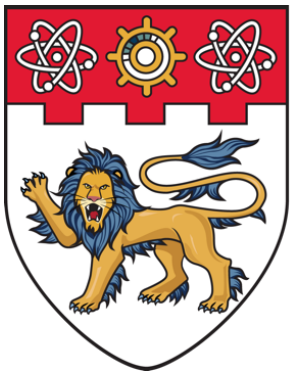

NANYANG TECHNOLOGICAL UNIVERSITY
SINGAPORE

DEVELOPMENT OF EARTH-ABUNDANT COPPER PHOTOSENSITIZERS FOR ARTIFICIAL PHOTOSYNTHESIS

NG YIK YIE

SCHOOL OF PHYSICAL AND MATHEMATICAL SCIENCES

2019

DEVELOPMENT OF EARTH-ABUNDANT COPPER PHOTOSENSITIZERS FOR ARTIFICIAL PHOTOSYNTHESIS

NG YIK YIE

SCHOOL OF PHYSICAL AND MATHEMATICAL SCIENCES

A thesis submitted to the Nanyang Technological University in partial fulfilment of the requirement for the degree of Doctor of Philosophy

2019

Statement of Originality

I hereby certify that the work embodied in this thesis is the result of original research done by me except where otherwise stated in this thesis. The thesis work has not been submitted for a degree or professional qualification to any other university or institution. I declare that this thesis is written by myself and is free of plagiarism and of sufficient grammatical clarity to be examined. I confirm that the investigations were conducted in accord with the ethics policies and integrity standards of Nanyang Technological University and that the research data are presented honestly and without prejudice.

7 Jan 2019

. . . . . .

Date

. . . . . .

Ng Yik Yie

Supervisor Declaration Statement

I have reviewed the content and presentation style of this thesis and declare it of sufficient grammatical clarity to be examined. To the best of my knowledge, the thesis is free of plagiarism and the research and writing are those of the candidate's except as acknowledged in the Author Attribution Statement. I confirm that the investigations were conducted in accord with the ethics policies and integrity standards of Nanyang Technological University and that the research data are presented honestly and without prejudice.

7 Jan 2019

. . . . . .

Date

. . . . . .

Dr. Soo Han Sen

Authorship Attribution Statement

This thesis contains material from two paper(s) published in the following peer-reviewed journal(s) where I was the first and/or second author.

Chapter 2 and 3 are published as Kee, J. W.; Ng, Y. Y.; Kulkarni, S. A.; Muduli, S. K.; Xu, K.; Ganguly, R.; Lu, Y.; Hirao, H.; Soo, H. S., Development of bis(arylimino)acenaphthene (BIAN) copper complexes as visible light harvesters for potential photovoltaic application. *Inorganic Chemistry Frontiers* **3**, 651-662 (2016). DOI: 10.1039/C5QI00221D.

The contributions of the co-authors are as follows:

- A/Prof Soo and Dr. Kee provided the initial project direction and edited the manuscript drafts.
- Dr. Kee and I prepared the manuscript drafts.
- I assisted Dr. Kee in the syntheses and characterizations of all the compounds.
- Dr. Kulkarni and Dr. Muduli were involved in the incorporation of the newly synthesized complexes into DSSCs and they collected the measurements obtained from the device testing.
- Dr. Xu, Dr. Lu, and A/Prof Hirao were instrumental in the computational studies performed.
- Dr. Ganguly collected all the crystallographic data and performed the analysis.

Chapter 4 is published as Ng, Y. Y.; Tan, L. J.; Ng, S. M.; Chai, Y. T.; Ganguly, R.; Du, Y.; Yeow, E. K. L.; Soo, H. S., Spectroscopic characterization and mechanistic studies on visible light photoredox carbon–carbon bond formation by bis(arylimino)acenaphthene copper photosensitizers**.** *ACS Catalysis* **8**, 11277–11286 (2018). DOI: 10.1021/acscatal.8b02502.

The contributions of the co-authors are as follows:

- A/Prof Soo H. S. provided the initial project direction and edited the manuscript drafts.
- I wrote the drafts of the manuscript.
- I performed the synthesis and characterization of the compounds, collected most of the spectroscopic data, and conducted data evaluation.
- Ms. Tan L. J. and Ms. Chai Y. T. assisted with the synthesis of a few of the compounds.
- Ms. Ng S. M. performed the time-correlated single photon counting (TCSPC) measurements.
- Dr. Ganguly collected all the crystallographic data and performed the analysis.
- Dr. Du Y. performed the X-ray absorption spectroscopy (XAS).
- Dr. Yeow E. K. L. provided insightful suggestions during manuscript preparations.

7 Jan 2019

. . . . . .
Date

. . . . . .
Ng Yik Yie

Acknowledgements

I would like to express my gratitude to my supervisor, Dr. Soo Han Sen for his continuous guidance during these four years. Thank you, Prof. Tan Howe Siang and Prof. Nripan Mathews, for being my Thesis Advisory Committee (TAC) members.

I would like to thank Jun Wei for being a great mentor during the beginning of my PhD days. Thank you to all my past and present colleagues in the research group, Haiyan, Jia Hui, Leonard, Zonghan, Jing Yi, Milosh, Sunny, Andrew, Xian Liang, Thiru, Subas, Gazi, and Siva for always being there to lend their help and support, making my every day in lab truly blessed.

The help I received from the undergraduate and exchange students, Lisa, Yoke Tin, Sze Shiek, Jin Shern, James, Ha Young, Jia Yang, Cher, Zhi Sian, and Meiraba is also appreciated.

I would like to thank the collaborators Prof. Hajime, Dr. Lu, and Xu Kai for the DFT calculations; Dr. Kulkarni and Dr. Muduli for the DSSC measurements, Dr. Ganguly for all the single crystal XRD data; Shue Mei and Prof. Edwin Yeow for the TCSPC measurements.

I am grateful to Nanyang Technological University (NTU) for the research scholarship. I would also like to thank all the SPMS and CBC staff including those from the Central Equipment Lab and Teaching Lab for providing their assistance with the various facilities and other administrative matters.

A big thank you to my family and friends whose love and encouragement helped me go a long way. The most heartfelt thank you to my father for his unconditional love. Although you are no longer here with me, but I know you would be the happiest for me. Miss you!

Table of Contents

Summary

A series of bis(arylimino)acenaphthene (Ar-BIAN) Cu^{I} complexes have been synthesized in three or fewer steps. A comprehensive study of their electrochemical and spectroscopic properties has been performed. The Ar-BIAN Cu^{I} complexes herein have been incorporated into dye-sensitized solar cells (DSSCs) or photoredox reaction to investigate their potential applications.

In Chapter 2, two new Ar-BIAN ligands and their corresponding homoleptic Cu^{I} complexes were synthesized and studied. The solution and solid-state absorption characteristics of the complexes have been examined. They were found to be panchromatic and absorb into the near-infrared (NIR) region. Notably, the crystal structure of one of the complexes gave an unprecedented rhombically distorted square planar geometry about the metal center. Computational studies revealed the non-covalent interactions between the aromatic functionalities and among the iodide atoms. To investigate the practical application of the complexes, they were anchored onto a metal oxide surface and incorporated into dye-sensitized solar cells (DSSCs). However, the efficiencies obtained and discussed in Chapter 3 were lower than expectations.

In Chapter 4, another group of panchromatic Ar-BIAN Cu^{I} complexes were synthesized and characterized. Electrochemical measurements showed that two of the complexes can be regenerated after redox activities. From the photoluminescence experiments, one of the complexes displayed a weakly emissive signal. According to the time-correlated single-photon counting (TCSPC) measurements, the photoluminescence has a bi-exponential lifetime (τ_1 = 3.6 ns; τ_2 = 11 ns). Following on, the luminescent complex was employed in the photocatalysis of atom transfer radical addition (ATRA) reactions. Spectroelectrochemical studies were carried out to obtain the UV-visible absorption spectra of the Cu^{II} species formed upon oxidation. A comparison of the absorption spectra of the independently synthesized Cu^{II} complex and the species formed during the photoredox reaction led us to conclude that the intermediate contained CBr_3 or Br^- attached to the Cu^{II} metal center.

List of Abbreviations

ACN	acetonitrile
AcOH	acetic acid
AIM	Atoms-in-Molecules
Ar	aryl (substituted aromatic ring)
Ar-BIAN	*bis*(*N*-arylimino)acenaphthene
ATRA	atom transfer radical addition
BCP	bond critical point
bpy	bipyridine
Btu	British thermal unit
CSD	Cambridge Structural Database
CV	cyclic voltammetry/cyclic voltammogram
DABCO	1,4-diazabicyclo[2.2.2]octane
dap	2,9-bis(para-anisyl)-1,10-phen
dbp	2,9-di-*n*butyl-1,10-phen
DCM	dichloromethane
DFT	density functional theory
dipp	2,6-diisopropylphenyl
diptmp	2,9-diisopropyl-3,4,7,8-tetramethyl-1,10-phenanthroline
DMF	*N*,*N*-dimethylformamide
dmp	2,9-dimethyl-1,10-phenanthroline
DMSO	dimethyl sulfoxide
DRS	diffuse reflectance spectroscopy
dsbtmp	2,9-di(sec-butyl)-3,4,7,8-tetramethyl-1,10-phenanthroline
DSPEC	dye-sensitized photoelectrosynthesis cell
DSSC	dye-sensitized solar cells
equiv	equivalent
Fc^+/Fc	ferrocenium/ferrocene redox couple
GC	gas chromatography
h	hour
HOMO	highest occupied molecular orbital
HRMS	high resolution mass spectrometry
Hz	hertz
IEA	International Energy Agency

ILCT	intraligand charge transfer
J–T	Jahn–Teller
LLCT	ligand to ligand charge transfer
LUMO	lowest unoccupied molecular orbital
M	concentration (mol L^{-1})
M^+	parent ion peak (mass spectrum)
Me	methyl
MeOH	methanol
mg	milligram
MHz	megahertz
MIC	mesoionic carbene
min	minute
mL	millimeter
MLCT	metal-to-ligand charge transfer
mmol	millimole
mol%	mole percent
NCI	non-covalent interactions
NHC	*n*-heterocyclic carbene
NIR	near infrared
NMR	nuclear magnetic resonance
OLED	organic light emitting diode
ORTEP	Oak Ridge Thermal Ellipsoid Plot
Ph	phenyl
Phen	phenanthroline
PV	photovoltaics
POP	bis[2-(diphenylphosphino)phenyl]ether
TCSPC	time-correlated single-photon counting
TEP	Tolman electronic parameters
THF	tetrahydrofuran
TLC	thin layer chromatography
TW	terawatts
UV-vis	ultraviolet-visible
VT	variable temperature

Index of Symbols

δ	chemical shift (ppm)
°C	degree centigrade
i_{pa}/i_p^{ox}	oxidative peak current (anodic)
i_{pc}/i_p^{red}	reductive peak current (cathodic)
ε	extinction coefficients
E_0	formal electrode potential
$E_{1/2}$	half-wave potential
E_{pa}	Oxidative peak potential (anodic)
E_{pc}	Reductive peak potential (cathodic)
π	pi
σ	sigma
J	coupling constants
d	doublet
m	multiplet
q	quartet
s	singlet
t	triplet

Chapter 1
Introduction

1.1 Motivation: Harnessing Solar Energy and Storage *via* Artificial Photosynthesis

Throughout history, the Earth's climate has undergone multiple cycles of changes because of the slight alterations to the Earth's orbit.[1] However, since the beginning of the modern era, the warming of the Earth can be attributed to the rapid human industrialization and exploding world population growth.[2] In the past century, there has been an accelerated rise in demand for energy by the burning of fossil fuels leading to a concomitant rise in the level of atmospheric carbon dioxide and other greenhouse gases. Since the 1950s, we have also witnessed more occurrence of erratic weather patterns and natural catastrophes such as the extended periods of droughts and extreme heatwaves.[3] It is inevitable that with the continuous increase in the world population, the demand for energy will continue with its upward trend. The amount of energy required by the world is projected to increase by almost 30% from 575 quadrillion British thermal unit (Btu) in 2015 to 736 quadrillion Btu in 2040.[4] Since there is little means to slow down our global energy consumption, it is crucial to direct our attention to more efficient use of sustainable sources of energy. According to the International Energy Agency (IEA), the use of renewables has seen the biggest hike in comparison to the other fuels. However, we still rely heavily on the burning of fossil fuels as it accounts for about 81% of our total energy usage in 2017.[5]

At present, there are various sustainable energy resources available and they are gaining popularity as illustrated in Figure 1. For instance, the use of solar photovoltaics (PV) and wind energy are predicted to almost double by 2040.[5] Being one of the most abundant and sustainable energy sources, solar energy has emerged as one of the most promising approaches. In one hour, the Sun delivers approximately 120,000 TW to the surface of Earth, comparable to 6000 times of the world's energy demand in a year.[6] Natural photosynthesis is the ideal example of the extensive use of solar energy and its storage. The building blocks for all living organisms are made by converting naturally abundant water and carbon dioxide into functional organic molecules. It is therefore an opportunity to harness solar energy without the harmful effects from the burning of fossil fuels by mimicking Nature *via* artificial photosynthesis.[7]

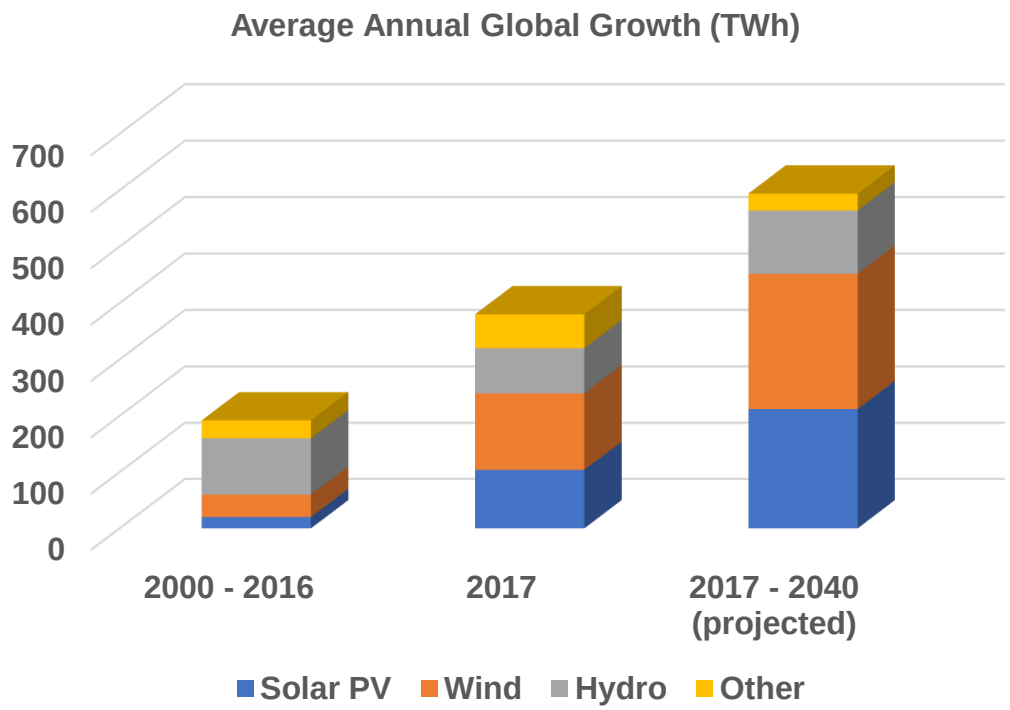

Figure 1.1 The average annual global growth in renewable energy generated by solar PV, wind, hydropower and other technologies from the past until 2040 assuming Sustainable Development Scenario.[5]

1.2 Artificial Photosynthesis

Artificial photosynthesis is the process involving the storage of energy by generating renewable fuels and chemicals from H_2O and CO_2 using light.[8] The simplified schematic representation of the 'Z-scheme' in artificial photosynthesis is given in Figure 1.2. The 'Z-scheme' shows the reduction and oxidation processes occurring in a photosynthetic system with two light absorbers. In natural photosynthesis, light absorption and charge separation of the two photosensitizers occur across a phospholipid membrane containing mediating small molecules to transfer the electrons. As illustrated in Figure 1.2, 'Z-scheme' allows the reductive and oxidative active sites to be spatially separated thus enhancing the separation efficiency of photogenerated charge carriers with potent redox ability.[9]

In the 'Z-scheme' (Figure 1.2) of the artificial photosynthetic system, the photosensitizers absorb (visible) light to create an electron-hole pair. The oxidative holes will be used by a water oxidation catalyst (WOC) to oxidize H_2O to O_2 while the electrons and protons generated are captured by a hydrogen evolving catalyst (HEC) to

reduce protons to H_2. Alternatively, a CO_2 reduction catalyst (CRC) can be used in place of HEC to reduce CO_2 to CO, CH_4 and CH_3OH. These chemicals that are formed have a larger energetic content than their corresponding substrates and can be used as fuels as they can be easily stored, transported and burned to produce energy.[10] Central to the artificial photosynthetic system is the panchromatic chromophore that can efficiently harvest sunlight to generate electrochemical potential.[11]

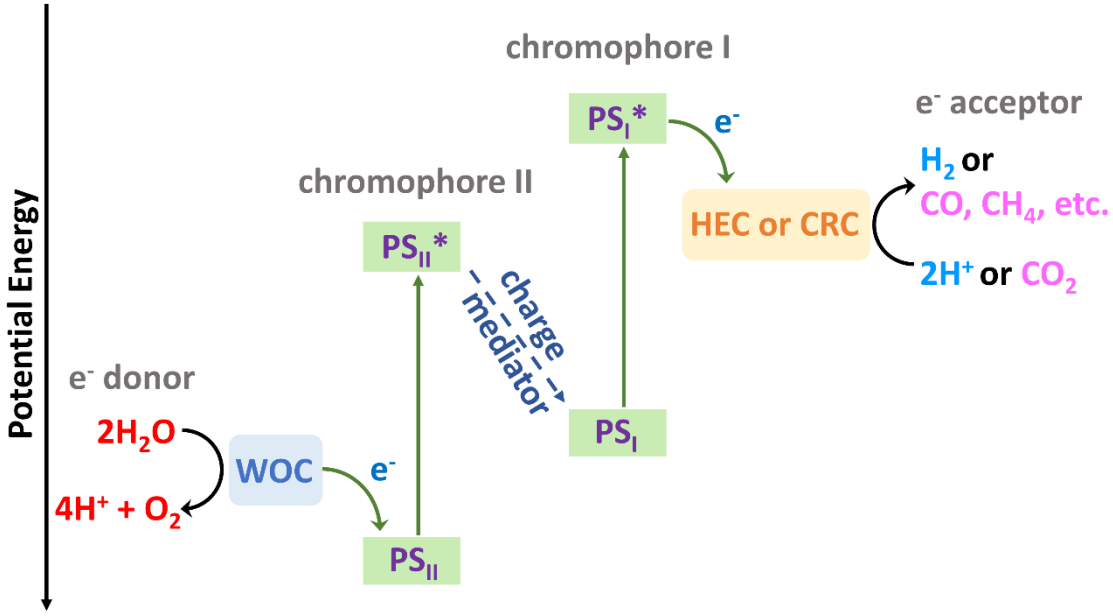

Figure 1.2 A simplified schematic representation of the 'Z-scheme' for artificial photosynthesis with chromophore I and II (PS_I and PS_{II} respectively) as the light-harvesting units, water oxidation catalyst (WOC), hydrogen evolving catalyst (HEC), or CO_2 reduction catalyst (CRC).[10]

1.3 Dye Sensitizers

1.3.1 Ru^{II} Photosensitizers

Some characteristics of an ideal light-harvester include a panchromatic to NIR absorption, an adequately long photoexcited lifetime to allow injection or transfer of charges to occur before ineffective recombination processes, suitable anodic and cathodic potentials, and stability.[12] To date, the most popular photosensitizers are of Ru^{II}-based due to their stability and efficiency. A typical example of a Ru^{II}-based photosensitizer is $[Ru(bpy)_3]^{2+}$ (bpy = tris(bipyridine)), which has a d^6 low spin

electronic configuration. Upon light irradiation, an electron from the metal is promoted from the singlet ground state to the singlet excited state which is the unoccupied π* orbital of the ligand *via* a metal-to-ligand charge transfer (MLCT), schematically represented in Figure 1.3 by the green arrow.[13] The excited electron will undergo intersystem crossing (ISC) to the triplet excited state aided by the heavy-atom effect of the Ru metal. In the triplet excited state, the photoexcited complex ($[Ru(bpy)_3]^{2+*}$) has a long lifetime since it is spin-forbidden to decay back to its singlet ground state.[11, 13-14]

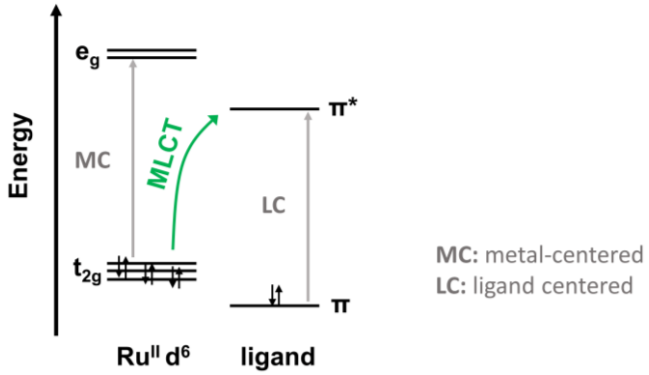

Figure 1.3 Possible electronic transitions in a Ru^{II} complex.[15]

Some examples of commercially available Ru complexes are also shown in Figure 1.4. One of the most notable Ru polypyridyl based dye is **N-3** (Figure 1.4), which has a broad absorption spectrum in the visible light region and a photoexcited lifetime of about 20 ns. In addition, the presence of four carboxylate functional groups allow it to be strongly anchored onto the surface of the TiO_2 semiconductor. In combination with all these desirable attributes, Nazeeruddin *et al*. obtained a groundbreaking solar-to-electric efficiency of 10%[16] as compared to prior reports of dye-sensitized photoelectrochemical cells where the efficiency was less than 1%. Since the success of **N-3**, many research groups have modified or redesigned the ligands of Ru dyes to further improve their chemical stability, electrochemical potentials, photoexcited lifetimes, and absorption and emission properties.[17]

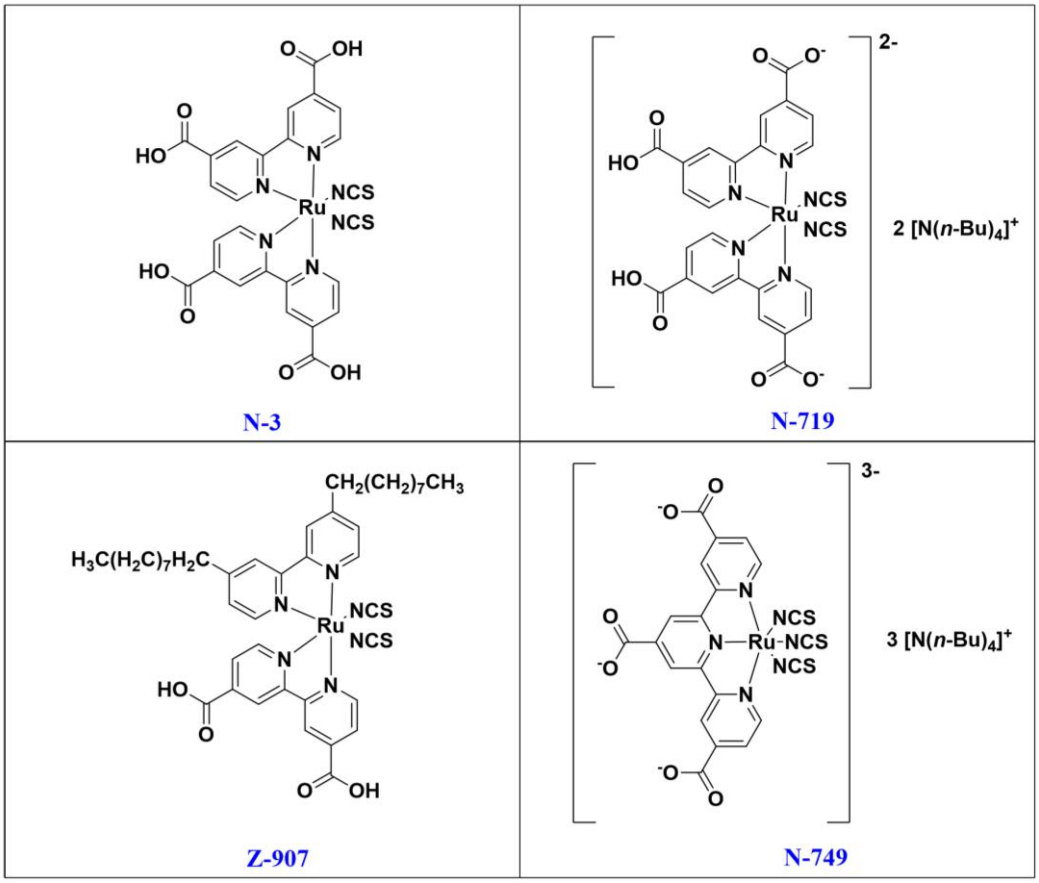

Figure 1.4 Some examples of commercially available Ru^{II} based dye molecules.[18]

With careful adjustments to the ligand design such as increasing the number of conjugation groups to the ancillary ligands[19] and modifying the electron donating or withdrawing substituents, the panchromaticity of the Ru^{II} complexes can be improved.[17a] Due to its many desirable photochemical and photophysical properties, Ru^{II}-based complexes have always been a popular choice as a dye molecule.

Although commonly employed, there are disadvantages to using Ru^{II}-based complexes. Notably, ruthenium is a precious metal leading to its high cost. Also, Ru compounds have high toxicity. In this respect, we are interested in looking into more sustainable alternatives, namely the earth abundant first-row transition metals to reduce the cost of production. The transition metal of choice is copper due to its similarities in photophysical properties[20] which will be discussed in the subsequent section.

1.3.2 Cu^{I} Photosensitizers

Similar to Ru^{II} complexes, an electron of the Cu^{I} complex is promoted from the d orbital of the metal center to an empty antibonding π* orbital of its ligand upon photoexcitation as depicted by the green arrow in Figure 1.5, and since Cu^{I} has fully occupied d orbitals, the number of non-radiative deactivation are reduced as there will not be any d-d transitions. Under suitable conditions, it is also possible for its singlet excited state to undergo rapid ISC to the triplet excited state thereby increasing the excited state lifetime.

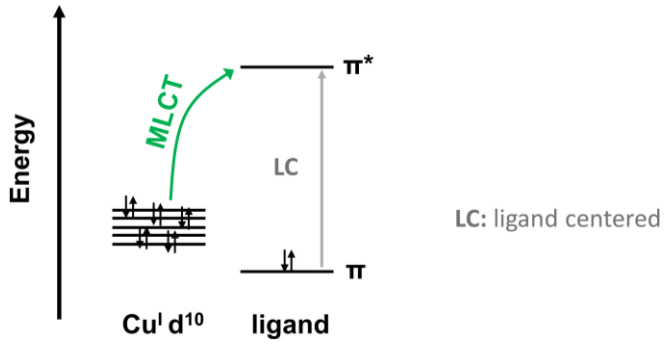

Figure 1.5 Possible electronic transitions in a Cu^{I} complex.[21]

However, after light irradiation, the d^{10} Cu^{I} complex will have a d^{9} electronic configuration since the Cu^{I} metal center now has a formal oxidation state of Cu^{II}. Pseudo-Jahn-Teller distortion arises from this uneven distribution of electrons in the d orbitals. In the ground state, a Cu^{I} complex typically has a distorted tetrahedral geometry whereas the photoexcited complex will likely adopt a more flattened geometry allowing the coordination of solvent molecules as shown in Figure 1.6. As a result, the excited state lifetime will be dramatically shortened due to the fast non-radiative decay of the MLCT excited state after the formation of the exciplex.[22] The formation of the five-coordinate exciplex was proposed by McMillin and co-workers after they increased the nucleophilicity of counterions on their $Cu^{I}(phen)_2$ complex and performed a series of photochemical experiments on them.[23] This hypothesis was confirmed by Chen *et al.* when they structurally determined the MLCT excited state via transient X-ray absorption spectroscopy and femtosecond optical spectroscopy.[24]

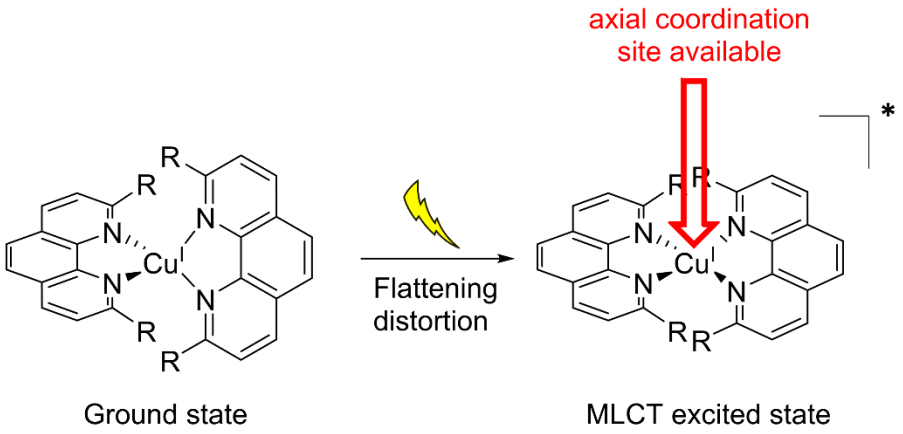

Figure 1.6 After the ground state $Cu^{I}(phen)_2$ complex is excited by light, the distorted tetrahedral geometry is "flattened" resulting in an empty axial coordination site in the MLCT excited state susceptible to attack by solvent molecules or counterions.[21]

To circumvent this problem, many research groups have modified the design of the ligands to improve the excited lifetimes of the Cu^{I} photosensitizers by increasing the steric bulk to prevent any additional molecules from coordinating to the metal center after light excitation. The most commonly investigated Cu^{I} photosensitizers includes cuprous phenanthroline (phen) and bipyridine (bpy) derivatives. Pioneering work on such Cu^{I} complexes by McMillin and co-workers reported photoluminescence of $Cu(dmp)_2^{+}$ (dmp = 2,9-dimethyl-1,10-phenanthroline) with an excited lifetime of 54 ± 10 ns.[25] By further increasing the steric bulk, Castellano and co-workers increased the lifetimes of their $Cu^{I}(phen)_2$ complexes to the microsecond timescales by introducing *sec*-butyl and isopropyl substituents to the 2,9-positions of 1,10-phen.[26] The long-lived excited lifetimes of $[Cu^{I}(diptmp)_2]^{+}$ (diptmp = 2,9-diisopropyl-3,4,7,8-tetramethyl-1,10-phen) and $[Cu^{I}(dsbtmp)_2]^{+}$ (dsbtmp = 2,9-di(sec-butyl)-3,4,7,8-tetramethyl-1,10-phen) recorded in deaerated dichloromethane (DCM) are given in Figure 1.7.[26]

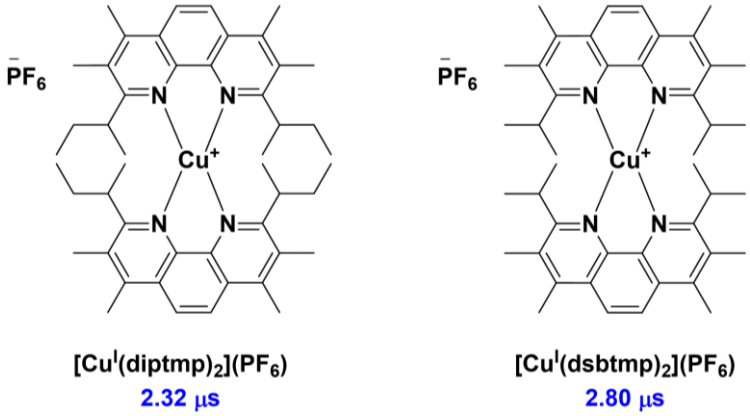

Figure 1.7 Molecular structures and excited lifetimes of two of the longest-lived homoleptic Cu^{I} photosensitizers to date.[26]

Other than the homoleptic Cu^{I} complexes mentioned above, heteroleptic ones have also been investigated. Some notable examples include those with bidentate phosphines as they exhibit impressive emission properties and excellent quantum efficiencies suitable for use in organic light emitting diodes (OLEDs).[27] For instance, Cuttell *et al*. reported new luminophores and $[Cu(dbp)(POP)]^{+}$ (dbp = 2,9-di-*n*butyl-1,10-phen; POP = bis[2-(diphenylphosphino)phenyl]ether) showed a remarkable excited state lifetime of 16.1 μs and emission efficiencies reaching 20%.[28]

With these attractive photophysical properties, Cu^{I}-based complexes are also gaining popularity as photocatalysts in various visible-light assisted photoredox reactions. For example, Reiser and team used $[Cu(dap)_2Cl]$ (dap = 2,9-bis(para-anisyl)-1,10-phen) to photocatalyze C-C bond formation *via* atom transfer radical addition (ATRA) reactions using visible light.[29] In 2014, Kainz *et al.* demonstrated the in-situ synthesis of a photoactive Cu^{I} complex to promote the formation of a new C-N bond thus generating highly enantioselective tertiary alkyl amines.[30] Evidently, Cu^{I} complexes have the potential to function as useful photoredox catalyst which are otherwise dominated by the use of expensive and rare transition metals.

1.4 *Bis*(arylimino)acenaphthene (Ar-BIAN) Ligands

1.4.1 Synthesis of Ar-BIAN Ligands

Although the abovementioned Cu^{I} complexes show excellent properties suitable for various applications, their synthesis require tedious synthetic routes and the use of rare and expensive precursors. One advantage of using Ar-BIAN is its ease of synthesis since it only requires a one-step condensation between commercially available anilines and acenaphthenequinone assisted by a Lewis acid.

For example, van Asselt *et al*. reported the formation of dipp-BIAN (dipp = 2,6-diisopropylphenyl) by simply refluxing a mixture of acenaphthenequinone and 2,6-diisopropylaniline in acetic acid (AcOH) for 1 h.[31] Whereas for synthesis of 2-$CF_3C_6H_4$-BIAN, a harsher condition was needed with the use of sulfuric acid under Dean-Stark conditions with toluene as the solvent.[32] In many other cases, the synthesis requires the formation of a metal complex of the intended Ar-BIAN ligand in-situ and the subsequent removal of the metal as presented in Scheme 1.1. For example, mesityl-, *p*-Cl-, *p*-Me-, and *p*-OMe-Ar-BIAN are synthesized by refluxing the acenaphthenequinone with approximately two equivalents of the corresponding anilines in AcOH with the addition of either excess $ZnCl_2$ or $NiBr_2$.[31] The purpose of the metal halide is for the formation of a less soluble product than its starting material so that the desired compound can be formed by precipitating out from the solution.

Scheme 1.1 Synthesis of Ar-BIAN *via* the use of a "metal template".[31]

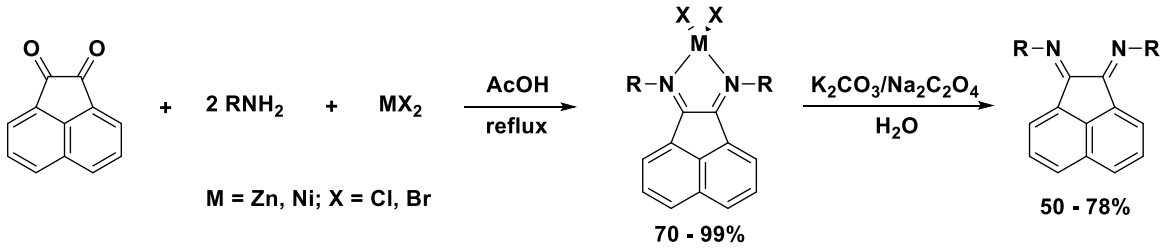

1.4.2 Properties of Ar-BIAN Ligands

Since the report by van Asselt *et al.*, Ar-BIAN compounds have become popular choices for catalytic and polymerization reactions.[33] Ar-BIANs are bidentate nitrogen ligands that are highly conjugated thus there is enhanced π-delocalization resulting in low-lying π^* orbitals, functioning as the LUMO for the Cu^I complex thereby reducing the HOMO-LUMO gap. This will allow the corresponding Cu^I complex to absorb in the red and even near-infrared region of the solar spectrum which is a desirable property for a light-absorbing material in solar energy harvesting technologies.

Additionally, Ar-BIAN derivatives are known to be redox-active, capable of accepting up to four electrons due to its delocalized π-electron system. According to Fedushkin and co-workers, Ar-BIAN can store up to four electrons reversibly upon consecutive two-electron reductions (Scheme 1.1).[34] This hypothesis was confirmed when their team isolated and structurally characterized the alkali metal derivatives of the one to four electrons reduced BIAN ligand.[34] Therefore, this redox non-innocent ligand behaves like a "capacitor" by providing a potential electron reservoir for catalytic multi-electron reactions. This is further proved by Gomes and group when they reported a series of Ar-BIAN Cu^I complexes that can perform reversible oxidation and reduction processes.[35] They successfully applied their complexes to the cycloaddition catalysis between azides and alkynes with a high catalytic activity matching that of the archetypal $CuSO_4$-sodium ascorbate catalyst system.[35]

Scheme 1.2 Illustration showing four electrons reversible reduction of the Ar-BIAN ligand.[34]

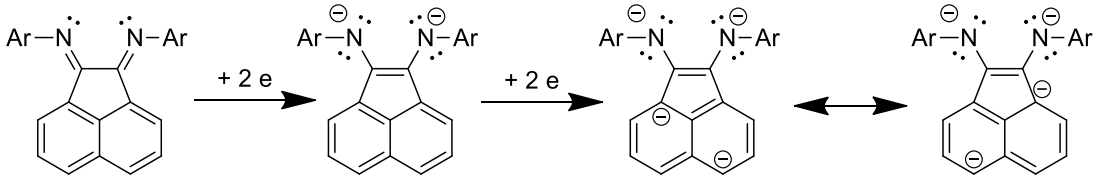

The structural rigidity of the Ar-BIAN ligand due to the strain of the diazabutadiene (DAB) moiety limits the range of bonding modes thus favoring robust chelation to metal centers. Typically, both the carbon to nitrogen bonds at the DAB moiety adopt a *E* conformation[36] whereby the higher priority functional groups (represented by the blue circle and Ar group) are on the opposite sides of the C-N double bond as shown in Figure

1.8(a). The opposite is true for the *Z* conformation where the higher priority groups are on the same side of the C-N double bond.

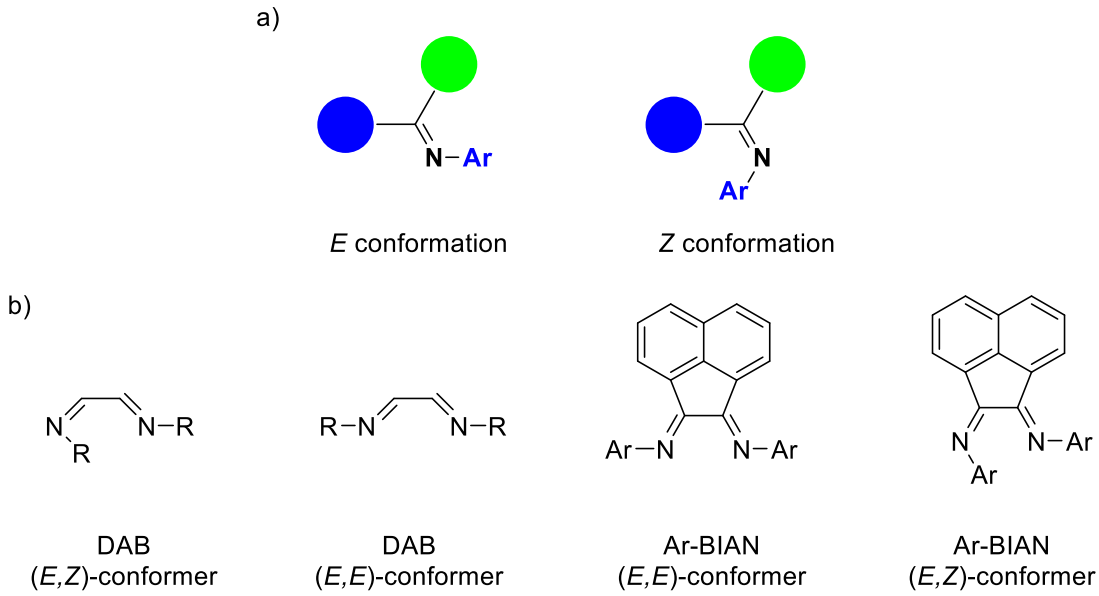

Figure 1.8 (a) The C-N double bond found in Ar-BIAN. The blue circles represent the higher priority group attached to the carbon while the green circles represent the lower priority group. (b) The different structural conformations of DAB and Ar-BIAN.

Figure 1.8 shows the different structural conformations of the DAB moiety and Ar-BIAN. In addition to the more common (*E*,*E*) conformers, there are also reports on a mixed (*E*,*Z*) conformation.[37] The presence of both the conformations have been confirmed by nuclear magnetic resonance (NMR) experiments which show that when the Ar-BIAN is dissolved in a solution, it undergoes rapid interconversion between the (*E*,*E*) and (*E*,*Z*) conformers (Scheme 1.3). Although this dynamic process does not hinder the binding of the strongly chelating ligand to form a robust metal complex as it transforms to the (*E*,*E*) conformer after complexation with the metal center.[37]

Scheme 1.3 Schematic representation of the rapid interconversion between the two conformers.[38]

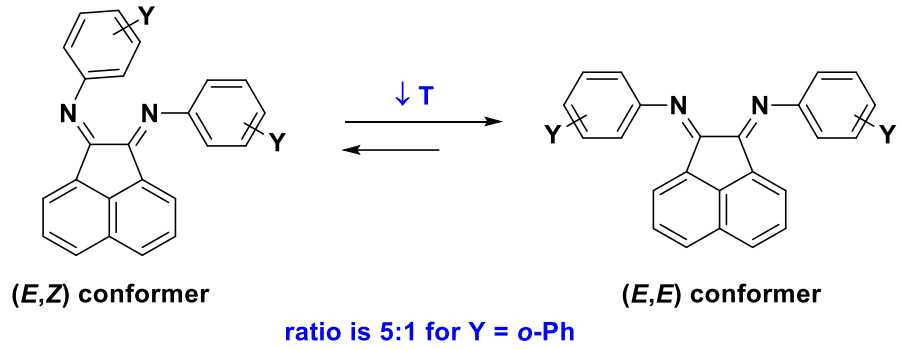

Another factor influencing the chelation to the metal center is the substituent group on the imine as it affects the stereoelectronic tunability.[37b] This is evident from a series of experiments performed by the Ragaini group to obtain the relative coordination strength of different chelating nitrogen ligands toward Pd^{0} and Pd^{II}. Therefore, a judicious choice of anilines used for the Ar-BIAN synthesis is necessary. In general, the more electron-donating substituents on the imine allows the ligand to bind more strongly to the metal center and is more favorable with metals with higher oxidation states. However, dipp-BIAN is an exception as it was found to chelate more weakly than its basicity suggests due to steric reasons.[39]

1.4.3 Ar-BIAN Cu^{I} Complexes

Ar-BIANs are known to be non-innocent ligands as they tend to stabilize radical species after their reactions with first-row transition metals. To find out the oxidation state of both the metal and Ar-BIAN ligand, Tkachenko and co-workers carried out NMR spectroscopy and crystallographic analysis to verify the presence of a Cu^{I} center and that the coordinated Ar-BIAN ligands were structurally similar to the neutral ones within acceptable experimental error.[38] The sharp peaks in the NMR spectra obtained suggest the absence of paramagnetic behavior. The structure shown in Figure 1.9 shows the Ar-BIAN ligands and the corresponding Cu^{I} complexes that they synthesized.[38]

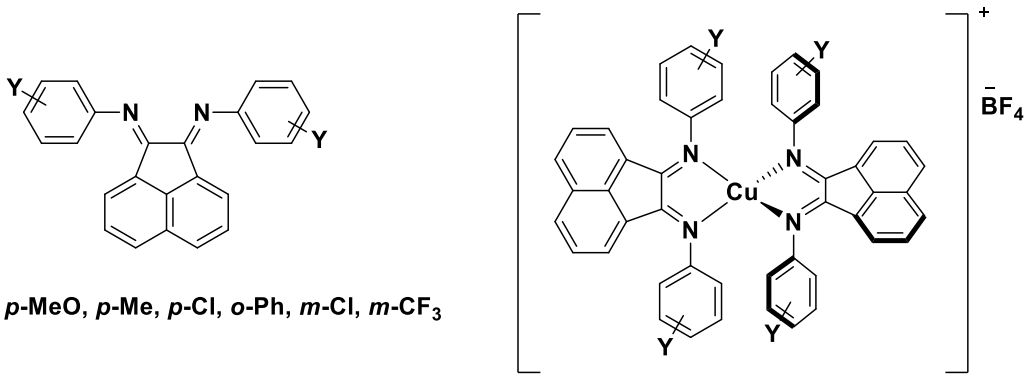

Figure 1.9 Molecular structures of the Ar-BIAN ligands and the corresponding Cu^{I} complexes Papanikolaou *et al.* synthesized and studied.[38]

These complexes showed improved light-harvesting features as their metal-to-ligand charge transfer (MLCT) absorptions were shifted towards longer wavelengths due to the stabilization of the π* orbitals through better electronic delocalization. The MLCT absorption of the complexes has λ_{max} in the visible region between 580 and 610 nm.[38] They postulated that when MLCT transitions are low-lying, they result in amply long photoexcited lifetimes and potential emission from the complexes.[38]

Subsequently, Zysman-Colman and group observed weak emission signals, which were previously unobserved in Ar-BIAN Ir complexes, after installing ester and carboxylate functionalities in their heteroleptic Ir complexes at the bay region of the acenaphthene (Figure 1.10). The electron-withdrawing substituents were initially installed to improve the π-accepting ability and better anchoring of the complexes for incorporation into DSSCs.[40] From the density functional theory (DFT) calculations, they assigned the emission bands to the spin-allowed fluorescence from the mixture of singlet intraligand charge transfer (^{1}ILCT), ^{1}MLCT, and singlet ligand-to-ligand charge transfer (^{1}LLCT) states.[40] Previously, Tkachenko and co-workers reported that the MLCT excited state for complexes with Ar-BIAN ligands deactivates to the non-emissive lower lying triplet intraligand state before decaying to the ground state. This is likely because the orbitals involved in the lowest MLCT excited state are primarily localized in the diiminic region leading to the ultrafast recombination.[41] With the presence of the electron-withdrawing groups to further localize the π-accepting orbital on the bay region of the acenaphthene, Zysman-Colman and group noticed a better spatial separation of the electron from the metal center. Thus, the observation of slightly longer-lived, radiative singlet photoexcited states.[40]

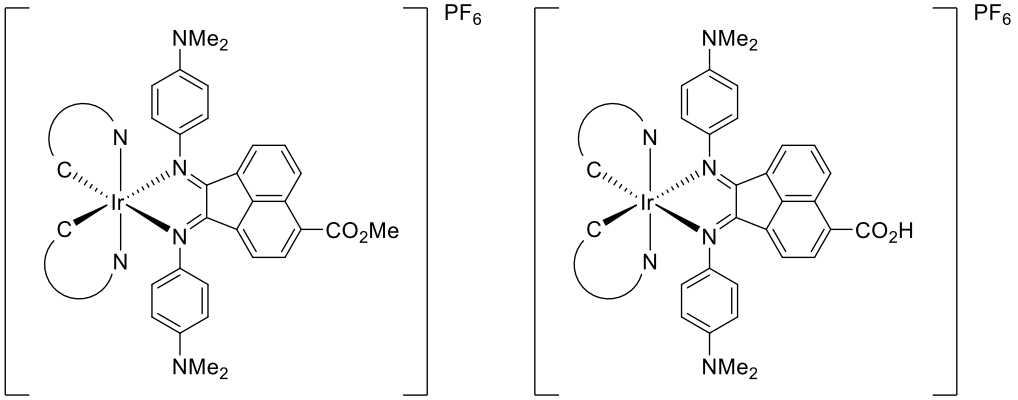

Figure 1.10 Ir complexes that displayed weak emission signals.[40]

Inspired by these studies, we sought to develop synthetically versatile Ar-BIAN complexes of Cu^{I} that are highly absorptive. We aim to improve the photophysical properties of such complexes by introducing heavier halogens on the ligand periphery to induce strong spin-orbit coupling. This can potentially enhance the rate of ISC to prolong the photoexcited lifetime of the MLCT state for observable luminescence signals. Also, by a judicious selection of substitution group at the ortho-position of the aniline, suitably bulky Ar-BIAN ligands can be synthesized to stabilize the corresponding Cu^{I} complex against the flattening distortion after photoexcitation to further improve its excited state lifetime. We hypothesize that with these modifications on the ligand, the resulting Ar-BIAN Cu^{I} complexes will be able to exhibit photoluminescence and improvements in the excited state lifetime to function as an attractive and more affordable candidate for light absorption in artificial photosynthesis applications as compared to the more expensive Ru and Ir.

1.5 Mesoionic Carbene (MIC) Ligands

Since the 1990s after Arduengo and co-workers isolated their first *n*-heterocyclic carbene (NHC),[42] such ligand system has remained as one of the most popular choices of chemists due to its strong σ-electron-donating property and highly versatile steric features. In this context, development of increasingly electron-donating ligands is of great interest in the field of organometallics chemistry and homogeneous catalysis. A new derivative of carbene was first reported by Crabtree *et al.* in 2002 when they characterized a new Ir compound bound to a carbene in its C4 position as opposed to the typical classical NHC binding at the C2 position as illustrated in Figure 1.11.[43] Subsequently, Bertrand and team termed such family of *abnormal* carbenes as

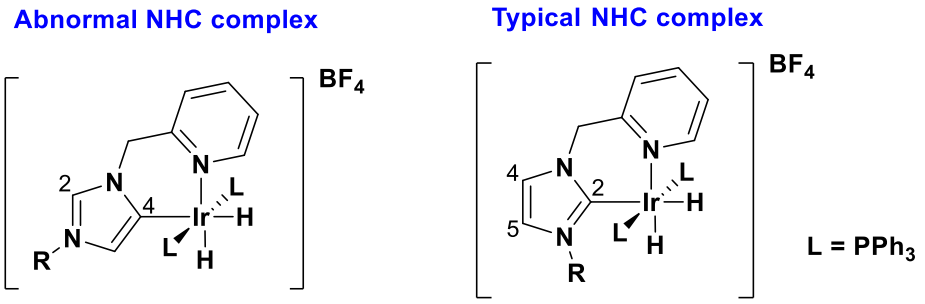

Figure 1.11 Comparison of the abnormal and typical NHC complex molecular structures.[43]

mesoionic carbenes (MICs) after they obtained new crystals of 1*H*-1,2,3-triazol-5-ylidenes.[44] The single crystal XRD structures that they obtained are for the compounds shown in Figure 1.12. Reasonable canonical resonance forms containing a carbene can only be drawn by including additional charges for the triazolylidenes hence it is appropriate to term it as mesoionic.

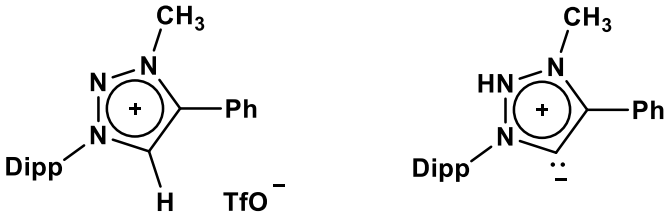

Figure 1.12 Molecular structures of the triazolium salt (left) and 1,2,3-triazol-5-ylidene (right) isolated by Bertrand and team.[44]

As compared to phosphorus-based ligands, carbenes are known to coordinate more strongly to their metal centers. Because of the strong carbon-to-metal bond, the complexes formed are more bench-top stable.[44] MIC ligands are strongly electron-donating, even more so than NHCs as observed from their smaller Tolman electronic parameters (TEPs) as compared to those of the classical NHCs.[45] It has been established that the combination of the strong σ-donating and π-accepting properties of carbenes helps to destabilize the deactivating triplet metal-centered (^{3}MC) state while retaining the ^{3}MLCT to obtain the long-lived excited species.[46] Therefore, the use of MIC ligands which are even more strongly electron-donating is advantageous in further separating the gap between the ^{3}MC and ^{3}MLCT states to obtain metal complexes with exceedingly long lifetimes.[17c] For example, Brown *et al.* synthesized a series of heteroleptic Ru^{II} complexes bearing MIC ligands to achieve microsecond excited-state lifetimes.[17c]

Another attractive property of MICs is their versatility. The synthesis involves a facile approach in using "click" chemistry for the [3+2] cycloaddition of acetylenes with azides to obtain 1,2,3-triazole compounds that can be easily transformed into MICs. This method allows for a large flexibility in adding a myriad of substituents and functionalities at the C1 and C4 positions of the triazole compound since there is endless variations of alkynes and azides to select from. This favors the tailoring of the electronic properties and steric bulkiness needed for the MIC metal complexes.[47]

1.6 Conclusion

In this introductory chapter, artificial photosynthesis has been proposed as a sustainable method to harness the sun's energy to produce chemicals with high energetic content to satisfy the world's demand for energy. Fundamentally challenging is the search for an ideal chromophore which is the *workhorse* of an artificial photosynthetic system. A brief review and some common examples of Ru^{II}-based photosensitizers have been discussed. The development of more sustainable alternatives such as Cu^{I}-based complexes is necessary to replace the expensive and toxic Ru. A comparison of the photophysical properties of Ru^{II} and Cu^{I} complexes have been presented. Beyond the typical but synthetically challenging phen and bpy ligands, synthetically more accessible Ar-BIAN ligands are introduced. Previously, much attention has been focused on their syntheses and exploration of their photophysical properties. Yet little has been done to further improve the ligand design and study the potential applications of the corresponding Cu^{I} complexes. Therefore, in the following chapters, the development of a series of new Ar-BIAN Cu^{I} complexes, their synthesis, detailed characterizations, and our attempt to incorporate them into DSSCs will be presented. In Chapter 4, further improvements made to the Ar-BIAN ligand will be examined and the corresponding Cu^{I} complex was applied to a photoredox reaction. The future direction of this project is also briefly mentioned in Chapter 5.

1.7 References

(1) Climate change: How do we know? https://climate.nasa.gov/evidence/ (accessed Jul, 8).

(2) World Population Prospects: The 2017 Revision. https://www.un.org/development/desa/publications/world-population-prospects-the-2017-revision.html (accessed Jul, 10).

(3) *Nature Climate Change* **2018**, *8*, 347.

(4) *International Energy Outlook 2017*; U.S. Energy Information Administration.

(5) *Global Energy and CO_2 Status Report 2017*; International Energy Agency.

(6) (a) Gratzel, M., *Acc. Chem. Res.* **2009**, *42*, 1788-1798; (b) Solar Energy Basics. https://www.nrel.gov/workingwithus/re-solar.html (accessed Jul, 9).

(7) (a) Dokic, M.; Soo, H. S., *Chem. Commun.* **2018**, *54*, 6554-6572; (b) Faunce, T. A.; Lubitz, W.; Rutherford, A. W.; MacFarlane, D.; Moore, G. F.; Yang, P.; Nocera, D. G.; Moore, T. A.; Gregory, D. H.; Fukuzumi, S.; Yoon, K. B.; Armstrong, F. A.; Wasielewski, M. R.; Styring, S., *Energy Environ. Sci.* **2013**, *6*, 695-698.

(8) (a) Kim, D.; Sakimoto, K. K.; Hong, D.; Yang, P., *Angew. Chem. Int. Ed.* **2015**, *54*, 3259-3266; (b) Barber, J., *Chem. Soc. Rev.* **2009**, *38*, 185-196; (c) Bonke, S. A.; Wiechen, M.; MacFarlane, D. R.; Spiccia, L., *Energy Environ. Sci.* **2015**, *8*, 2791-2796.

(9) Xu, Q.; Zhang, L.; Yu, J.; Wageh, S.; Al-Ghamdi, A. A.; Jaroniec, M., *Mater. Today* **2018**.

(10) (a) Berardi, S.; Drouet, S.; Francas, L.; Gimbert-Surinach, C.; Guttentag, M.; Richmond, C.; Stoll, T.; Llobet, A., *Chem. Soc. Rev.* **2014**, *43*, 7501-7519; (b) Tachibana, Y.; Vayssieres, L.; Durrant, J. R., *Nat. Photonics* **2012**, *6*, 511-518.

(11) Schultz, D. M.; Yoon, T. P., *Science* **2014**, *343*, 985.

(12) (a) Robertson, N., *Angew. Chem. Int. Ed.* **2008**, *47*, 1012-1014; (b) Armaroli, N., *Chem. Soc. Rev.* **2001**, *30*, 113-124.

(13) Giarikos, D. G., Artificial Photosynthesis: Ruthenium Complexes. In *Natural and Artificial Photosynthesis: Solar Power as an Energy Source*, Razeghifard, R., Ed. John Wiley & Sons, Inc.: 2013.

(14) Prier, C. K.; Rankic, D. A.; MacMillan, D. W., *Chem. Rev.* **2013**, *113*, 5322-5363.

(15) Campagna, S.; Puntoriero, F.; Nastasi, F.; Bergamini, G.; Balzan, V., *Photochemistry and Photophysics of Coordination Compounds: Ruthenium*. Springer: Berlin, Heidelberg, 2007; Vol. 280.

(16) (a) Nazeeruddin, M. K.; Kay, A.; Rodicio, I.; Humphry-Baker, R.; Mueller, E.; Liska, P.; Vlachopoulos, N.; Graetzel, M., *J. Am. Chem. Soc.* **1993**, *115*, 6382-6390; (b) O'Regan, B.; Grätzel, M., *Nature* **1991**, *353*, 737-740.

(17) (a) Yin, J.-F.; Velayudham, M.; Bhattacharya, D.; Lin, H.-C.; Lu, K.-L., *Coord. Chem. Rev.* **2012**, *256*, 3008-3035; (b) Pal, A. K.; Hanan, G. S., *Chem. Soc. Rev.* **2014**, *43*, 6184-6197; (c) Brown, D. G.; Sanguantrakun, N.; Schulze, B.; Schubert, U. S.; Berlinguette, C. P., *J. Am. Chem. Soc.* **2012**, *134*, 12354-12357; (d) Bomben, P. G.; Robson, K. C. D.; Koivisto, B. D.; Berlinguette, C. P., *Coord. Chem. Rev.* **2012**, *256*, 1438-1450.

(18) Desilvestro, H.; Hebting, Y. Ruthenium-based dyes for Dye-sensitized Solar Cells. https://www.sigmaaldrich.com/technical-documents/articles/materials-science/organic-electronics/dye-solar-cells.html (accessed Jul, 15).

(19) (a) Chen, C. Y.; Wu, S. J.; Wu, C. G.; Chen, J. G.; Ho, K. C., *Angew. Chem. Int. Ed.* **2006**, *45*, 5822-5825; (b) Akula, S. B.; Chen, H. S.; Su, C.; Chen, B. R.; Chiou, J. J.; Shieh, C. H.; Lin, Y. F.; Li, W. R., *Inorg. Chem.* **2017**, *56*, 12987-12995.

(20) (a) Robertson, N., *ChemSusChem* **2008**, *1*, 977-979; (b) Lu, X. Q.; Wei, S. X.; Wu, C. M. L.; Li, S. R.; Guo, W. Y., *J. Phys. Chem. C* **2011**, *115*, 3753-3761.

(21) Armaroli, N.; Accorsi, G.; Cardinali, F.; Listorti, A., Photochemistry and Photophysics of Coordination Compounds: Copper. In *Photochemistry and Photophysics of Coordination Compounds I*, Balzani, V.; Campagna, S., Eds. Springer Berlin Heidelberg: 2007; Vol. 280, pp 69-115.

(22) Housecroft, C. E.; Constable, E. C., *Chem. Soc. Rev.* **2015**, *44*, 8386-8398.

(23) Everly, R. M.; McMillin, D. R., *Photochem. Photobiol.* **1989**, *50*, 711-716.

(24) Chen, L. X.; Shaw, G. B.; Novozhilova, I.; Liu, T.; Jennings, G.; Attenkofer, K.; Meyer, G. J.; Coppens, P., *J. Am. Chem. Soc.* **2003**, *125*, 7022-7034.

(25) Blaskie, M. W.; McMillin, D. R., *Inorg. Chem.* **1980**, *19*, 3519-3522.

(26) (a) McCusker, C. E.; Castellano, F. N., *Inorg. Chem.* **2013**, *52*, 8114-8120; (b) Garakyaraghi, S.; Crapps, P. D.; McCusker, C. E.; Castellano, F. N., *Inorg. Chem.* **2016**, *55*, 10628-10636.

(27) Bizzarri, C.; Spuling, E.; Knoll, D. M.; Volz, D.; Bräse, S., *Coord. Chem. Rev.* **2017**.

(28) Cuttell, D. G.; Kuang, S.-M.; Fanwick, P. E.; McMillin, D. R.; Walton, R. A., *J. Am. Chem. Soc.* **2002**, *124*, 6-7.

(29) (a) Pirtsch, M.; Paria, S.; Matsuno, T.; Isobe, H.; Reiser, O., *Chem. Eur. J.* **2012**, *18*, 7336-7340; (b) Reiser, O., *Acc. Chem. Res.* **2016**, *49*, 1990-1996.

(30) Kainz, Q. M.; Matier, C. D.; Bartoszewicz, A.; Zultanski, S. L.; Peters, J. C.; Fu, G. C., *Science* **2016**, *351*, 681-684.

(31) van Asselt, R.; Elsevier, C. J.; Smeets, W. J. J.; Spek, A. L.; Benedix, R., *Recl. Trav. Chim. Pays-Bas* **1994**, *113*, 88-98.

(32) Gates, D. P.; Svejda, S. A.; Oñate, E.; Killian, C. M.; Johnson, L. K.; White, P. S.; Brookhart, M., *Macromolecules* **2000**, *33*, 2320-2334.

(33) (a) van Asselt, R.; Elsevier, C. J., *J. Mol. Catal.* **1991**, *65*, L13-L19; (b) Fedushkin, I. L.; Nikipelov, A. S.; Morozov, A. G.; Skatova, A. A.; Cherkasov, A. V.; Abakumov, G. A., *Chemistry* **2012**, *18*, 255-266; (c) Rumble, S. L.; Page, M. J.; Field, L. D.; Messerle, B. A., *Eur. J. Inorg. Chem.* **2012**, *2012*, 2226-2231.

(34) Fedushkin, I. L.; Skatova, A. A.; Cherkasov, V. K.; Chudakova, V. A.; Dechert, S.; Hummert, M.; Schumann, H., *Chem. Eur. J.* **2003**, *9*, 5778-5783.

(35) Li, L.; Lopes, P. S.; Rosa, V.; Figueira, C. A.; Lemos, M. A. N. D. A.; Duarte, M. T.; Aviles, T.; Gomes, P. T., *Dalton Trans.* **2012**, *41*, 5144-5154.

(36) (a) Coventry, D. N.; Batsanov, A. S.; Goeta, A. E.; Howard, J. A. K.; Marder, T. B., *Polyhedron* **2004**, *23*, 2789-2795; (b) El-Ayaan, U.; Murata, F.; El-Derby, S.; Fukuda, Y., *J. Mol. Struct.* **2004**, *692*, 209-216.

(37) (a) Gasperini, M.; Ragaini, F.; Gazzola, E.; Caselli, A.; Macchi, P., *Dalton Trans.* **2004**, 3376-3382; (b) Hill, N. J.; Vargas-Baca, I.; Cowley, A. H., *Dalton Trans.* **2009**, 240-253; (c) Kee, J. W.; Ng, Y. Y.; Kulkarni, S. A.; Muduli, S. K.; Xu, K.; Ganguly, R.; Lu, Y.; Hirao, H.; Soo, H. S., *Inorg. Chem. Front.* **2016**, *3*, 651-662.

(38) Papanikolaou, P.; Akrivos, P. D.; Czapik, A.; Wicher, B.; Gdaniec, M.; Tkachenko, N., *Eur. J. Inorg. Chem.* **2013**, 2418-2431.

(39) Gasperini, M.; Ragaini, F.; Cenini, S., *Organometallics* **2002**, *21*, 2950-2957.

(40) Hasan, K.; Wang, J.; Pal, A. K.; Hierlinger, C.; Guerchais, V.; Sen Soo, H.; Garcia, F.; Zysman-Colman, E., *Sci. Rep.* **2017**, *7*, 15520.

(41) Papanikolaou, P. A.; Tkachenko, N. V., *Phys. Chem. Chem. Phys.* **2013**, *15*, 13128-13136.

(42) (a) Crudden, C. M.; Allen, D. P., *Coord. Chem. Rev.* **2004**, *248*, 2247-2273; (b) Lin, J. C.; Huang, R. T.; Lee, C. S.; Bhattacharyya, A.; Hwang, W. S.; Lin, I. J., *Chem. Rev.* **2009**, *109*, 3561-3598; (c) Hopkinson, M. N.; Richter, C.; Schedler, M.; Glorius, F.,

Nature **2014**, *510*, 485-496; (d) Arduengo, A. J.; Harlow, R. L.; Kline, M., *J. Am. Chem. Soc.* **1991**, *113*, 361-363.

(43) (a) Gründemann, S.; Kovacevic, A.; Albrecht, M.; Faller Robert, J. W.; Crabtree, H., *Chem. Commun.* **2001**, 2274; (b) Gründemann, S.; Kovacevic, A.; Albrecht, M.; Faller, J. W.; Crabtree, R. H., *J. Am. Chem. Soc.* **2002**, *124*, 10473-10481.

(44) Guisado-Barrios, G.; Bouffard, J.; Donnadieu, B.; Bertrand, G., *Angew. Chem. Int. Ed.* **2010**, *49*, 4759-4762.

(45) Ung, G.; Bertrand, G., *Chem. Eur. J.* **2011**, *17*, 8269-8272.

(46) Son, S. U.; Park, K. H.; Lee, Y. S.; Kim, B. Y.; Choi, C. H.; Lah, M. S.; Jang, Y. H.; Jang, D. J.; Chung, Y. K., *Inorg. Chem.* **2004**, *43*, 6896-6898.

(47) Mathew, P.; Neels, A.; Albrecht, M., *J. Am. Chem. Soc.* **2008**, *130*, 13534-13535.

Chapter 2

Development of Bis(arylimino)acenaphthene (BIAN) Copper Complexes

2.1 Foreword

Chapter 2 discusses our efforts in the synthesis and characterization of new Cu^{I} photosensitizers with Ar-BIAN as the ligand system. The application of these new Cu^{I}-Ar-BIAN complexes synthesized will be discussed in Chapter 3. Both chapters are based on the work published in *Inorganic Chemistry Frontiers* (*Inorg. Chem. Front.*, **2016**, *3*, 651) and reproduced by permission of The Royal Society of Chemistry.[1] Dr. Kee was the first author on this paper while I was the second. I assisted Dr. Kee in the syntheses and characterizations of all the compounds. Dr. Kulkarni and Dr. Muduli were involved in the incorporation of the newly synthesized complexes into DSSCs and they collected the measurements obtained from the device testing. Dr. Xu was instrumental in the computational studies performed. Dr. Ganguly perfomed all the crystallographic analysis.

Development of Bis(arylimino)acenaphthene (BIAN) Copper Complexes as Visible Light Harvesters for Potential Photovoltaic Applications

Jun Wei Kee, Yik Yie Ng, S. A. Kulkarni, S. K. Muduli, Kai Xu, Rakesh Ganguly, Yunpeng Lu,* Hajime Hirao,* and Han Sen Soo*

2.2 Abstract

Photovoltaics with DSSCs have been recognized as being promising for the utilization of sunlight to produce electricity and 'solar chemicals'. One of the remaining unsolved challenges is the development of an affordable, robust dye that has a panchromatic light harvesting range and efficiently provides separated charges for the desired photochemistry. The most commonly employed molecular photosensitizers include the noble metal-based ruthenium and iridium complexes, synthetically challenging porphyrin derivatives, and expensive, functionalized polypyridine compounds. Here, we describe the development of Cu^{I} dyes supported by Ar-BIAN ligands, which can be synthesized in fewer than three steps from affordable, commercially available reagents. The diamagnetic, homoleptic complexes have been characterized by a suite of spectroscopic and analytical methods and exhibit panchromatic light absorption extending to the NIR region. Remarkably, the crystal structure of a complex bearing an ortho-iodoarylimino substituent displays a unique,

rhombically distorted square planar geometry around the Cu^{I} center, for crystals isolated from two disparate solvent combinations. DFT calculations were performed to provide insights into the spectroscopic features and the unusual coordination sphere around the metal center, and allude to noncovalent interactions between the aromatic groups and among the iodide atoms. Preliminary studies were conducted to explore the application of these copper photosensitizers in dye-sensitized solar cells.

2.3 Introduction

There has been growing interest in the use of photoredox catalysis as a sustainable means to mediate organic chemical transformations by harvesting visible light as a source of energy.[2] Numerous seminal studies have been documented recently for novel, chemoselective, photodriven, and mild routes to C-C bond formation.[2a, 2b, 3] However, as discussed in section 1.3, the adopted photocatalysts have been predominantly expensive Ru- and Ir-based photosensitizers,[2a, 2b, 3f, 4] although there have been sporadic reports on the employment of organic or Cu^{I} dyes.[2c, 3a, 3c, 3i] Likewise, for DSSCs and the nascent field of dye-sensitized photoelectrosynthesis cells (DSPECs), functionalized Ru^{II} polypyridyl photosensitizers have remained the *workhorse* for several decades, despite the high cost and low abundance of Ru.[5] Inspired by the paucity of research on photosensitizers containing earth-abundant first-row transition metals,[3a, 3c, 3d, 3h, 3i, 6] we sought to develop new Cu^{I} visible light harvesters.

Similar to the ubiquitous Ru^{II} dyes, Cu^{I} photosensitizers with polypyridine ligands in the form of 2,2′-bpy and phen derivatives have received the most attention with a number of examples given in section 1.3.2.[3a, 6d, 6f, 7] Cu^{I} polypyridyl complexes have d^{10} electronic configurations and possess comparable photophysical characteristics as Ru^{II} chromophores since they are not plagued by as many non-radiative relaxation losses through low-energy d–d transitions that are common among first row transition metals. By using suitable π-acceptor ligands such as pyridines, Cu^{I} compounds can absorb visible light through MLCT processes.[3a, 6d, 6f, 7] However, a transient Cu^{I} to Cu^{II} conversion typically results in significant Jahn–Teller (J–T) distortions, unlike the minimal reorganization after a Ru^{II} to Ru^{III} transition, which can lead to undesired non-radiative losses. Although some of these Cu^{I} polypyridyl complexes have notably long lifetimes, the more successful, bulky polypyridyl ligands are notoriously expensive, require demanding multi-step syntheses, and typically yield Cu^{I} complexes that do not

absorb much red and longer wavelength irradiation.[3a, 6d, 6f, 7] In contrast, Ar-BIAN ligands are highly modular and readily accessible by facile condensation reactions between commercially available and affordable substituted anilines and acenaphthenequinone.[1, 6i, 8] Ar-BIAN ligands have been explored and reviewed in the context of transition metal and main-group molecular compounds.[1, 6i, 8] They have been established as redox non-innocent ligands with low-lying π* orbitals that can behave as 'capacitors' for multi-electron reductions.[9] Moreover, Ar-BIAN ligands are acknowledged as robust scaffolds for catalysis and even photovoltaic devices.[8d, 10] Critically, pioneering work on Cu^{I} Ar-BIAN complexes verified that judicious selection of the arylimino component or an appropriate co-ligand can generate panchromatic Cu^{I} dyes, which can absorb in the NIR region.[1, 6i, 8d, 10a, 10b, 11]

In the following sections, the synthesis, experimental characterization, and DFT studies on new panchromatic Ar-BIAN Cu^{I} compounds will be discussed. Attempts were made to prolong the lifetime of the MLCT photoexcited state by introducing heavier halogens on the ligand periphery to harness the heavy-atom effect. In particular, the observation of an unusually flat coordination sphere of Cu^{I} may have interesting implications on the photochemistry as discussed previously by Iwamura *et al.*[6f] In anticipation of potential applications in DSSCs and DSPECs, we have installed sulfonate[12] and ester groups[13] on the ligands to serve as anchoring groups and charge conduits into semiconductors. The testing of these devices and the results obtained will be further discussed in the next chapter.

2.4 Results and Discussion

2.4.1 Design and Synthesis of Ar-BIAN Ligands (2.1 – 2.2)

The synthetic steps for the two substituted Ar-BIAN ligands are illustrated in Scheme 2.1 and detailed characterization data can be found in section 2.6.2. Briefly, template-free methods, namely the acid-catalyzed synthesis[14] of Na(Ar^{SO_3}-Br-BIAN) (**2.1**) and the $TiCl_4$-promoted condensation[15] leading to $Ar^{I,COOMe}$-BIAN (**2.2**), were adapted to give moderate yields. These synthetic methods were chosen over the more popular $ZnCl_2$-templated route to avoid complications with hydrolysis and purification issues during the extraction of zinc with sodium oxalate.[8b]

Scheme 2.1 Synthetic routes for ligands **2.1** and **2.2**.

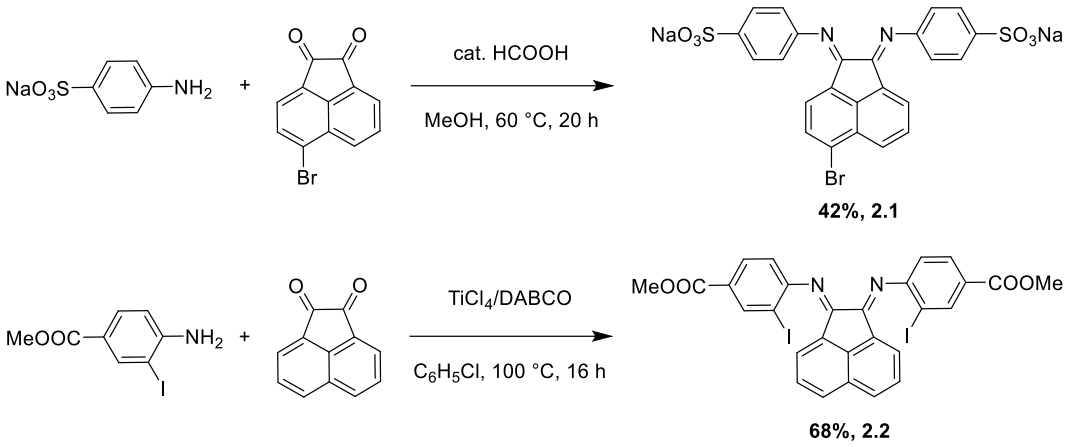

2.4.2 Isomerism for 2.2

Both the (*E*,*E*)- and (*E*,*Z*)-isomers for **2.2** (Figure 2.1) were present in the $CDCl_3$ solution in a ratio of around 2 : 1 respectively, as suggested by the broad peaks in the ^1H NMR spectrum of **2.2** at room temperature.

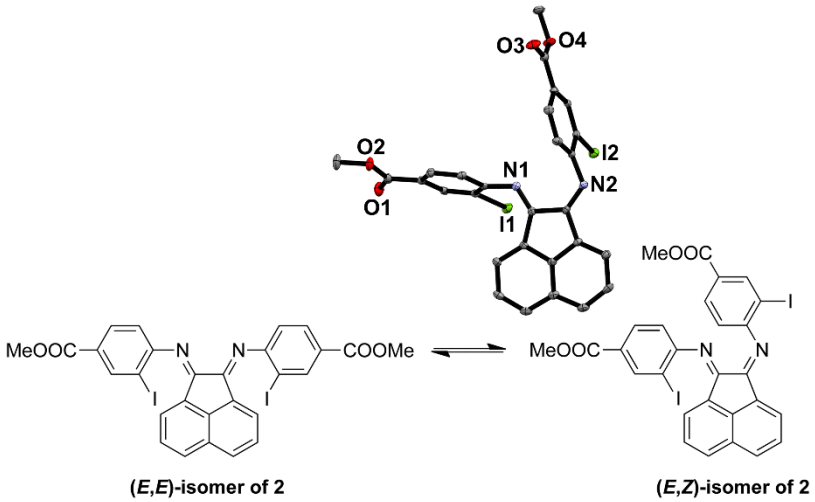

Figure 2.1 (*E*,*E*)- and (*E*,*Z*)-isomeric forms of **2.2**.

The broadening is likely due to the thermal exchange between the two isomers under ambient conditions. This isomerism has been previously reported by Gasperini *et al.* whereby they observed the presence of two isomers at 183 K for their Ar-BIAN ligand.[8b] It is therefore likely that at very low temperatures the isomerization still occurred in solution. Since there are no solvents that remains liquid at 100 K, we cannot verify this experimentally. Variable temperature (VT) NMR experiments at low (Figure 2.2) and

high (Figure 2.3) temperatures were conducted in $CDCl_3$ to obtain the thermodynamic parameters of this isomeric equilibrium of **2.2**. Compound **2.2** was dissolved in $CDCl_3$ and sealed in a J. Young NMR tube. In order to collect the ^1H NMR spectra at various temperatures between 333K and 223K (Figures 2.2 and 2.3), the tube was inserted into a temperature-controlled NMR probe before leaving the sample to equilibrate for 10 min at the desired temperature. The exact temperatures are indicated in the stack plots of Figures 2.2 and 2.3. Through the relative concentrations of the two isomers, obtained from the relative integration of peaks belonging to (*E,E*)-isomer (doublet at δ = 8.66 ppm, corresponding to two protons) and (*E,Z*)-isomer (doublet at δ = 6.65 ppm, corresponding to one proton), the equilibrium constants for the isomerization from the (*E,E*)-isomer to the (*E,Z*)-isomer at each temperature can be determined by the following expression:

$$K_{eq} = \frac{[(E,Z)-isomer]}{[(E,E)-isomer]}.$$

Subsequently, a Van't Hoff plot of $\ln K_{eq}$ as a function of T^{-1} as shown in Table 2.1 was fit to a line according to the expression:

$$\ln K_{eq} = -\frac{\Delta H°}{RT} + \frac{\Delta S°}{R}$$

where $\Delta H°$ and $\Delta S°$ have been determined to be +13.3 kJ mol^{-1} and +39.0 J mol^{-1} K^{-1} respectively (Table 2.1 and Figure 2.4). The conversion of (*E,E*)-**2.2** to (*E,Z*)-**2.2** is endothermic with the (*E,Z*)-isomer being the product of the equilibrium, while (*E,E*)-**2.2** is the starting material. NMR experiments at elevated temperatures (Figure 2.3) indicated that the coalescence temperature is 333 K in $CDCl_3$.

Table 2.1 Experimental data and calculated reaction enthalpy (ΔH°), entropy (ΔS°), and free energies (ΔG°) for the isomerization of (*E*,*E*)-**2.2** to (*E*,*Z*)-**2.2**

Reaction: (*E*,*E*)-**2.2** ⇌ (*E*,*Z*)-**2.2**						
T/ K	$\frac{1}{T}$/ × 10^{-3} K^{-1}	K_{eq}	ln K_{eq}	ΔH°/ kJ mol^{-1}	ΔS°/ J mol^{-1} K^{-1}	ΔG°/ kJ mol^{-1}
273	3.67	0.322	-1.13			+2.65
263	3.80	0.242	-1.42			+3.04
253	3.95	0.188	-1.67	+13.3	+39.0	+3.43
243	4.12	0.148	-1.91			+3.82
233	4.29	0.114	-2.17			+4.21
223	4.48	0.084	-2.48			+4.60

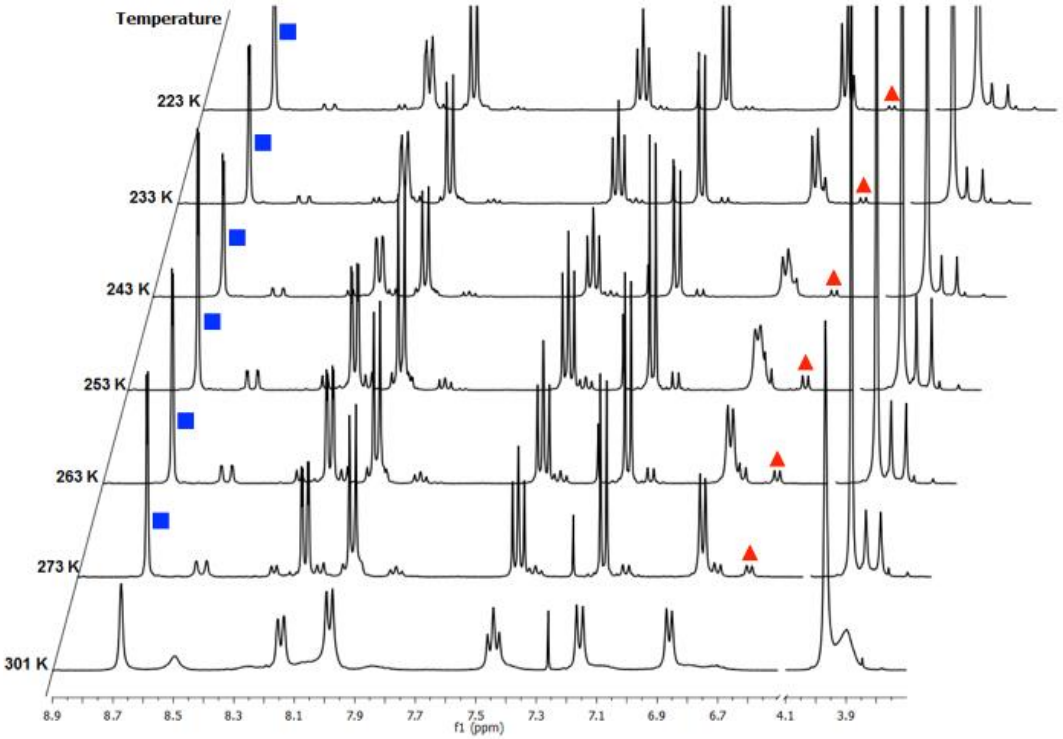

Figure 2.2 Low temperature ^{1}H NMR spectra of **2.2** in $CDCl_3$ between 223 and 301 K. The solvent residual peak is at 7.26 ppm (singlet). The signal for the (*E*,*E*)-isomer used in the Van't Hoff plot is represented by the blue squares, while the signal for the (*E*,*Z*)-isomer is represented by red triangles.

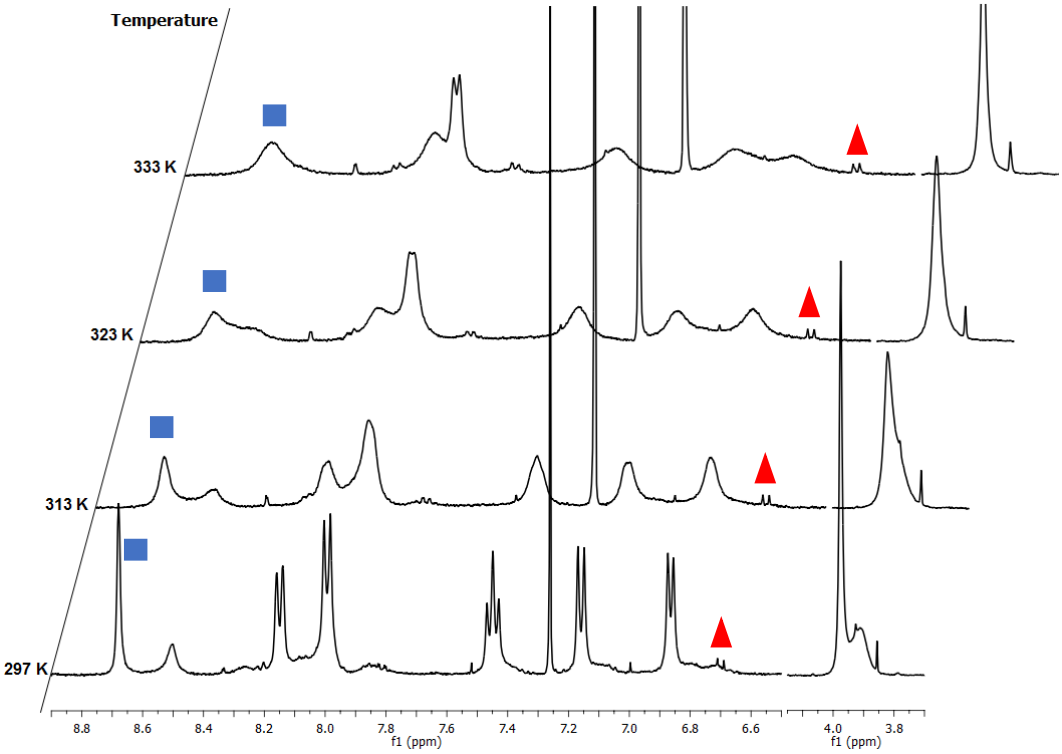

Figure 2.3 High temperature ^{1}H NMR spectra of **2.2** in $CDCl_3$ between 301 and 333 K. The solvent residual peak is at 7.26 ppm (singlet). The signal for the (*E*,*E*)-isomer used in the Van't Hoff plot is represented by the blue squares, while the signal for the (*E*,*Z*)-isomer is represented by red triangles.

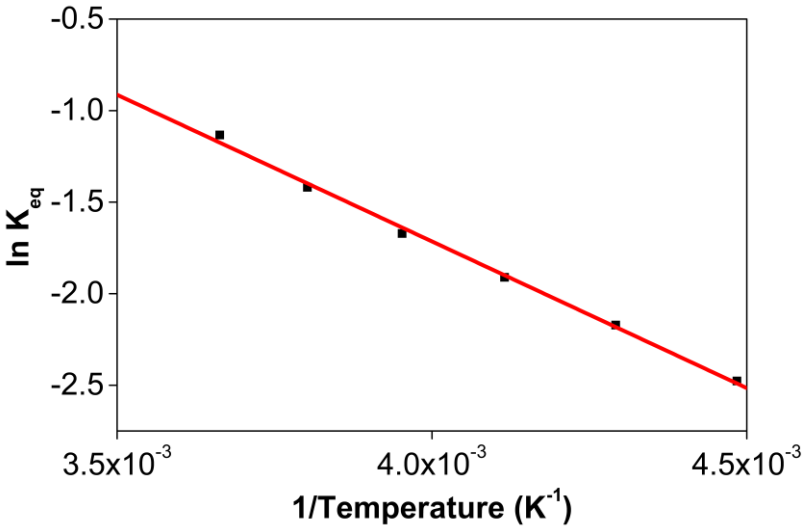

Figure 2.4 Van't Hoff plot for the isomerization equilibrium between the *(E,E)*-isomer and the *(E,Z)*-isomer.

The solid-state structure was obtained to confirm the identity of **2.2** with single crystals grown from methanol (MeOH)/dichloromethane (DCM) and the *(E,Z)*-isomer of **2.2** was isolated (Figure 2.1). For a clearer display of the *(E,Z)*-isomer geometry, the space filling model is shown in Figure 2.5. Notably, the *(E,Z)*-isomerism does not impede the coordination of Cu^{I}, since the Cu^{I} complexes bound to the thermally more stable (*E,E*) form was isolated and characterized in high yields, presumably due to facile isomerization between the two isomers at room temperature.

The *(E,Z)*-isomer was isolated in the solid state probably due to π-π interaction in the solid state. Gasperini *et al.* also reported the observation of the (*E,Z*)-isomer and they proposed the onset of π-π charge transfer interaction thereby stabilizing the isomer.[8b] Also, DFT studies performed by Rosa *et al.* revealed that both conformers are isoenergetic, and both can be obtained experimentally, with the (*E,Z*)-isomer to be slightly more stable by 0.06 kJ mol^{-1}. Each of the (*E,Z*)-isomer is joined to seven neighboring molecules through C-H•••π interactions to generate a complicated 3D organization.[16]

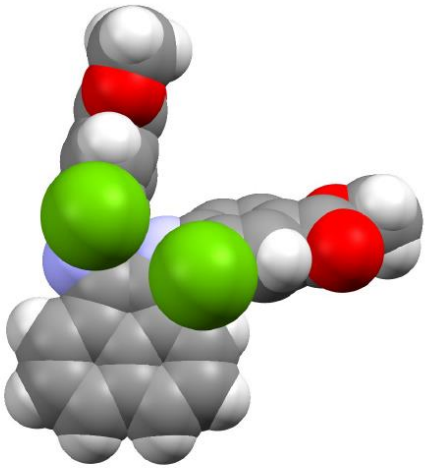

Cu: orange; C: grey; I: green; N: blue; O: red

Figure 2.5 Space-filling model of **2.2** from single crystal X-ray diffraction experiments.

2.4.3 Preparation of Cu^{I} Complexes (2.3 – 2.4)

The synthetic steps for the two Ar-BIAN Cu^{I} complexes (**2.3** and **2.4**) are illustrated in Scheme 2.2. Upon mixing two equivalents of **2.1** with CuCl in dimethyl sulfoxide (DMSO), a dark blue-colored solution formed within 1 h. The solution was filtered, and the product was isolated by precipitation from the filtrate by adding acetonitrile (ACN). The residue was purified by recrystallization from DMSO/ACN to obtain $Na_3[(Ar^{SO}{}_3$-

Br-BIAN)$_2$Cu] (**2.3**). The single crystals of **2.3** were not successfully obtained to confirm the structure. However, the ^{1}H and ^{13}C NMR spectra, as well as the electrospray ionization-mass spectrum (ESI-MS) were consistent with the assignment of **2.3** as a homoleptic cuprate complex supported by two units of the ligand **2.1**.

Scheme 2.2 Synthetic routes for complexes **2.3** and **2.4**.

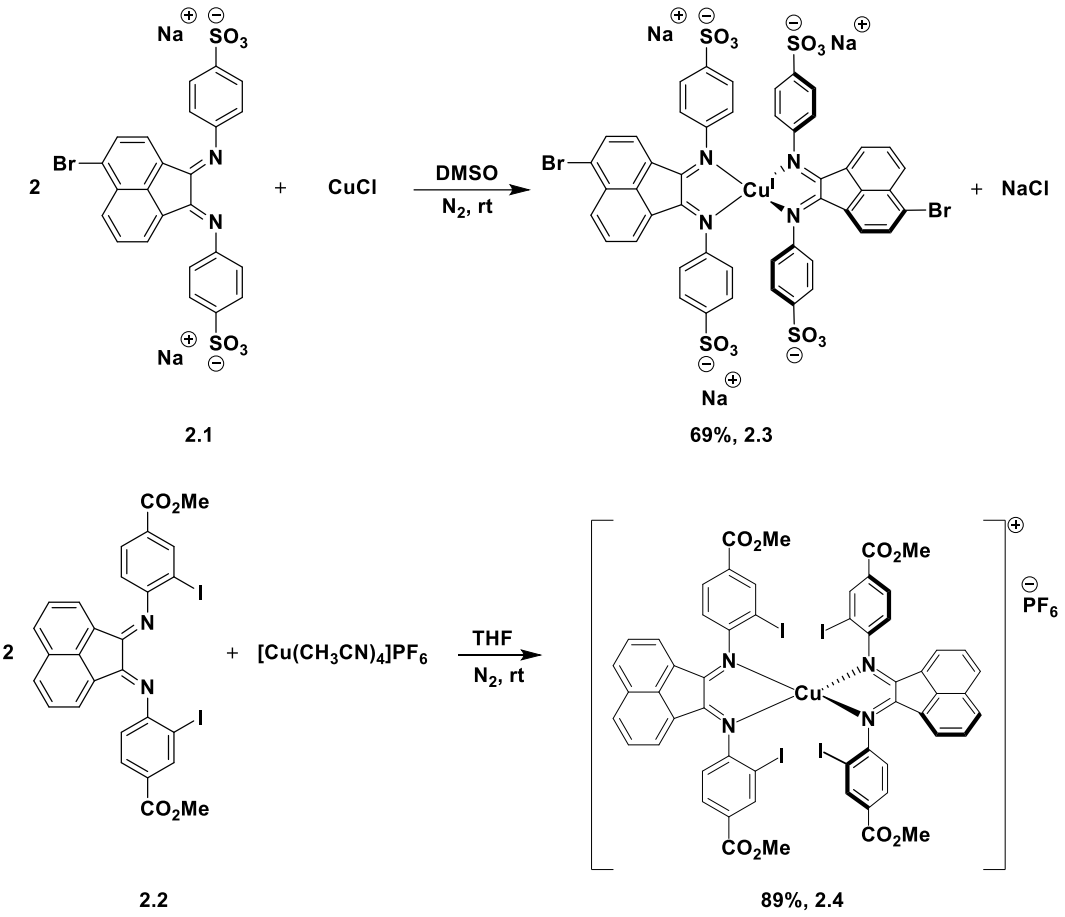

Since ligand **2.2** was more souble, the complex [(Ar^{I,COOMe}-BIAN)$_2$Cu]PF$_6$ (**2.4**) was prepared by using another Cu^I precursor, namely [Cu(CH$_3$CN)$_4$]PF$_6$, in tetrahydrofuran (THF) and the product was precipitated with pentane as a dark green material. Through recrystallization from THF/toluene, dark green crystals suitable for X-ray structural analyses were obtained (Figure 2.6). Complex **2.4** crystallized in the triclinic space group $P\bar{1}$ (Table 2.7).

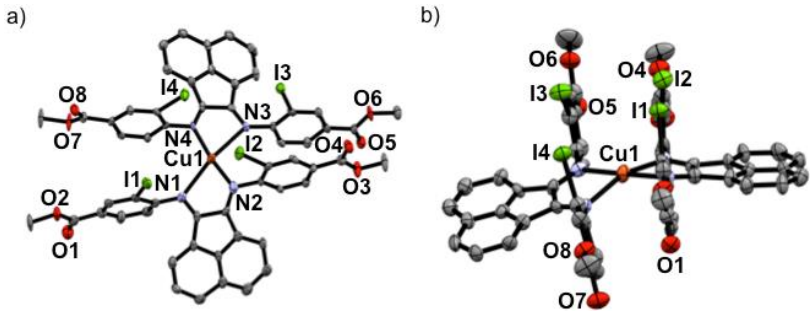

Figure 2.6 Oak Ridge Thermal Ellipsoid Plots (ORTEPs) from single crystal X-ray diffraction experiments of **2.4**. Top (a) and side views (b) of crystals grown from THF/toluene. The PF_6-counteranion and the calculated hydrogen atoms are omitted for clarity. The thermal ellipsoids are at 50% probability.

The crystal structure of **2.4** in Figure 2.6 displays a rhombically distorted square planar coordination sphere around the Cu^I center when chelated by two molecules of the ligand **2.2**, with a PF_6^- counteranion. This is in stark contrast to the typical distorted tetrahedral geometry of Cu^I Ar-BIAN complexes reported previously.[8d, 10b] One measure of the deviation from a tetrahedral geometry about Cu^I is the dihedral angle[10b] between the two five-membered chelate rings and this was found to be 21.2(3)° in **2.4**, which is much smaller than those reported previously (55.3–89.4°).[8d, 10b] To determine if the unique coordination sphere observed was due to the solvents used for the recrystallization, a different solvent combination of DCM/diethyl ether (Et_2O) was used to recrystallize **2.4**. Albeit with a larger dihedral angle of 32.0(3)°, the coordination sphere still approximates a distorted square planar geometry (Figure 2.7a and 2.7b). The space filling models of the crystals recrystallized from different solvent combinations are also shown in Figure 2.7c-f. It is evident from these models that the isolated crystals possessed a distorted square planar geometry. Other salient parameters are summarized in Table 2.2.

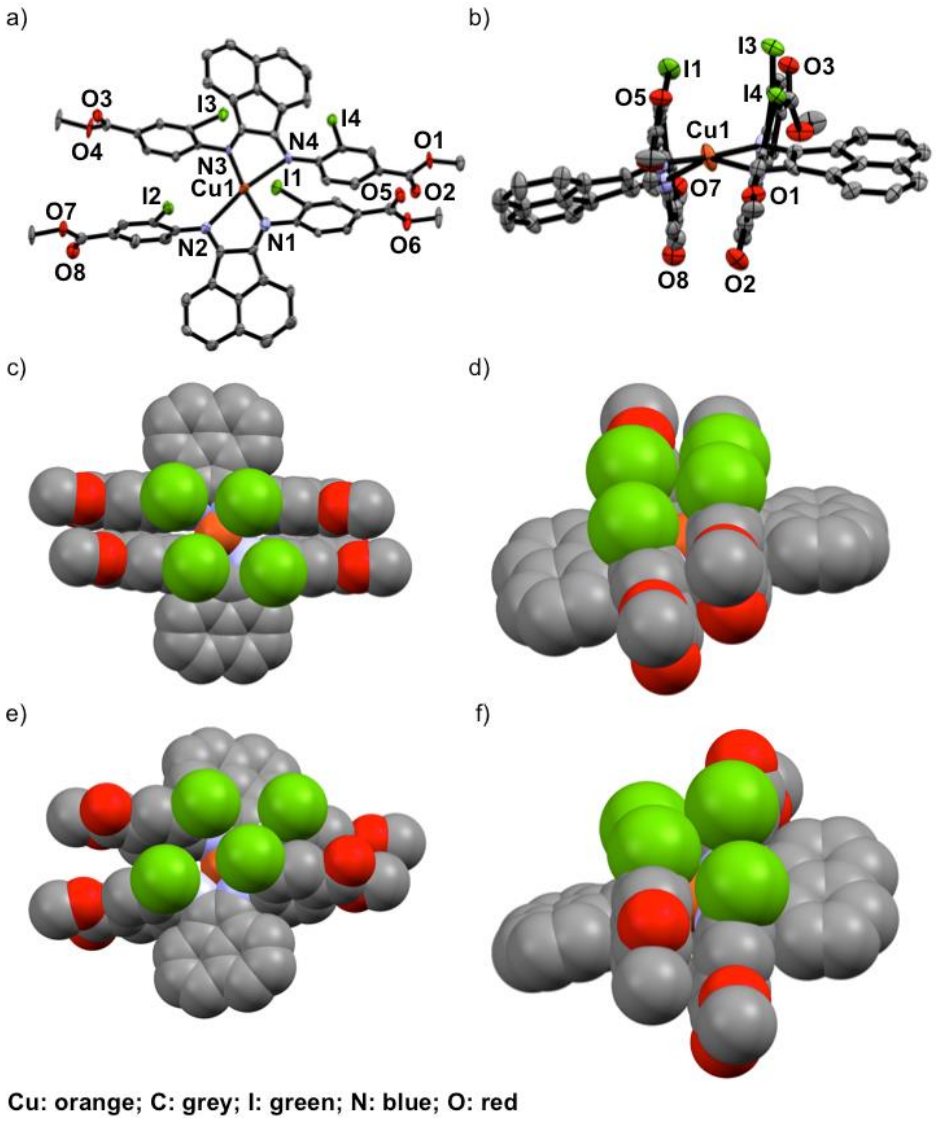

Figure 2.7 ORTEPs from single crystal X-ray diffraction experiments of **2.4**. Top a) and side views b) of crystals grown from DCM/Et_2O. The thermal ellipsoids are at 50% probability. Space-filling model of **2.4** from the crystal structures. Top ((c) and (e)) and side views ((d) and (f)) of the crystals grown from THF/toluene and DCM/Et_2O respectively. The PF_6^- counteranion and the calculated hydrogen atoms are omitted for clarity.

In addition, dramatic asymmetry in the way each unit of **2.2** binds to Cu^I is evident regardless of the crystal growth solvent combination employed. The structures presented are drastically different from the more symmetric homoleptic Ar-BIAN Cu^I complexes in prior publications. For the sake of clarity, the discussions below correspond to the crystals grown out of THF/toluene, unless stated otherwise.

Table 2.2 Selected covalent and non-covalent bond distances [Å] and angles [°] for **2.4**, grown from different solvent combinations.

Parameter	**THF/toluene**	**DCM/Et_2O**
Cu1-N1	1.938(11)	1.907(9)
Cu1-N2	2.463(11)	2.460(9)
Cu1-N3	1.931(11)	1.892(7)
Cu1-N4	2.517(13)	2.645(9)
C1-N1	1.268(14)	1.288(16)
C11-N2	1.262(13)	1.253(16)
C29-N3	1.287(13)	1.305(17)
C39-N4	1.272(13)	1.298(16)
I1-I2	4.354(2)	4.984(2)
I2-I3	4.276(2)	4.857(2)
I3-I4	4.621(2)	5.144(2)
I1-I4	4.309(2)	4.524(2)
I1-I3	4.829(2)	4.110(1)
N1-Cu1-N2	76.5(4)	76.1(4)
N3-Cu1-N4	75.8(4)	74.6(3)
Dihedral angle between chelate rings	21.2(3)	32.0(3)
Dihedral angles between acenaphthene and *o*-iodoaryl rings	89.5(4), 84.9(3), 82.6(3), 89.7(4)	71.2(3) 79.9(3), 82.7(3), 87.9(3)
o-iodoaryl centroid-centroid distances	3.615, 3.622	3.719, 4.381

It was observed from Table 2.2 that the C-N bond lengths are not lengthened as compared to previously reported Ar-BIAN Cu complexes. [8d, 10b, 11b] For example, Papanikolaou *et al.* reported C-N bond lengths ranging from 1.274(4) to 1.294(5) Å.[8d] This likely indicates that the ligands are not reduced after complexation. However, the Cu–N bond lengths are different for each ligand. For example, the Cu–N bond distances are 1.931(11) and 2.517(13) Å for one of the ligands, while the other distances are 1.938(11) Å and 2.463(11) Å. In the previously documented homoleptic Cu^I Ar-BIAN complexes, the typical Cu–N bond lengths are in a narrower range of 1.98–2.06 Å.[8d, 10b] Evidently, for each coordinated **2.2**, one nitrogen atom has an almost expected value, whereas the second nitrogen atom is only weakly coordinated. The longer than expected Cu-N bond lengths may be due to the poor overlap of the nitrogen lone pair orbitals with those of the metal similar to the long Cu-N bond lengths observed by Doherty *et al.*[17] The coordination geometry surrounding the Cu^I can arguably be considered as being *linear*. A survey of complexes with Cu–N bond distances longer than 2.40 Å suggests that the majority involved Cu^{II} centers with axially lengthened octahedral geometries due to a first-order Jahn–Teller effect. Six examples of Cu^I complexes with at least one

Cu–N bond length above 2.40 Å were found in the Cambridge Structural Database (CSD), all of which feature neutral amine or heterocycle donors.[17-18] Out of these instances, one consists of a distorted octahedral Cu^{I},[18d] two possess trigonal monopyramidal Cu centers with long axial bonds,[17, 18c] while the remaining two have been described as distorted square planar or sawhorse geometries.[17-18] In particular, the bis(amino-oxazoline) Cu^{I} complex reported by Doherty *et al.* has exceptionally long Cu–N bonds of 2.640(5) and 2.838(5) Å, which have been aptly considered as weak interactions between the Cu and aniline ligands.[17] Since the sum of the van der Waals radii of Cu^{I} and N is 2.90 Å, **2.4** joins a class of rare Cu^{I} complexes containing weak Cu–N interactions.[17]

The pendant *o*-iodoaryl rings appear to be almost perpendicular to the acenaphthene ring, and the dihedral angles among the two contiguous aryl rings varied between 71.2(3) and 89.7(4)°. This is unlike most of the known homoleptic Cu^{I} Ar-BIAN complexes. Furthermore, the four ortho-iodides on the two ligands are in close proximity with one another on the same face of **2.4**, with distances between 4.276 and 4.621 Å. The steric pocket surrounding the Cu^{I} is most patently observed in the space-filling model (Figure 2.7). This alludes to some non-covalent electronic interactions that may favour this unusual arrangement among these iodide atoms or between the iodides and Cu, since the geometry is mostly independent of the crystal growth solvent. Steric effects are unlikely to be the sole reason because crystal structures of Cu^{I} compounds with (*o*-isopropyl)aryl-BIAN ligands have shown tetrahedral coordination spheres, and the isopropyl groups orientate themselves to minimize steric hindrance by being far apart.[10b]

Another factor that might affect the orientation of the *o*-iodoaryl rings, and hence the overall coordination sphere of Cu^{I}, is the π–π interactions between the aryl rings. The *o*-iodoaryl moieties within **2.4** are aligned parallel to each other with offset centroid–centroid distances of 3.615 and 3.622 Å between the aryl groups, for the crystal grown from THF/toluene. However, longer centroid–centroid distances (3.719 and 4.381 Å) were observed in the crystal grown out of DCM/Et_2O, which is inconsistent with a dominant π–π interaction between the aryl rings to account for the remarkably flat coordination geometry around the Cu^{I} center. The structural data suggests that novel electronic or steric reasons originating from the ortho-iodides are contributing to the unusual coordination geometry of **2.4**, and the effect does not solely arise from crystal-packing forces in disparate solvents. In combination with the exceptionally long Cu–N

bond distances in the complex, **2.4** possesses a truly unique rhombically distorted square planar Cu^{I} center. To explain this unusual phenomenon, and also several remarkable UV-visible features, we sought insights from DFT calculations (*vide infra*). Additional x-ray data about these crystal structures are described in section 2.7.

2.4.4 Electrochemical Measurements of 2.1 – 2.4

Cyclic voltammetric techniques were employed to probe the redox behavior of the Ar-BIAN ligands and the complexes in DMSO/*N*,*N*-dimethylformamide (DMF) 1 : 1 (v : v), containing 0.10 M tetrabutylammonium tetrakis[3,5-bis(trifluoromethyl) phenyl]borate (n-$Bu_4NBAr^F{}_4$). The choice of solvents used was due to **2.1** and **2.3** being unable to dissolve in non-coordinating solvents such as 1,2-difluorobenzene or DCM. All potentials (Table 2.3) reported and discussed subsequently are referenced against the ferrocenium ion/ferrocene redox couple (Fc^+/Fc).

Table 2.3 Electrochemical data[a] for **2.1** – **2.4**

Compound	E_p^{ox} / E_p^{red} (V *vs* Fc^+/Fc)			
	2.1	**2.2**	**2.3**	**2.4**
Ligand oxidations	+0.38/– +0.71/–	–	–	–
Ligand reductions	-1.20/-1.68 –/-2.24	-1.36/-1.41[b] -2.18/-2.27 -2.35/-2.40	-1.08/-1.16[c] -1.37/-1.46 -1.59/-1.84 –/-2.05	-0.62/-0.96 –/-1.21 -1.30/-1.37[d] -2.10/-2.28 -2.34/-2.39
Cu^I oxidation	–	–	-0.08/-0.38	-0.33/-0.42

[a] E_p^{ox} and E_p^{red} represent the oxidation and reduction peak potentials respectively and are reported in V *versus* Fc^+/Fc. [b] An additional oxidation wave at -0.86 V is associated with this ligand reduction. [c] An additional oxidation wave at -0.72 V is associated with this ligand reduction. [d] An additional oxidation wave at -0.02 V is associated with this ligand reduction.

When comparing with similar Ar-BIAN ligands reported previously, there were at least two reductions (−1.78 to −1.93 V and −2.37 to −2.55 V) and two oxidations (+0.22 to +0.97 V and +1.07 to +1.82 V) that were commonly observed.[8b-d] The electrochemical behavior of **2.1** in DMF/DMSO consists of a series of irreversible reductions and oxidations. The cathodic scan of **2.1** reveals two irreversible reduction waves at −1.68 V and at −2.24 V (Figure 2.8a). When an anodic scan was performed, two irreversible oxidations appeared at +0.38 and +0.71 V and upon the reverse cathodic scan up to

−2.60 V, an additional reduction wave at −0.76 V appeared (Figure 2.8b), indicating that significant structural change or decomposition occurred during the oxidation of **2.1**. However, this additional reduction wave may also be due to unavoidable solvent oxidation by-products, due to the limited solvent choices for the ionic **2.1**.

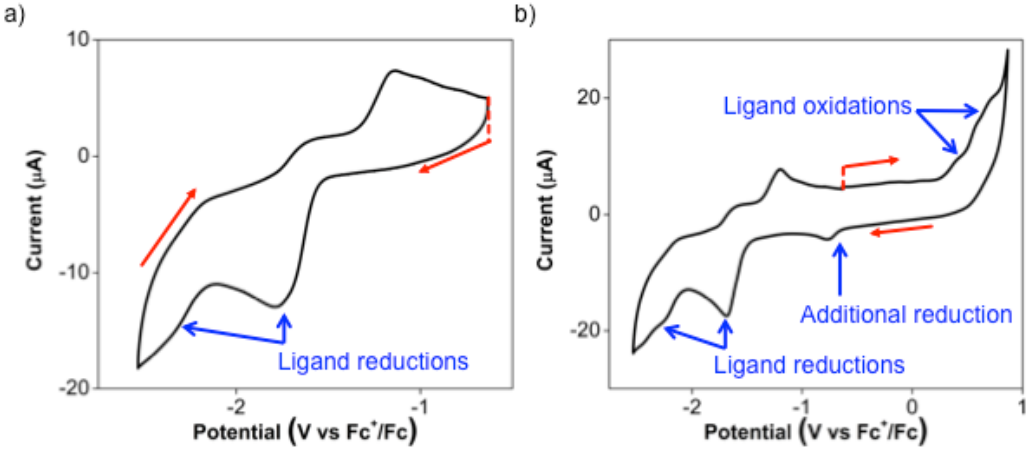

Figure 2.8 Cyclic voltammograms of 1.0 mM of **2.1**, with 0.10 M ***n*-Bu$_4$NBAr$^F{}_4$** as the electrolyte in **DMSO/DMF 1:1 (v/v)**, each at a scan rate of 100 mV s^{-1}, within the potential windows of a) -2.6 to +0.9 V, and b) -2.6 to -0.6 V respectively, relative to Fc$^+$/Fc. The red arrows indicate the scan directions, with red vertical lines indicating the initial potentials for each scan. The blue arrows indicate the ligand redox events of **2.1**.

The electrochemistry of **2.2** in DMF/DMSO can be compared to that reported for the structurally similar *p*-(methylester)aryl-BIAN.[8c] When the cathodic scan of **2.2** was performed, three irreversible reduction waves appeared at −1.41, −2.27 and −2.40 V before the onset of solvent reduction (Figure 2.9a). The first wave at −1.41 V appears to be a two-electron reduction process and has two oxidation waves at −0.86 and −1.36 V associated with it. In addition, these three waves are similar to that reported for *p*-(methylester)aryl-BIAN (−1.68 and −2.23 V). Within the electrochemical window accessible for the DMF/DMSO combination (+0.8 to −2.6 V) before solvent redox events occur, we were unable to access the electrochemical oxidation potentials of **2.2**. The electrochemical oxidation is accessible when the cyclic voltammetry is conducted in THF instead. An irreversible oxidation wave was observed at +0.94 V before the oxidation of the THF solvent at higher potentials (Figure 2.9d). This potential is slightly higher than that reported for *p*-(methylester)aryl-BIAN (+0.82 V) and could be due to the electron-withdrawing effect of the ortho-iodides, thus raising the oxidation potential slightly.

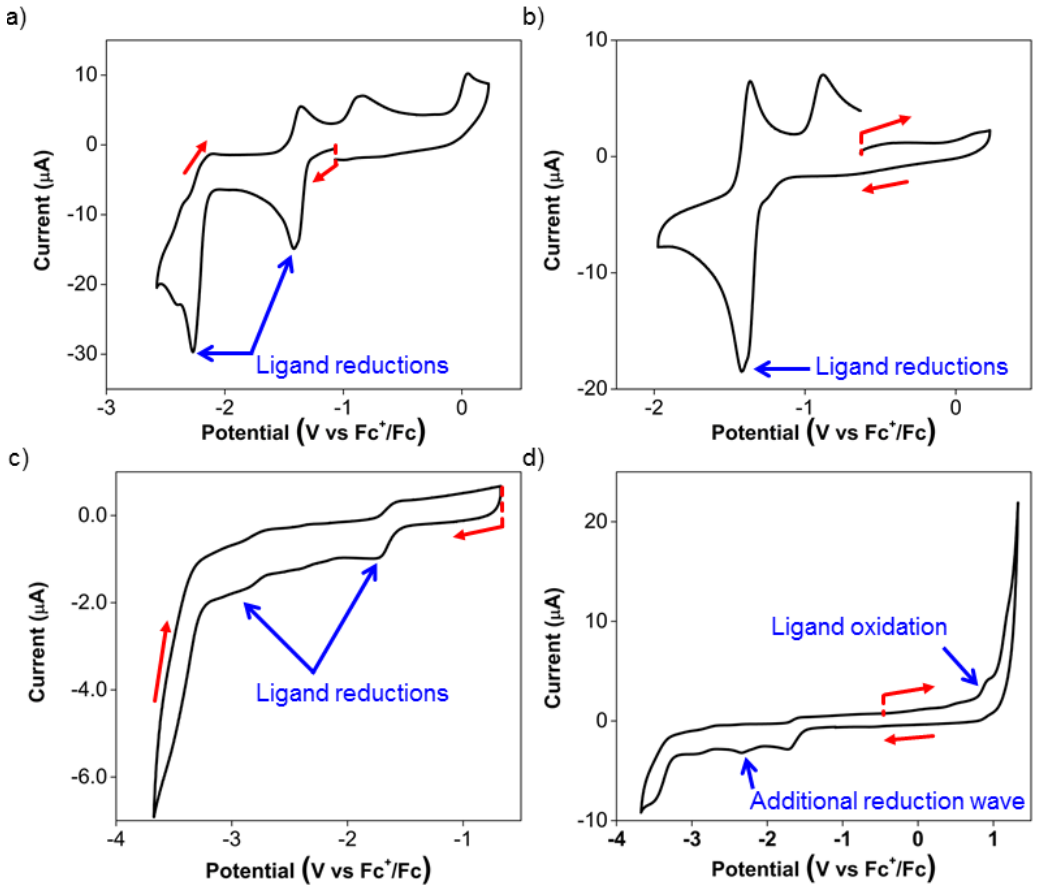

Figure 2.9 Cyclic voltammograms of 1.0 mM of **2.2**, with 0.10 M ***n*-Bu$_4$NBAr$^F{}_4$** as the electrolyte in **DMSO/DMF 1:1 (v/v)**, each at a scan rate of 100 mV s^{-1}, within the potential windows of a) -2.6 to +0.3 V, and b) -1.9 to +0.3 V respectively, relative to Fc$^+$/Fc. Additional cyclic voltammograms were performed similarly with 0.10 M ***n*-Bu$_4$NPF$_6$** as the electrolyte in **THF** instead, within the potential windows of c) -3.7 to -0.7 V and d) -3.7 to +1.3 V respectively, relative to Fc$^+$/Fc. The red arrows indicate the scan directions, with red vertical lines indicating the initial potentials for each scan. The blue arrows indicate the ligand redox events of **2.2** as well as additional reduction waves that appear after reversing the anodic scan in d).

An additional reduction wave at −2.36 V was observed in the return cathodic scan (Figure 2.9d) suggesting that oxidation of **2.2** in THF results in significant chemical transformations and changes to the electrochemical properties of **2.2**. In addition, the cathodic scan in THF (Figure 2.9c) reveals a more negative potential of −2.86 V for the second reduction instead. It is likely that this electrochemical reduction is complicated by the reductive de-iodination of the iodoaryl moiety, since it is close to the reported reduction potential of −2.64 V for iodobenzene.[19]

The Cu^{I} complexes exhibit more complicated voltammograms than the ligands, with additional reduction and oxidation processes owing to the presence of the Cu^{I} center.[8d] For **2.3**, the anodic scan revealed two overlapping oxidation peaks before the onset of solvent oxidation (Figure 2.10a). The redox wave was quasi-reversible at −0.08 V with a cathodic return wave at −0.38 V (Figure 2.10a). These potentials are similar to those previously reported for Cu^{I} Ar-BIAN homoleptic complexes and have been ascribed to Cu^{I}/Cu^{II} oxidations that involve donation from the iminyl moiety of the Ar-BIAN ligands.[8d]

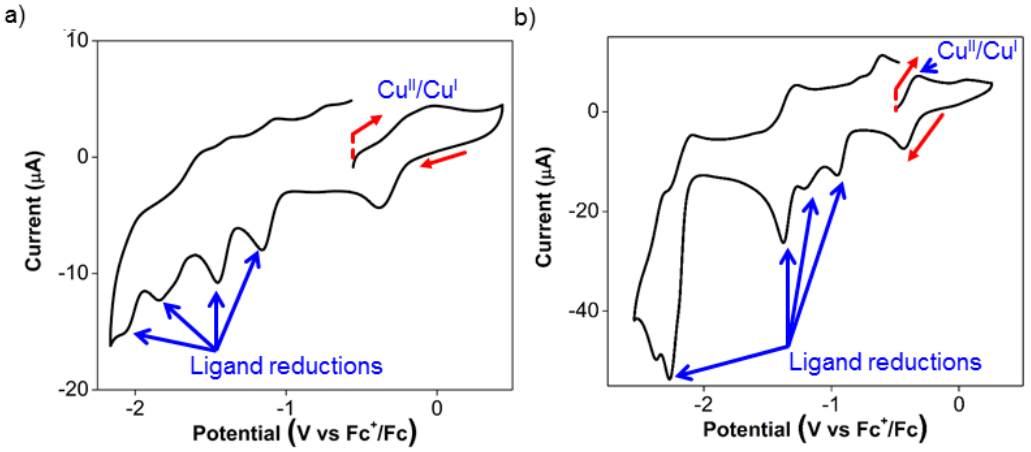

Figure 2.10 Cyclic voltammograms of (a) 1.0 mM of **2.3** and (b) 1.0 mM of **2.4** in **DMF/DMSO 1 : 1 (v : v)**, with 0.10 M ***n*-Bu$_4$NBAr$^{F}_4$** as the electrolyte, each at a scan rate of 100 mV s^{-1} with its scan direction and initial potential indicated by the red arrows and red vertical dashed line respectively. The blue arrows indicate the redox events of **2.3** and **2.4**. The data are reported relative to Fc^{+}/Fc.

During the cathodic scans of **2.3**, two quasi-reversible reduction waves at −1.16 and −1.46 V, and two irreversible reduction waves at −1.84, and −2.05 V were observed (Figure 2.11a). The electrochemical behavior in the cathodic scan in a smaller potential window (Figure 2.11b) is identical to that observed during the anodic scan, suggesting that the Cu^{II}/Cu^{I} redox process probably does not result in ligand dissociation or decomposition of the complex. Instead, the quasi-reversible behavior of the Cu^{II}/Cu^{I} process may be due to structural reorganization or reversible, transient solvent coordination by DMSO or DMF. The reduction potentials for **2.3** are slightly less negative than those observed in the ligand **2.1**. This could be due to the stabilization by distribution of electron density between both Ar-BIAN ligands within the complex. On

the other hand, the heteroleptic Cu^{I} Ar-BIAN phosphane complexes reported previously display only irreversible reduction processes, since the anionic charge is concentrated on only one ligand.[8b]

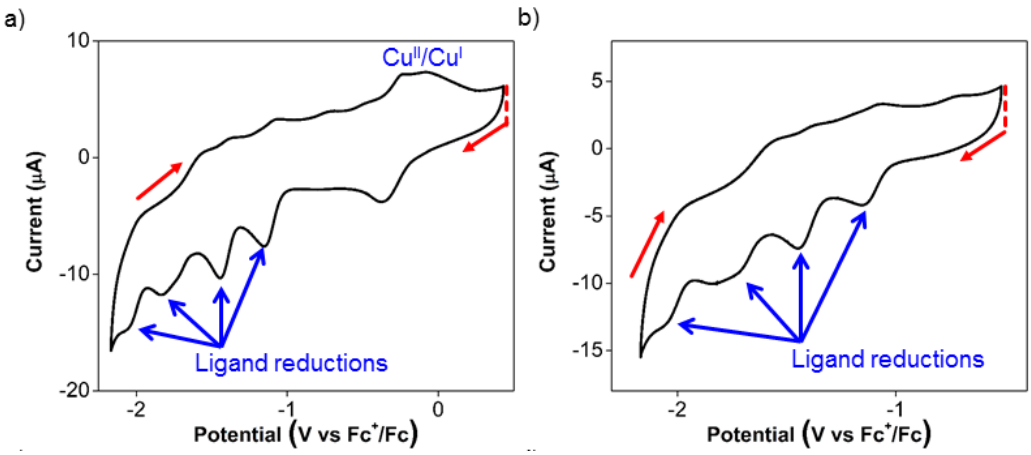

Figure 2.11 Cyclic voltammograms of 1.0 mM of **2.3** with 0.10 M ***n*-Bu$_4$NBAr$^F_4$** as the electrolyte in **DMF/DMSO 1:1 (v:v)**, each at a scan rate of 100 mV s^{-1}, within the potential windows of a) -2.1 to +0.5 V and b) -2.1 to -0.5 V respectively, relative to Fc^+/Fc. The red arrows indicate the scan directions, with red vertical lines indicating the initial potentials for each scan. The blue arrows indicate the ligand reductions of **2.3.**

Similarly, the cyclic voltammetry of **2.4** in DMF/DMSO is more complicated than that of its ligands while still displaying electrochemical behavior associated with ligand reduction processes. The anodic scan of **2.4** in DMF/DMSO (Figure 2.10b) exhibits a quasi-reversible oxidation at −0.33 V, which is significantly lower than that for **2.2** and other previously reported Cu^{I} Ar-BIAN homoleptic complexes.[8d] The Cu^{I}/Cu^{II} oxidation process could have become more accessible as a result of stabilization from solvent coordination on the Cu^{I} metal center, as facilitated by the rhombically distorted square planar geometry. It is especially noteworthy that the Cu^{I} complex did not suffer from ligand dissociation issues, since its purple color remained upon dissolution in DMF/DMSO. This is in contrast to the lability of **2.4** in ACN, which led to the dissociation of **2.2** in solution, as suggested by UV-visible spectroscopic measurements (*vide infra*).

The cathodic scan of **2.4** in DMF/DMSO yields three ligand-centered reduction waves (Figure 2.12a) at −1.37, −2.28 and −2.39 V as evident by their similarities in potentials to those observed during the reduction of **2.2**. Additional irreversible

reduction waves at −0.96 and −1.21 V are likely due to ligand reductive processes that involve stabilization by electron density distribution between Cu and the two ligands, similar to that found in **2.3**. As a result of the reduction process at −1.37 V, the oxidation peak current at −0.33 V appears to be diminished and a new anodic wave was observed at −0.02 V (Figure 2.12b). This could be due to dissociation of Cu upon excessive ligand reduction, which results in solvated Cu ions being subsequently oxidized.

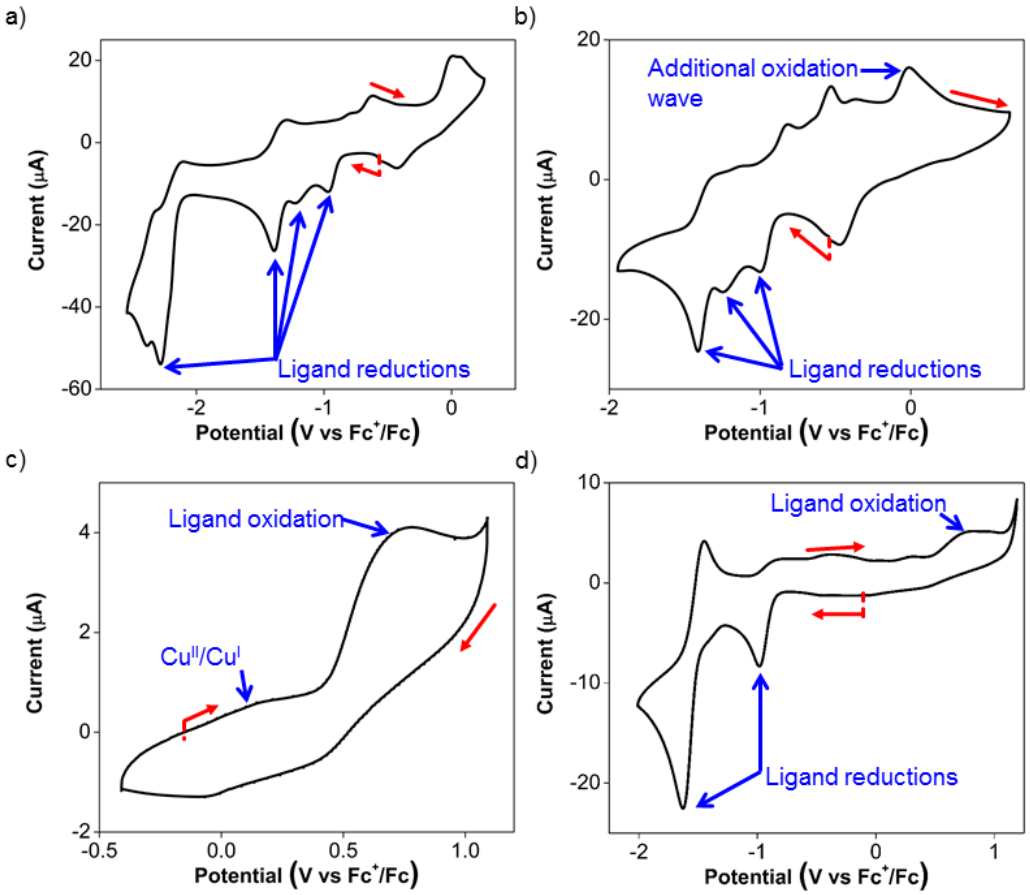

Figure 2.12 Cyclic voltammograms of 1.0 mM of **2.4** with 0.10 M ***n*-Bu$_4$NBAr$^F{}_4$** as the electrolyte in **DMSO/DMF 1:1 (v/v)** at a scan rate of 100 mV s^{-1}, within the potential windows of (a) -2.6 to +0.3 V, and (b) -2.0 to +0.7 V respectively. Additional cyclic voltammograms were performed similarly with 0.10 M ***n*-Bu$_4$NPF$_6$** as the electrolyte in **THF**, each at a scan rate of 100 mV s^{-1}, within the potential windows of (c) -0.40 to +1.1 V, and (d) -2.0 to +1.2 V respectively, relative to Fc$^+$/Fc. The red arrows indicate the scan directions, with red vertical lines indicating the initial potentials for each scan. The blue arrows indicate the ligand reductions of **2.4**.

On the other hand, the anodic scan of **2.4** in the relatively less coordinating THF exhibits two irreversible oxidations at +0.26 and +0.78 V (Figure 2.12c). The first oxidation likely corresponds to the Cu^{I}/Cu^{II} oxidation process, while the second oxidation can be assigned to the ligand oxidation, due to its comparable oxidation potential as **2.2** in THF. The cathodic scan of **2.4** in THF produces two quasi-reversible reduction waves at −0.98 and −1.63 V (Figure 2.12d), which is distinct from the electrochemical behavior in DMF/DMSO. In addition, the reduction wave at −1.63 V appears to be a two-electron reduction process, with double the current drawn compared to the reduction at −0.98 V. This solvent-dependence in the electrochemical behavior is likely due to the stronger coordination by DMF and DMSO than THF.

2.4.5 Spectroscopic Features of Cu^{I} Photosensitizers

UV-visible spectroscopy was employed to study the absorption characteristics of **2.1**–**2.4** and the results are summarized in Table 2.4. Relative reflectance measurements for the solids of **2.3** and **2.4** were recorded and the Kubelka-Munk function, *f(R)*, for each wavelength were computed from the relative reflectance, *R*, of the complexes using the following equation:

$$f(R) = \frac{(1-R)^2}{2R}$$

The spectra were treated with a Peakfit algorithm by using the second-derivative technique for locating the maxima between 450 nm and 1200 nm. The initial parameters were set up to fit three bands with the initial wavelengths set to 560, 620, and 720 nm before the amplitudes and widths of the Gaussian curves were optimized until a satisfactory fit was obtained (Figure 2.13c and 2.14). The Kubelka-Munk functions were then obtained from the amplitudes of the individual Gaussian curves fitted into the spectrum.

Table 2.4 UV-visible absorption properties and spectral fitting of the ligands and Cu^{I} complexes in MeOH[a] or DCM[b].

Compound	Band	Wavelength (nm)	ε ($M^{-1}cm^{-1}$)	ε ratio of bands I:II
2.1[a]	-	367	4190	
2.2[b]	-	364	3070	
2.3[a]	III	529	2970	0.59
	II	581	2930	
	I	686	1750	
2.4[b]	III	510	7730	0.57
	II	569	5340	
	I	700	3040	

The UV-visible spectra of ligands **2.1** and **2.2** (Figure 2.13a) extends to about 550 nm with a weak and broad band, and strong absorption in the UV region. Previous reports have assigned these UV-visible absorptions to π–π* transitions while the bands appearing in the visible spectrum could be attributed to iodide *n*–π* transitions or intraligand π–π* charge transfer (ILCT) from the aryl rings to the naphthyl backbone.[8d] The visible absorption peaks are similar to those observed for Ar-BIAN with meta substituents[8d] and suggest that their effect on the π system of the acenaphthene ring may not be too significant.

Similar ILCT transitions in the UV region are observed for **2.3** and **2.4**. In addition, they exhibit MLCT bands in the visible region (Figure 2.13b). The molar extinction coefficients (ε) of the bands in the UV regions of **2.3** and **2.4** are similar to their corresponding transitions in **2.1** and **2.2** respectively, as observed for Cu^{I} Ar-BIAN previously reported.[8d] A useful piece of information that can be obtained from the UV-visible spectroscopy, as established for Cu^{I} phen complexes,[6e, 20] is that the MLCT bands allows insight to the degree of distortion in the ground-state geometry from a tetrahedral coordination environment towards a flatter rhombically distorted square planar geometry. The three bands that are typically observed are labelled in Figure 2.13b. The D_{2d}-symmetry forbidden low-energy band extending beyond 700 nm is designated as band I. It corresponds to the lowest energy MLCT transition to the S_1 state.

The largest component of the spectrum comes from band II, which has been attributed to MLCT to the S_3 excited state. As a result, band I typically has low extinction coefficients and the ratios of band I to band II are lower for structures with

ideal tetrahedral Cu^{I} centers. Band III is an absorption between 500 and 600 nm, often overlapping with band II, which coincides with excitation to higher MLCT singlet states.[20] The intensity ratios of band I to band II for both complexes **2.3** and **2.4** in solution (Figure 2.13b and Table 2.3) are comparable to those reported previously.[8d] From the calculated intensity ratios, it is most probable that in the solution phase, **2.3** and **2.4** adopt slightly distorted tetrahedral geometries. However, the observed colors of **2.3** (dark blue) and **2.4** (dark green) are vastly different from their colors when dissolved (dark green for **2.3**; dark purple for **2.4**, *vide supra*). It is thus necessary to investigate the solid-state absorption characteristics through diffuse reflectance UV-visible spectroscopy (DRS). These measurements would also confirm the X-ray crystal structural features and provide information about the dyes when they are immobilized in DSSCs.

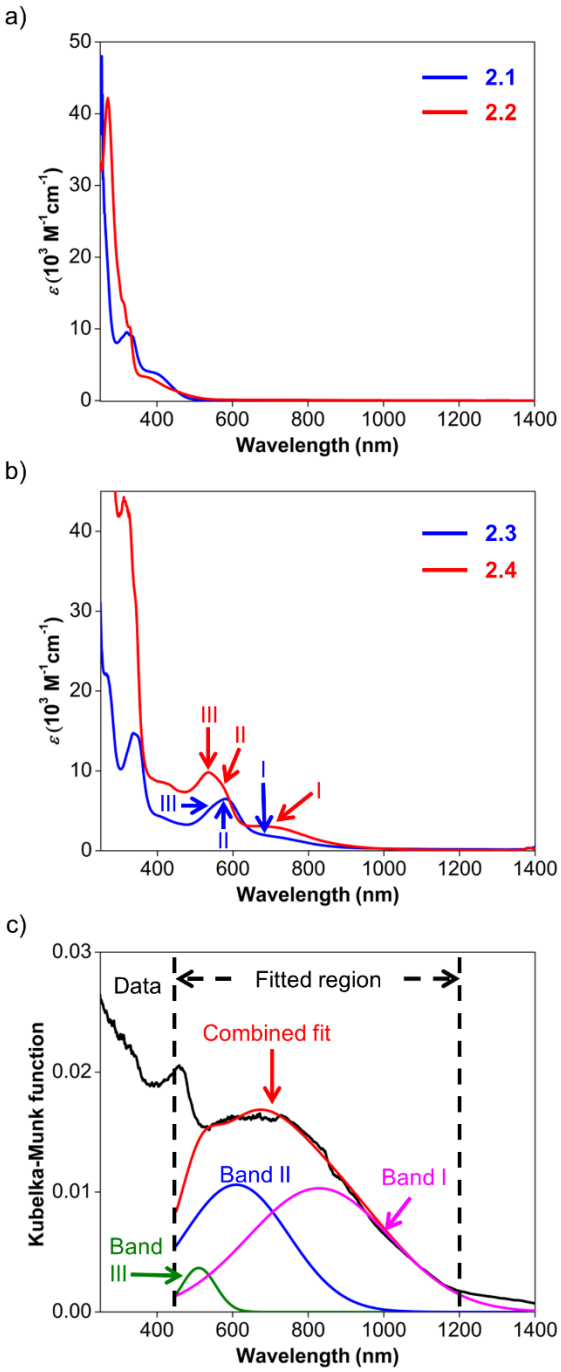

Figure 2.13 (a) UV-visible spectra of **2.1** (blue) and **2.2** (red) in MeOH and DCM respectively. (b) UV-visible spectra of **2.3** (blue) and **2.4** (red) in MeOH and DCM respectively. Roman numerals and arrows indicate the wavelength for the various fitted absorption bands of **2.3** (blue) and **2.4** (red). (c) Diffuse reflectance spectrum of **2.4** with fits for bands I (pink), II (blue), and III (green). The black line corresponds to the experimental data, while the red line is the superposition of the fitted bands.

The DRS spectra obtained (Figure 2.13c and 2.14) were distinct from the solution UV-visible spectra. In general, the MLCT bands from 500 nm and longer wavelengths bathochromically shift into the NIR region. For **2.3**, the two bands of the solution spectra split into the three distinct bands III, II and I (Figure 2.14a and 2.14b) at 493, 602, and 869 nm respectively, and a ratio of 1.2 was calculated for the fitted Kubelka–Munk functions. A broad band centered around 660 nm in the DRS spectrum of **2.4** was observed (Figure 2.14c). This broad absorption could be deconvoluted into the constituent bands III, II and I at 510 (green), 610 (blue), and 829 (pink) nm respectively, giving a ratio of 0.97 for the fitted Kubelka–Munk functions (Table 2.5). These results concur with the severely distorted geometry in the X-ray structures of **2.4** (Figure 2.6 and 2.7), which leads to absorptions in the NIR region.

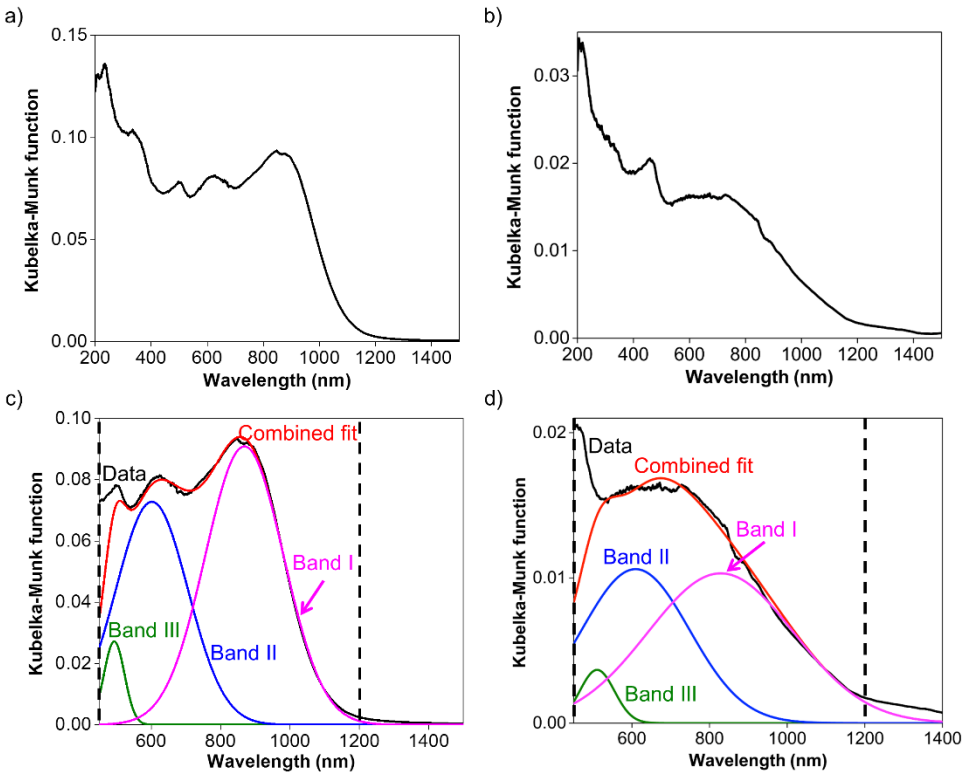

Figure 2.14 (a) Diffuse reflectance spectrum of (a) **2.3** and (b) **2.4**. Simulated spectrum obtained from fitting the MLCT bands I (pink), II (blue), and III (green) into the diffuse reflectance spectrum of (c) **2.3** and (d) **2.4** between the dashed lines. The black line represents the experimental data while the red line depicts the combined fit of all three bands.

Previously, ligand dissociation has been discussed as one of the possible degradation pathways for Cu^{I} complexes in coordinating solvents,[21] and similar observations were made with **2.4**. When it was dissolved in ACN, the UV-visible spectrum obtained did not present the MLCT components, whereas only the absorption bands due to the constituent ligand **2.2** were observed. Therefore, it is likely that **2.4** is labile in the presence of small, coordinating solvents (i.e. ACN), evident from the drastic change in solution color from dark purple (in DCM) to yellow (in ACN). In combination with the solvent dependence during the electrochemical measurements, the UV-visible data suggest that judicious selection of the solvents will be necessary for applications of **2.4**.

Table 2.5 Band maxima related to the excitations for the compounds measured using DRS and the ratio of the Kubelka-Munk functions, *K/S*.

Complex	Band	Wavelength (nm)	Fitted *f(R)*	*f*(R) ratio of *I:II*
2.3	III	493	0.0272	1.2
	II	602	0.0728	
	I	869	0.0909	
2.4	III	510	0.004	0.97
	II	610	0.0106	
	I	829	0.0103	

2.4.6 DFT Calculations

To further understand the unusual structural features of **2.4** and its observed UV-visible spectral behavior, a series of DFT calculations have been conducted by Dr. Xu, Dr Lu, and Prof Hirao. All calculations in this work were performed using the Gaussian 09 D01 package.[22] The M06 functional[23] was used in both DFT and TD-DFT calculations, and the def2 general basis sets were used (I and Cu: def2-TZVPPD; H, C, N and O: def2-TZVP).[24] Also, def2-ECP was used for iodine atoms. Ultrafine grids were adopted for the numerical integration in the DFT and TD-DFT calculations. The geometries of the cation complexes were optimized from crystal structures and solvent effects were included using the CPCM model.[25] Although two mixtures of solvents were used in the experiments, in the calculations, only two pure solvents, toluene and DCM, were considered for simplicity. Using the optimized geometries, two additional

theoretical analyses were performed to evaluate non-covalent interactions within the molecule. First, non-covalent interaction (NCI) analysis was conducted using the NCIPLOT-3.0 software package with the promolecular approximation.[26] Second, an Atoms in Molecules (AIM) analysis was performed using AIMAll (Version 13.05.06).[27]

Screening of various DFT methods and basis sets were performed to find the best agreement, for both the Cu–N bond lengths and the dihedral angles between the two chelated rings, among the optimized and solid-state structures (Table 2.6). Some of the frontier orbitals for the structure of **2.4** optimized in toluene as the solvent are illustrated in Figure 2.15. As anticipated, the HOMO (Figure 2.15a) appears to consist predominantly of a d-orbital from the Cu^{I} center, with spin density distributed over the iminoaryl parts of ligand **2.2**, and almost no contribution from the acenaphthene fragment. In contrast, the LUMO (Figure 2.15b) and LUMO+1 (Figure 2.15c) are mainly comprised of orbital components from the acenaphthene fragments. In fact, inter-ligand lobes connecting both the imino moieties of the ligands can be observed in the LUMO, alluding to ligand- to-ligand charge transfer characteristics in **2.4**. An interesting identification is a low energy orbital (HOMO−12) consisting of overlapping lobes between two opposite iodide p-orbitals and a copper d-orbital (Figure 2.15d), despite the long copper–iodide distances (3.904(2) and 4.051(2) Å for crystals grown from THF/toluene; and 3.481(2) and 4.273(2) Å for crystals grown from DCM/Et_2O), as determined from the crystal structures.

Table 2.6 Comparison of selected bond lengths [Å] and angles [°] for **2.4** from the geometry optimizations in the different solvents with the experimental values.

Internal coordinates	Cation of **2.4** in toluene	Experimental data	Cation of **2.4** in DCM	Experimental data
Cu1-N1	1.957	1.94	1.950	1.907
Cu1-N2	2.549	2.46	2.542	2.46
Cu1-N3	1.957	1.93	1.944	1.892
Cu1-N4	2.552	2.52	2.593	2.645
I1-I2	4.904	4.354	4.927	4.984
I2-I3	4.321	4.276	4.367	4.857
I3-I4	4.903	4.621	5.236	5.144
I1-I4	4.322	4.309	4.366	4.524
N1-Cu-N2	76.5	76.5	75.1	76.1
N3-Cu-N4	75.8	75.8	74.4	74.7
Dihedral angle	23.9	32.0	23.6	21.2

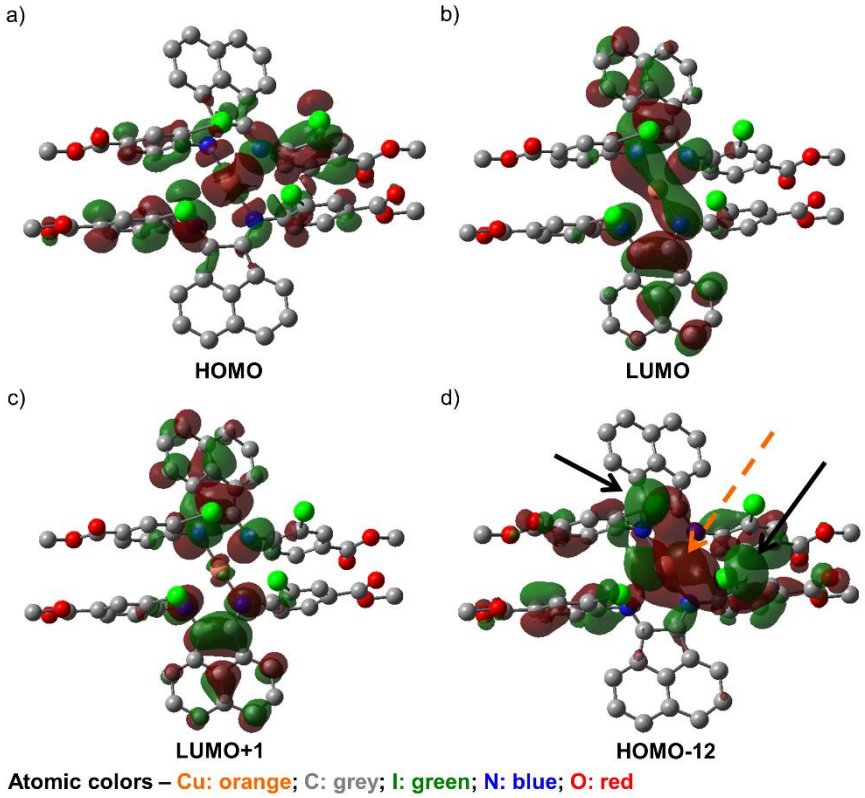

Figure 2.15 (a) HOMO, (b) LUMO, and (c) LUMO+1 of geometry-optimized **2.4** in toluene, set at isovalues of 0.02, and (d) HOMO-12 set at an isovalue of 0.01. The orange arrows in (d) indicate the d-orbital lobe contributions from Cu^{I}, while the black arrows point to the p-orbital contributions from two of the iodides in **2.2**.

It is hypothesized that these weak copper–iodide interactions, some iodide–iodide interactions, and the π-π stacking between the iminoaryl motifs in Figure 2.15d are responsible for the unusual geometrical arrangement of the ligands surrounding the Cu^{I} center. Therefore, further analysis by the Atoms-in-Molecules (AIM) approach[27] was performed to understand the non-covalent interactions within the molecules. As shown in Figure 2.16, the AIM analysis yielded several bond critical points (BCPs) between the aromatic rings of the ligands, indicative of the presence of π–π stacking effects.

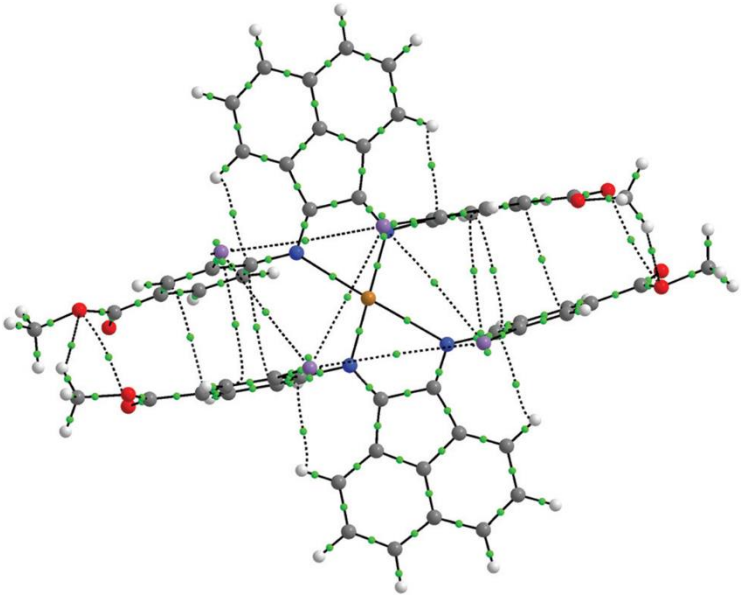

Figure 2.16 AIM plot for **2.4** in toluene, with the light-green points being BCPs.

Furthermore, BCPs are also seen between the iodine atoms, which imply the presence of halogen–halogen interactions, even though the arrangement of iodine atoms does not appear to strictly fulfil the geometric criteria set by Desiraju.[28] These combined non-covalent effects may therefore facilitate the establishment of the unique coordination sphere around the metal center observed in this compound. An analysis was performed using the non-covalent interactions (NCI) index further implicating the involvement of these non-covalent interactions (Figure 2.16).[26]

Additional TD-DFT calculations of **2.4** conducted to compare with the obtained UV-visible data will be excluded since they are beyond the scope of this report.

2.5 Conclusion

In this chapter, the development of two Cu^{I} dyes bearing new Ar-BIAN ligands that can be expediently synthesized from affordable commercial reagents were discussed. For complex **2.4**, the solid-state crystal structures derived from single crystal X-ray diffraction experiments using crystals grown from two different solvent combinations both displayed remarkable rhombically distorted square planar geometries around the Cu^{I} center. This unique coordination sphere around the Cu^{I} nucleus is manifest in the broad, panchromatic light absorption extending to the NIR region, as determined by DRS measurements. DFT and AIM calculations suggest that weak, non-covalent interactions between the aromatic rings and among the iodides may be responsible for

the rare coordination geometry and photophysical features. The following chapter will discuss the incorporation of **2.3** and **2.4** into DSSCs.

2.6 Experimental Section

2.6.1 General Considerations

The copper (Cu) complexes used in this study were synthesized in a glovebox under a N_2 atmosphere. Deuterated solvents were purchased from Cambridge Isotope Laboratories and were distilled prior to use. The other chemicals were obtained from Sigma-Aldrich and were used as received. Tetrabutylammonium tetrakis[3,5-bis(trifluoromethyl)phenyl]borate[29] (*n*-$Bu_4NBAr^F_4$), bromoacenaphthylene-1,2-dione,[30] methyl 4-amino-3-iodobenzoate,[31] and sodium 4-aminobenzenesulfonate[14] were synthesized according to previously published procedures. The ^1H and ^{13}C NMR spectra were recorded at room temperature on a Bruker AVANCE 400 MHz spectrometer. The chemical shifts (δ reported in ppm) are referenced to the residual solvent signal(s). For the X-ray crystal structures, dihedral angles between the planes formed by the chelating rings around the Cu^I center were determined by the Diamond 3.2 software, whereas centroid distances between aryl rings were obtained from the Mercury 3.5 software.

CV experiments were conducted using a Biologic SP-300 potentiostat with 1.0 mM solutions of each sample and 0.10 M of either *n*-$Bu_4NBAr^F_4$ or tetrabutylammonium hexafluorophosphate (*n*-Bu_4NPF_6) as the electrolyte. The measurements of all four compounds **2.1** – **2.4** were conducted in DMF/DMSO 1:1 (v/v) for comparison among them, while additional CVs were run in THF at a scan rate of 100 mV s^{-1} in a glovebox. A standard three-electrode electrochemical cell was used with a glassy carbon working electrode (3 mm in diameter from BAS), a Pt wire as the counter electrode, and another Pt wire as the pseudoreference electrode. The potentials were calibrated by addition of ferrocene as an internal reference (0 V) after the CV measurements on the compound have been conducted to avoid obscuring signals from our samples. Before each experiment, the working electrode (glassy carbon) was polished using a polishing pad infused with a 0.05 μm alumina suspension, followed by sonication in DI water for 10 min, washed with methanol and acetone, before drying in air.

UV-visible spectroscopic measurements were performed using a Shimadzu UV-3600 UV-Vis-NIR Spectrophotometer. Relative reflectance measurements were recorded using a Shimadzu UV-3600 UV-Vis-NIR Spectrophotometer equipped with

an ISR-3100 integrating sphere attachment and barium sulfate was used as the reference standard. The samples were mixed and ground with barium sulfate in the glovebox prior to measurement.

2.6.2 Synthesis of Ligands

Na(Ar^{SO3}-Br-BIAN) (2.1). The ligand **Na(Ar^{SO3}-Br-BIAN)** (**2.1**) was synthesized according to a modified literature procedure.[14] To a 2 mL methanolic suspension of sodium 4-aminobenzenesulfonate (248 mg, 1.27 mmol) and 5-bromoacenaphthylene-1,2-dione[30] (81 mg, 0.31 mmol), five drops of formic acid were added and the mixture was heated at 60 ºC for 20 hours. The resulting orange mixture was then filtered and washed with 3 x 5 mL of cold methanol to remove unreacted aniline and the partially condensed monoimine. The crude product was then recrystallized using DMF/Et_2O and washed with THF to give the orange-colored **2.1** (86 mg, 0.14 mol, 42% yield). ^{1}H NMR (400 MHz, DMSO-d_6): δ = 6.80 (d, J = 7.6 Hz, 1 H), 6.94 (d, J = 7.2 Hz, 1 H), 7.04 (d, J = 7.6 Hz, 4 H), 7.73 (m, 5 H), 7.97 (d, J = 8.0 Hz, 1 H), 8.12 (d, J = 8.4 Hz, 1 H) ppm. ^{13}C NMR (101 MHz, DMSO-d_6): δ = 117.11, 124.16, 124.30, 124.48, 127.67, 128.42, 129.03, 130.03, 130.72, 132.01, 142.00, 145.41, 151.36, 151.46, 159.26, 159.62 ppm. HRMS (ESI−, m/z) calculated for $C_{24}H_{13}BrN_2NaO_6S_2$ $[M - Na]^-$ 590.9296, found 590.9289.

Ar^{I,COOMe}-BIAN (2.2). The ligand **Ar^{I,COOMe}-BIAN** (**2.2**) was synthesized according to a modified literature procedure.[15] Methyl 4-amino-3-iodobenzoate[31] (294 mg, 1.09 mmol) and 1,4-diazabicyclo[2.2.2]octane (492 mg, 4.38 mmol) was dissolved in 2 mL of chlorobenzene before a 1.0 M toluene solution of $TiCl_4$ (1.2 mL, 1.2 mmol) was added under N_2. The mixture was heated for an hour at 100 ºC before acenapthylene-1,2-dione (100 mg, 0.548 mmol) was added and heated for another 16 hours. The reaction mixture was cooled to room temperature and 20 mL of DCM was added before the suspension was filtered. The filtrate was then dried by rotary evaporation and the remaining solid was recrystallized using DCM/methanol to afford an orange crystalline product (261 mg, 0.372 mmol, 68 % yield). ^{1}H NMR (400 MHz, $CDCl_3$): (*E*,*E*)-isomer only: δ = 3.97 (s, 6 H), 6.87 (d, *J* = 6.8 Hz, 2 H), 7.16 (d, *J* = 8.4 Hz, 2 H), 7.45 (t, *J* = 7.6 Hz, 2 H), 7.99 (d, *J* = 8.0 Hz, 2 H), 8.15 (d, *J* = 8.0 Hz, 2 H), 8.68 (s, 2 H) ppm. ^{13}C NMR (101 MHz, $CDCl_3$): δ = 52.47, 86.37, 117.79, 124.12, 127.80, 128.36 (2 C),

130.09, 131.00, 131.48, 141.32, 141.77, 157.15, 161.71, 165.67 ppm. HRMS (ESI+, *m/z*) calculated for $C_{28}H_{19}N_2O_4I_2$ $[M+H]^+$ 700.9436, found 700.9434. Elemental analyses for $C_{28}H_{18}N_2O_4I_2$ calculated: C, 48.03; H, 2.59; N, 4.00%; found: C, 48.02; H, 2.59; N, 4.01%.

2.6.3 Synthesis of Cu^I Complexes

Na_3[(Ar^{SO3}-Br-BIAN)$_2$Cu] (2.3). To a 2 mL DMSO solution of **2.1** (84 mg, 0.14 mmol), anhydrous Cu^I chloride (8.0 mg, 0.059 mmol) was added. The reaction mixture was stirred for 12 h before it was filtered to remove undissolved matter. The filtrate was dried *in vacuo* and the product was recrystallized in DMSO/ACN to afford a dark-blue powder (66 mg, 0.041 mmol, 69% yield). Due to the poor solubility of **2.3**, sufficiently high concentrations of the complex could not be dissolved for all the chemicals shifts in the ^{13}C NMR spectrum to be located. ^1H NMR (400 MHz, methanol-d_4): δ = 7.15 (d, J = 7.5 Hz, 2 H), 7.34 (m, br, 10 H), 7.68 (dd, J = 8.0, 8.0 Hz, 2 H), 7.86 (d, J = 8.5 Hz, 2 H), 8.04 (d, J = 6.2 Hz, 8 H), 8.31 (d, J = 8.9 Hz, 2 H) ppm. HRMS (ESI-, *m/z*) Calculated for $C_{48}H_{26}N_4O_{12}Na_2S_4{}^{63}Cu^{81}Br_2$ $[M-Na]^-$ 1248.7847, $C_{48}H_{26}N_4O_{12}Na_2S_4{}^{65}Cu^{79}Br^{81}Br$ $[M-Na]^-$ 1248.7850, found 1248.7845. Elemental analyses for octa-hydrate $C_{48}H_{42}Br_2N_4Na_3O_{20}S_4Cu$ calculated: C, 40.73; H, 2.99; N, 3.96; S, 9.06%; found: C, 40.38; H, 3.30; N, 3.78; S, 9.49%.

[($Ar^{I,COOMe}$-BIAN)$_2$Cu]PF_6 (**2.4**). A 2 mL THF solution of $Cu(CH_3CN)_4PF_6$ (13 mg, 0.035 mmol) was added dropwise to a separate 2 mL THF solution of **2.2** (50 mg, 0.071 mmol). The mixture was stirred for 8 h and dark-green crystalline material formed. Et_2O was added and more crystalline material formed on standing. The crystals were filtered and redissolved in DCM before drying to afford a dark green powder (50 mg, 0.031 mmol, 89% yield). ^1H NMR (400 MHz, $CDCl_3$): δ = 4.02 (s, 12 H), 6.77 (s, br, 4 H), 7.31 (s, br, 4 H), 7.49 (t, J = 7.6 Hz, 4 H), 8.13 (m, 8 H), 8.63 (s, 4 H) ppm. ^{13}C NMR (101 MHz, $CDCl_3$): δ = 52.75, 89.37, 121.22, 125.38, 126.09, 129.03, 130.28, 131.28, 131.48, 132.30, 141.43, 142.93 152.81, 164.89, 166.1 ppm. HRMS (ESI+, *m/z*) calculated for $C_{56}H_{36}I_4N_4O_8Cu$ $[M-PF_6]^+$ 1462.8008, found 1462.7936. Elemental analyses for $C_{56}H_{36}I_4N_4O_8CuPF_6$ calculated: C, 41.80%; H, 2.26 N, 3.48%; found: C, 41.58%; H, 2.53%; N, 3.36%.

2.7 References

(1) Kee, J. W.; Ng, Y. Y.; Kulkarni, S. A.; Muduli, S. K.; Xu, K.; Ganguly, R.; Lu, Y.; Hirao, H.; Soo, H. S., *Inorg. Chem. Front.* **2016**, *3*, 651-662.

(2) (a) Prier, C. K.; Rankic, D. A.; MacMillan, D. W., *Chem. Rev.* **2013**, *113*, 5322-5363; (b) Narayanam, J. M. R.; Stephenson, C. R. J., *Chem. Soc. Rev.* **2011**, *40*, 102-113; (c) Romero, N. A.; Nicewicz, D. A., *Chem. Rev.* **2016**, *116*, 10075-10166.

(3) (a) Bagal, D. B.; Kachkovskyi, G.; Knorn, M.; Rawner, T.; Bhanage, B. M.; Reiser, O., *Angew. Chem. Int. Ed.* **2015**, *54*, 6999-7002; (b) Beatty, J. W.; Douglas, J. J.; Cole, K. P.; Stephenson, C. R., *Nat. Commun.* **2015**, *6*, 7919; (c) Fumagalli, G.; Rabet, P. T.; Boyd, S.; Greaney, M. F., *Angew. Chem. Int. Ed.* **2015**, *54*, 11481-11484; (d) Hernandez-Perez, A. C.; Collins, S. K., *Angew. Chem. Int. Ed.* **2013**, *52*, 12696-12700; (e) Nguyen, J. D.; Matsuura, B. S.; Stephenson, C. R., *J. Am. Chem. Soc.* **2014**, *136*, 1218-1221; (f) Nicewicz, D. A.; MacMillan, D. W. C., *Science* **2008**, *322*, 77-80; (g) Schultz, D. M.; Yoon, T. P., *Science* **2014**, *343*, 985; (h) Tang, X. J.; Dolbier, W. R., Jr., *Angew. Chem. Int. Ed.* **2015**, *54*, 4246-4249; (i) Xuan, J.; Xiao, W. J., *Angew. Chem. Int. Ed.* **2012**, *51*, 6828-6838; (j) Yoon, T. P.; Ischay, M. A.; Du, J. N., *Nat. Chem.* **2010**, *2*, 527-532; (k) Zuo, Z. W.; Ahneman, D. T.; Chu, L. L.; Terrett, J. A.; Doyle, A. G.; MacMillan, D. W. C., *Science* **2014**, *345*, 437-440; (l) Griffin, J. D.; Zeller, M. A.; Nicewicz, D. A., *J. Am. Chem. Soc.* **2015**, *137*, 11340-11348; (m) Romero, N. A.; Margrey, K. A.; Tay, N. E.; Nicewicz, D. A., *Science* **2015**, *349*, 1326-1330.

(4) (a) Yin, J.-F.; Velayudham, M.; Bhattacharya, D.; Lin, H.-C.; Lu, K.-L., *Coord. Chem. Rev.* **2012**, *256*, 3008-3035; (b) Henwood, A. F.; Zysman-Colman, E., *Chem. Commun.* **2017**, *53*, 807-826.

(5) (a) Gratzel, M., *Acc. Chem. Res.* **2009**, *42*, 1788-1798; (b) Brown, D. G.; Sanguantrakun, N.; Schulze, B.; Schubert, U. S.; Berlinguette, C. P., *J. Am. Chem. Soc.* **2012**, *134*, 12354-12357; (c) Robson, K. C. D.; Hu, K.; Meyer, G. J.; Berlinguette, C. P., *J. Am. Chem. Soc.* **2013**, *135*, 1961-1971; (d) Hu, K.; Robson, K. C. D.; Johansson, P. G.; Berlinguette, C. P.; Meyer, G. J., *J. Am. Chem. Soc.* **2012**, *134*, 8352-8355.

(6) (a) Harlang, T. C.; Liu, Y.; Gordivska, O.; Fredin, L. A.; Ponseca, C. S., Jr.; Huang, P.; Chabera, P.; Kjaer, K. S.; Mateos, H.; Uhlig, J.; Lomoth, R.; Wallenberg, R.; Styring, S.; Persson, P.; Sundstrom, V.; Warnmark, K., *Nat. Chem.* **2015**, *7*, 883-889; (b) Bozic-Weber, B.; Chaurin, V.; Constable, E. C.; Housecroft, C. E.; Meuwly, M.; Neuburger, M.; Rudd, J. A.; Schonhofer, E.; Siegfried, L., *Dalton Trans.* **2012**, *41*, 14157-14169; (c) Bozic-Weber, B.; Constable, E. C.; Furer, S. O.; Housecroft, C. E.; Troxler, L. J.;

Zampese, J. A., *Chem. Commun.* **2013**, *49*, 7222-7224; (d) Chen, L. X.; Shaw, G. B.; Novozhilova, I.; Liu, T.; Jennings, G.; Attenkofer, K.; Meyer, G. J.; Coppens, P., *J. Am. Chem. Soc.* **2003**, *125*, 7022-7034; (e) Ichinaga, A. K.; Kirchhoff, J. R.; McMillin, D. R.; Dietrich-Buchecker, C. O.; Marnot, P. A.; Sauvage, J. P., *Inorg. Chem.* **1987**, *26*, 4290-4292; (f) Iwamura, M.; Takeuchi, S.; Tahara, T., *Acc. Chem. Res.* **2015**, *48*, 782-791; (g) Juban, E. A.; Smeigh, A. L.; Monat, J. E.; McCusker, J. K., *Coord. Chem. Rev.* **2006**, *250*, 1783-1791; (h) Lu, X. Q.; Wei, S. X.; Wu, C. M. L.; Li, S. R.; Guo, W. Y., *J. Phys. Chem. C* **2011**, *115*, 3753-3761; (i) Papanikolaou, P. A.; Tkachenko, N. V., *Phys. Chem. Chem. Phys.* **2013**, *15*, 13128-13136.

(7) Armaroli, N., *Chem. Soc. Rev.* **2001**, *30*, 113-124.

(8) (a) Gasperini, M.; Ragaini, F.; Cenini, S., *Organometallics* **2002**, *21*, 2950-2957; (b) Gasperini, M.; Ragaini, F.; Gazzola, E.; Caselli, A.; Macchi, P., *Dalton Trans.* **2004**, 3376-3382; (c) Hasan, K.; Zysman-Colman, E., *J. Phys. Org. Chem.* **2013**, *26*, 274-279; (d) Papanikolaou, P.; Akrivos, P. D.; Czapik, A.; Wicher, B.; Gdaniec, M.; Tkachenko, N., *Eur. J. Inorg. Chem.* **2013**, 2418-2431; (e) Hasan, K.; Wang, J.; Pal, A. K.; Hierlinger, C.; Guerchais, V.; Sen Soo, H.; Garcia, F.; Zysman-Colman, E., *Sci. Rep.* **2017**, *7*, 15520; (f) Wang, J.; Ganguly, R.; Yongxin, L.; Diaz, J.; Soo, H. S.; Garcia, F., *Inorg. Chem.* **2017**, *56*, 7811-7820; (g) Wang, J.; Ganguly, R.; Yongxin, L.; Diaz, J.; Soo, H. S.; Garcia, F., *Dalton Trans.* **2016**, *45*, 7941-7946.

(9) (a) Fedushkin, I. L.; Chudakova, V. A.; Skatova, A. A.; Khvoinova, N. M.; Kurskii, Y. A.; Glukhova, T. A.; Fukin, G. K.; Dechert, S.; Hummert, M.; Schumann, H., *Z. Anorg. Allg. Chem.* **2004**, *630*, 501-507; (b) Fedushkin, I. L.; Skatova, A. A.; Chudakova, V. A.; Fukin, G. K., *Angew. Chem. Int. Ed.* **2003**, *42*, 3294-3298; (c) Fedushkin, I. L.; Skatova, A. A.; Cherkasov, V. K.; Chudakova, V. A.; Dechert, S.; Hummert, M.; Schumann, H., *Chem. Eur. J.* **2003**, *9*, 5778-5783.

(10) (a) Li, L. D.; Lopes, P. S.; Figueira, C. A.; Gomes, C. S. B.; Duarte, M. T.; Rosa, V.; Fliedel, C.; Aviles, T.; Gomes, P. T., *Eur. J. Inorg. Chem.* **2013**, 1404-1417; (b) Li, L.; Lopes, P. S.; Rosa, V.; Figueira, C. A.; Lemos, M. A. N. D. A.; Duarte, M. T.; Aviles, T.; Gomes, P. T., *Dalton Trans.* **2012**, *41*, 5144-5154; (c) Chan, W. K.; Hui, C. S.; Man, K. Y. K.; Cheng, K. W.; Wong, H. L.; Zhu, N. Y.; Djurisic, A. B., *Coord. Chem. Rev.* **2005**, *249*, 1351-1359.

(11) (a) Kern, T.; Monkowius, U.; Zabel, M.; Knor, G., *Eur. J. Inorg. Chem.* **2010**, 4148-4156; (b) Rosa, V.; Santos, C. I. M.; Welter, R.; Aullon, G.; Lodeiro, C.; Aviles, T., *Inorg. Chem.* **2010**, *49*, 8699-8708.

(12) Huang, J.; Buyukcakir, O.; Mara, M. W.; Coskun, A.; Dimitrijevic, N. M.; Barin, G.; Kokhan, O.; Stickrath, A. B.; Ruppert, R.; Tiede, D. M.; Stoddart, J. F.; Sauvage, J.-P.; Chen, L. X., *Angew. Chem. Int. Ed.* **2012**, *51*, 12711-12715.

(13) He, J.; Hagfeldt, A.; Lindquist, S.-E.; Grennberg, H.; Korodi, F.; Sun, L.; Åkermark, B., *Langmuir* **2001**, *17*, 2743-2747.

(14) Zhou, J.; Li, X.; Sun, H., *Can. J. Chem.* **2008**, *86*, 782-790.

(15) Li, L.; Jeon, M.; Kim, S. Y., *J. Mol. Catal. A: Chem.* **2009**, *303*, 110-116.

(16) Rosa, V.; Aviles, T.; Aullon, G.; Covelo, B.; Lodeiro, C., *Inorg. Chem.* **2008**, *47*, 7734-7744.

(17) Doherty, S.; Knight, J. G.; Smyth, C. H.; Sore, N. T.; Rath, R. K.; McFarlane, W.; Harrington, R. W.; Clegg, W., *Organometallics* **2006**, *25*, 4341-4350.

(18) (a) Madhu, V.; Diskin-Posner, Y.; Neumann, R., *Eur. J. Inorg. Chem.* **2011**, *2011*, 1792-1796; (b) Drew, M. G. B.; Harding, C. J.; Howarth, O. W.; Lu, Q.; Marrs, D. J.; Morgan, G. G.; McKee, V.; Nelson, J., *J. Chem. Soc., Dalton Trans.* **1996**, 3021; (c) Stollenz, M.; John, M.; Gehring, H.; Dechert, S.; Grosse, C.; Meyer, F., *Inorg. Chem.* **2009**, *48*, 10049-10059; (d) Spek, A. L.; Duisenberg, A. J. M.; van Stein, G. C.; van Koten, G., *Acta Crystallogr. Sect. C: Cryst. Struct. Commun.* **1985**, *41*, 374-377; (e) Monkowius, U.; Svartsov, Y. N.; Fischer, T.; Zabel, M.; Yersin, H., *Inorg. Chem. Commun.* **2007**, *10*, 1473-1477.

(19) Pause, L.; Robert, M.; Savéant, J.-M., *J. Am. Chem. Soc.* **1999**, *121*, 7158-7159.

(20) Armaroli, N.; Accorsi, G.; Cardinali, F.; Listorti, A., Photochemistry and Photophysics of Coordination Compounds: Copper. In *Photochemistry and Photophysics of Coordination Compounds I*, Balzani, V.; Campagna, S., Eds. Springer Berlin Heidelberg: 2007; Vol. 280, pp 69-115.

(21) Gandhi, B. A.; Green, O.; Burstyn, J. N., *Inorg. Chem.* **2007**, *46*, 3816-3825.

(22) M. J. Frisch, *e. a.*, Gaussian 09, Revision D.01, Gaussian, Inc., Wallingford, CT, USA, 2009

(23) Zhao, Y.; Schultz, N. E.; Truhlar, D. G., *J. Chem. Theory Comput.* **2006**, *2*, 364-382.

(24) (a) Weigend, F.; Ahlrichs, R., *Phys. Chem. Chem. Phys.* **2005**, *7*, 3297-3305; (b) Metz, B.; Stoll, H.; Dolg, M., *The Journal of Chemical Physics* **2000**, *113*, 2563-2569.

(25) (a) Barone, V.; Cossi, M., *The Journal of Physical Chemistry A* **1998**, *102*, 1995-2001; (b) Cossi, M.; Rega, N.; Scalmani, G.; Barone, V., *J. Comput. Chem.* **2003**, *24*, 669-681.

(26) (a) Contreras-Garcia, J.; Johnson, E. R.; Keinan, S.; Chaudret, R.; Piquemal, J. P.; Beratan, D. N.; Yang, W., *J. Chem. Theory Comput.* **2011**, *7*, 625-632; (b) Johnson, E. R.; Keinan, S.; Mori-Sanchez, P.; Contreras-Garcia, J.; Cohen, A. J.; Yang, W., *J. Am. Chem. Soc.* **2010**, *132*, 6498-6506.

(27) (a) Bader, R. F. W., *Chem. Rev.* **1991**, *91*, 893-928; (b) Keith, T. A., *AIMAll (Version 13.05.06)*, TK Gristmill Software, Overland Park, KS, USA, 2013 (aim.tkgristmill.com)

(28) Mukherjee, A.; Tothadi, S.; Desiraju, G. R., *Acc. Chem. Res.* **2014**, *47*, 2514-2524.

(29) (a) Fierke, M. A.; Olson, E. J.; Buhlmann, P.; Stein, A., *ACS Appl. Mater. Interfaces* **2012**, *4*, 4731-4739; (b) Yakelis, N. A.; Bergman, R. G., *Organometallics* **2005**, *24*, 3579-3581.

(30) Grant, C. D.; Kang, S. O.; Hay, B. P., *J. Org. Chem.* **2013**, *78*, 7735-7740.

(31) Patel, B.; Saviolaki, G.; Ayats, C.; Garcia, M. A. E.; Kapadia, T.; Hilton, S. T., *RSC Adv.* **2014**, *4*, 18930-18932.

Chapter 3

Incorporation of Bis(arylimino)acenaphthene (BIAN) Copper Complexes as Visible Light Harvesters for Potential Photovoltaic Applications

3.1 Foreword

As mentioned previously in section 2.1, Chapter 3 is based on the work published in *Inorganic Chemistry Frontiers* (*Inorg. Chem. Front.*, **2016**, *3*, 651) and reproduced by permission of The Royal Society of Chemistry.[1] The numbering scheme used in this chapter is the numbering system from Chapter 2. The Cu^{I} complexes synthesized and discussed in Chapter 2 were utilized as photosensitizers in solar devices. The results obtained from the testing of the devices will be presented in this chapter. The fabrication of the devices and the measurements required the expertise of Dr. Kulkarni and Dr. Muduli.

3.2 Introduction

3.2.1 Brief History of Dye-Sensitized Solar Cells (DSSCs)

With the aim of harnessing solar energy more efficiently, many technologies are already in place and continuously developed upon so as to improve their capabilities in utilizing the energy provided by the Sun. Some of them include photovoltaic (PV) cells, solar thermal technology, and passive solar technology.[2] Although this list is non-exhaustive, it gives a glimpse of the more common solar technology used.

Traditional solar PV cells are made of crystalline silicone. Over the years, there has been much improvements made to these traditional PV cells and also new innovative technologies to further decrease the cost and ease of production.[3] One of the most promising alternatives is the DSSC due to its ability to perform better than PV cells when the sunlight intensity is low.[4] The first remarkable breakthrough in the development of DSSC was by O'Regan and Grätzel in 1991 when they achieved more than 80% efficiency in converting incident photons to electrical current.[5] Since this seminal discovery, there have been industrial interest in improving its design and commercializing it. Some advantages of DSSCs include the reasonable efficiency in solar energy conversion, low production cost and the possibility of upscale production.[6]

3.2.2 Principle of Operation

DSSC is a semiconductor photovoltaic cell which can absorb sunlight and convert it into useful electrical energy.[6b, 7] As illustrated in Figure 3.1, in the DSSC, there is a transparent photoanode deposited with a thin mesoporous semiconductor (usually TiO_2)

layer that is treated with a conductive substrate. On which, a monolayer of molecular dye (typically Ru-based, denoted as PS in Figure 3.1) was bonded covalently to the surface. Upon visible light irradiation, the absorbed PS gets photoexcited to become PS*. This results in the injection of an electron into the conduction band of the semiconductor while PS* is oxidized to become PS^+. The injected electron is driven through the external circuit to arrive at the counter electrode, generating an electric current. The electron reduces the redox mediator (typically I_3^-/I^- redox couple) to regenerate the PS by the reduction of PS^+ thus completing the circuit. [6b, 7]

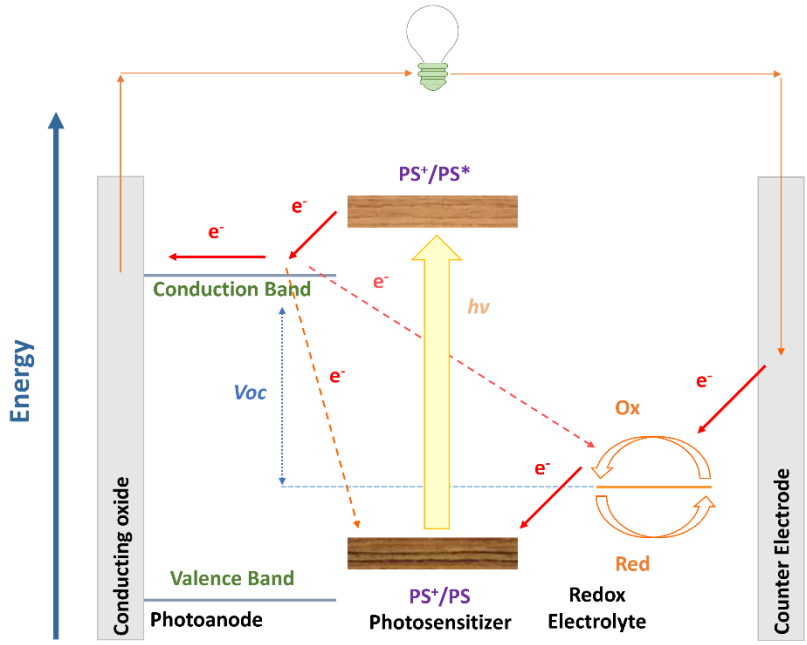

Figure 3.1 Operating principle and energy level diagram of a DSSC.[6b]

3.2.3 Recent Advances

In order to optimize the efficiency of the DSSC, a judicious selection of the substrates and materials making up the different components is needed to fully exploit the maximum potential of the DSSC. Over the past two decades, the continual improvements made has increased the efficiency of DSSCs to more than 15%.[8] With the potential in DSSCs as the future solar cell technology, it has attracted investments from companies such as Sharp Corporation, 3GSolar Photovoltaics, Fujikura Ltd., and Dyesol.[9]

Conventional DSSCs involve the use of Ru photosensitizers, for example the black dye (**N749**), where it helped to improve the incident photon to current conversion

efficiency (IPCE) to almost 80% thus achieving a record efficiency of about 11% in 2006. The black dye is capable of absorbing into the NIR region, allowing the onset of the photocurrent to be about 900 nm thereby enhancing the overall conversion efficiency of the DSSC significantly.[7a, 8] More than 12% efficiency was achieved when a zinc porphyrin dye (**YD2-*o*-C8**, Figure 3.2) was used as the photosensitizer with $Co^{(II/III)}$tris(bipyridyl)–based complex as the redox electrolyte.[10]

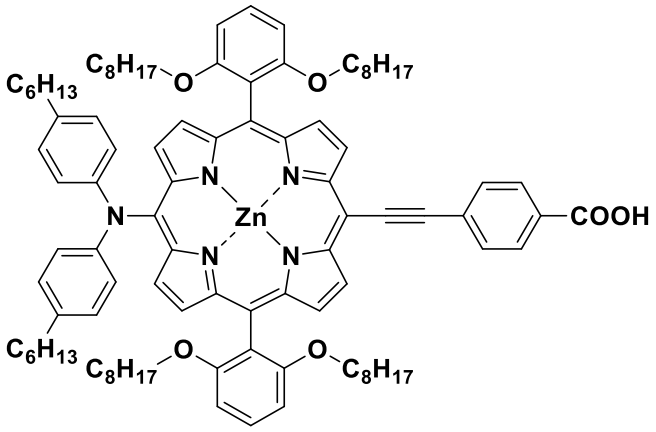

Figure 3.2 The molecular structure of **YD2-*o*-C8**.[10]

Since then, the progress in liquid junctions DSSCs has slowed down and more attention is diverted to the solid-state DSSCs after an impressive 15% power conversion efficiency was recorded with the use of lead iodide perovskite sensitizer.[6b, 11] Nevertheless, the liquid-electrolyte ones are still researched on to further improve its conversion efficiency since they have an advantage in their long-term stability.

3.3 Synthesized Bis(arylimino)acenaphthene (Ar-BIAN) Cu^I Complexes

In our efforts to value-add to the ongoing development of DSSCs, we have synthesized two new Ar-BIAN Cu^I complexes as discussed in Chapter 2. Figure 3.3 shows the molecular structures of the newly synthesized Cu^I compounds (**2.3** and **2.4**). These photosensitizers were tested in DSSCs and the insights gained from the DFT calculations are useful in the development of the next generation Cu^I compounds that can be employed as photosensitizers in artificial photosynthetic and photoredox components.

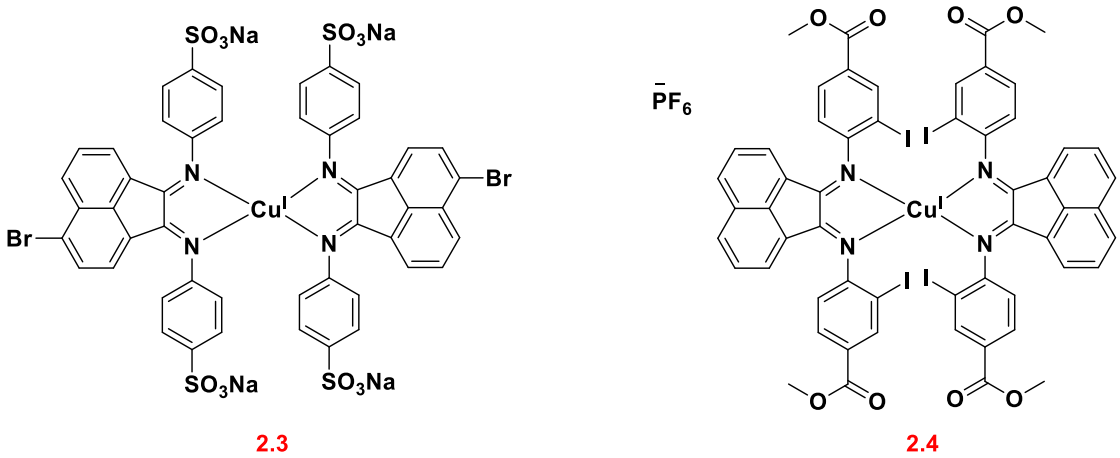

Figure 3.3 Molecular structures of **2.3** and **2.4**.

3.4 Incorporation of the Cu^{I} Light-Harvesters in DSSCs

To test the viability of Cu^{I} Ar-BIANs in DSSCs, we adopted a method reported previously to incorporate **2.3** and **2.4** into such devices.[12] Sulfonates are known to serve as attachment groups on TiO_2 surfaces through electrostatic or covalent linkages. Thus, **2.3** can be conveniently grafted by dipping the TiO_2 into a DMSO solution of **2.3**.[13] However, the anchoring of **2.4** is less straightforward, since the methyl esters do not effectively bind to metal oxides. To circumvent this issue, the TiO_2 was pre-treated with a THF solution of 1.0 M potassium *tert*-butoxide for two days to deprotonate the surface titanol groups and give "Ti-O^{-}" anions prior to dipping the substrate into a DCM solution of **2.4**.[14] The activated TiO_2 surface can then react with the methyl esters to facilitate attachment of **2.4**. After 24 h, the TiO_2 films acquired the solid-state colors of the Cu^{I} complexes. The dyes appeared to be retained successfully since they were not rinsed off the TiO_2 films by the solvents (DMSO for **2.3**; DCM for **2.4**). Each TiO_2 film was then incorporated into a DSSC according to previously published protocols.[12] Despite reports that I^{-}/I_3^{-} electrolytes have been found to be incompatible with Cu^{I} photosensitizers,[15] we sought to collect preliminary data as a proof-of-concept by using the standard I^{-}/I_3^{-} electrolyte. Table 3.1 summarizes measurements made on freshly sealed cells. The solar cells did not give very favorable photocurrent density-voltage (*J-V*) characteristics defined by the following figures of merit – photocurrent density measured at short circuit (J_{sc}), open circuit voltage (V_{oc}), fill factor (FF) and overall power conversion efficiency ($\eta = J_{sc} \times V_{oc} \times FF$).[7a, 16]

Table 3.1 Salient DSSC characteristics using either **2.3** or **2.4**, I^-/I_3^- as electrolyte, and two layers of TiO_2 post-treated with $TiCl_4$.

Compound	J_{SC} **(mA cm^{-2})**	V_{OC} **(mV)**	**FF**	η **(%)**
2.3	0.0325	470	0.66	0.0101
2.4	0.0338	339	0.40	0.0046

The low, but unoptimized efficiencies obtained from the measured *J-V* curves for **2.3** (Figure 3.4a) and **2.4** (Figure 3.5b) demonstrate that the Cu^I Ar-BIAN complexes are capable of electron injection into TiO_2 for rudimentary DSSCs (Figure 3.4c). However, the DSSC characteristics using either **2.3** or **2.4** shown in Table 3.1 are not comparable to solar cells made with state of art Ru-based sensitizers that have J_{sc} = 16-22 mA cm^{-2}, V_{oc} = 0.70-0.86 V, and FF = 0.65-0.80. The low efficiencies of these DSSCs sensitized by **2.3** and **2.4** can partly be explained by considering the charge transfer kinetics and band alignment (Figure 3.4b and Figure 3.5b) for the devices.

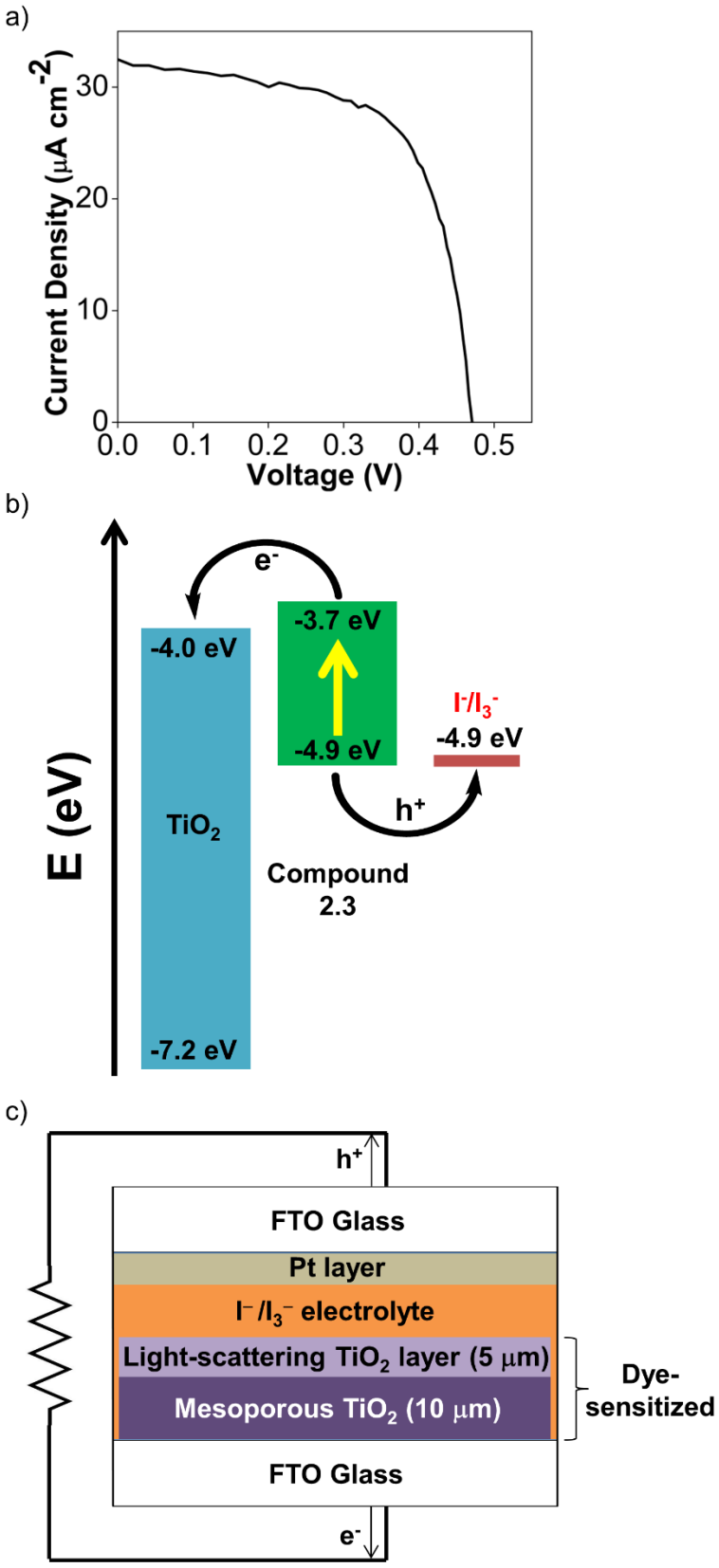

Figure 3.4 (a) *J-V* plot for DSSCs after **2.3** has been adsorbed for dye-sensitization. (b) Band alignment for DSSC incorporated with **2.3**, showing the relative energy levels (in eV against vacuum) for **2.3**, TiO_2, and the I^-/I_3^- electrolyte. (c) General device structure for the DSSCs prepared in this study.

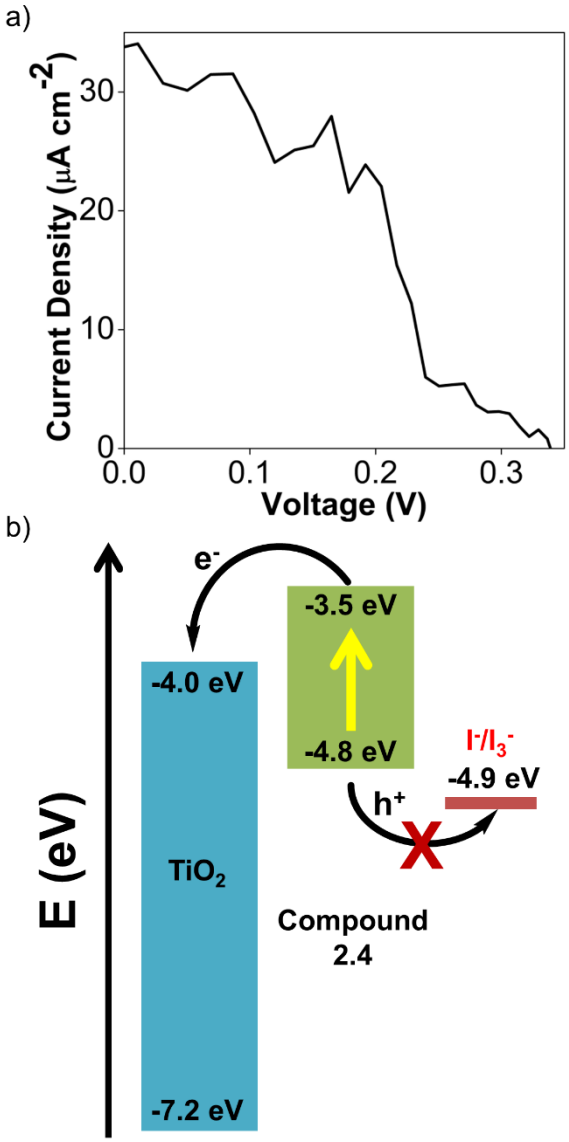

Figure 3.5 (a) *J-V* plot for DSSCs after **2.4** has been adsorbed for dye-sensitization. (b) Band alignment for DSSC incorporated with **2.4**, showing the relative energy levels (in eV against vacuum) for **2.4**, TiO_2, and the I^-/I_3^- electrolyte.

In **2.3**, its LUMO is localized around the iminyl and acenaphthyl moieties of the Ar-BIAN ligand (Figure 3.6), whereas the sulfonate anchoring group that attaches the complex to TiO_2 is on the aniline ring. This may result in less efficient electron injection into TiO_2, since the LUMO containing the photoexcited electron will not have an effective overlap with the conduction band of the TiO_2. For **2.4**, the low efficiency can be further attributed to poor dye regeneration as a result of its HOMO of -4.8 eV being higher in energy than that of the I^-/I_3^- electrolyte which has an energy level of -4.9 eV.

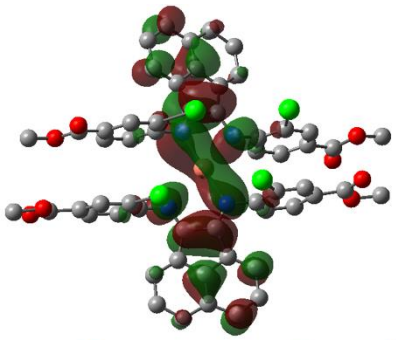

Atomic colors – Cu: orange; C: grey; I: green; N: blue; O: red

Figure 3.6 LUMO of geometry-optimized **2.4** in toluene.

The conditions for these Cu^{I} Ar-BIANs DSSCs can be fine-tuned to improve the stability and response of the Cu^{I} photosensitizers. For instance, the use of tris(bipyridyl) cobalt electrolytes are more suitable in circumventing Cu^{I} formation and also improve the band alignment with the dyes. Moreover, it was observed that after the cell made with **2.4** was sealed, the Cu^{I} dye appeared to leach into the ACN electrolyte solution. The use of bulkier, less-coordinating solvents such as DMSO or γ-butyrolactone may be a better choice. Also, it was previously reported that long hydrocarbon chains on the periphery of the aryl-imino motif can obstruct the approach of the iodide electrolyte through hydrophobic effects to limit the formation of Cu^{I}, as well as minimize recombination processes.[7e, 17]

3.5 Conclusion

Two newly developed Cu^{I} light harvesters have been preliminarily applied as photosensitizers in DSSCs and give solar cells with unoptimized efficiencies of up to 0.010%. Although their efficiencies are low, the results have provided an understanding of the use of Ar-BIAN Cu^{I} complexes in DSSCs. This allows further studies to be done including the judicious design of new derivatives of these Cu^{I} Ar-BIAN photosensitizers, time-resolved spectroscopic experiments, and exploration of their other applications in artificial photosynthesis such as in photoredox catalysis which will be examined in the following chapter.

3.6 Experimental Section

3.6.1 Fabrication of DSSCs and Device Measurements

The device fabrication was carried out as reported elsewhere.[18] Freshly cleaned FTO glass (2.2 mm thickness, 14 Ω/sq sheet resistance, Pilkington) was used as the current collector. The FTO glass was immersed in a 40 mM aqueous $TiCl_4$ solution at 70 ºC for 30 min and rinsed with water and ethanol. The 10 μm-thick transparent TiO_2 layers (Dyesol 18NR-T, average nanoparticle size: 20 nm) and 5 μm-thick scattering TiO_2 layers (Dyesol WER2-O paste, average nanoparticle size: 150-250 nm) were then printed on the FTO glass plates and the plates were annealed under air at 125 ºC for 10 min, at 325 °C for 5 min, at 375°C for 5 min, at 450 °C for 15 min, and finally, at 500 °C for 15 min. The FTO plates were further treated with a 40 mM aqueous $TiCl_4$ solution at 70 °C for 30 min and subsequently annealed at 450 °C for 20 mins. The TiO_2 photoanodes were then made by immersing the plates into either a dye solution of **2.3** (500 μM in DMSO) for 24 h, or a dye solution of **2.4** (500 μM in DCM) for 24 hours after pretreatment with 1.0 M potassium *tert*-butoxide in THF for 48 hours.

The dye-sensitized TiO_2 photoanode and the Pt-coated FTO glass counter electrode were sandwiched together using a 25 μm-thick transparent Surlyn® film (Meltonix 1170-25, Solaronix). The electrolyte was injected through a hole at the back of the counter electrode via vacuum backfilling. The electrolyte employed was a solution containing 1.0 mM 1,3-dimethylimidazolium iodide (DMII), 50 mM LiI, 30 mM I_2, 0.50 mM *tert*-butylpyridine, and 0.10 mM guanidinium thiocyanate (GNCS) in a mixed solvent of ACN and valeronitrile (v/v, 85/15). Finally, the hole was sealed using a 25 μm-thick Surlyn® film and a cover glass (0.1 mm thickness) to avoid leakage of the electrolyte.

Photocurrent density - photovoltage (*J-V*) curves were measured under AM 1.5 (100 mW cm^{-2}) illumination using a solar simulator (San-EI Electric, XEC-301S) equipped with a 450 W xenon lamp, which was coupled with an Agilent semiconductor parameter analyzer (4155C). The power of the simulated light was calibrated to 100 mW cm^{-2} by using a silicon reference cell (Fraunhofer) and monitored using a power meter throughout the testing. A black mask (6 mm x 6 mm) was used in the subsequent photovoltaic studies to avoid the effects of diffusive light on the cell performance. The reported values are calculated based on the average of three batches of devices with identical composition and fabrication procedure.

3.7 References

(1) Kee, J. W.; Ng, Y. Y.; Kulkarni, S. A.; Muduli, S. K.; Xu, K.; Ganguly, R.; Lu, Y.; Hirao, H.; Soo, H. S., *Inorg. Chem. Front.* **2016**, *3*, 651-662.

(2) Solar Energy Basics. https://www.nrel.gov/workingwithus/re-solar.html (accessed Jul, 9).

(3) (a) Pagliaro, M.; Ciriminna, R.; Palmisano, G., *ChemSusChem* **2008**, *1*, 880-891; (b) Green, M. A., *Nat. Energy* **2016**, *1*, 15015; (c) Louwen, A.; van Sark, W.; Schropp, R.; Faaij, A., *Sol. Energy Mater. Sol. Cells* **2016**, *147*, 295-314.

(4) Yunaz, I. A.; Kasashima, S.; Inthisang, S.; Krajangsang, T.; Miyajima, S.; Yamada, A.; Konagai, M., *Effect of Light Intensity on Performance of Silicon-Based Thin Film Solar Cells*, IEEE, Philadelphia, PA, USA, 2009

(5) O'Regan, B.; Grätzel, M., *Nature* **1991**, *353*, 737-740.

(6) (a) Jen, H. P.; Lin, M. H.; Li, L. L.; Wu, H. P.; Huang, W. K.; Cheng, P. J.; Diau, E. W., *ACS Appl. Mater. Interfaces* **2013**, *5*, 10098-10104; (b) Ye, M.; Wen, X.; Wang, M.; Iocozzia, J.; Zhang, N.; Lin, C.; Lin, Z., *Mater. Today* **2015**, *18*, 155-162.

(7) (a) Gratzel, M., *Acc. Chem. Res.* **2009**, *42*, 1788-1798; (b) Gong, J.; Liang, J.; Sumathy, K., *Renew. Sust. Energ. Rev.* **2012**, *16*, 5848-5860; (c) Hagfeldt, A.; Vlachopoulos, N., Dye-Sensitized Solar Cells. In *The Future of Semiconductor Oxides in Next-Generation Solar Cells*, Lira-Cantu, M., Ed. Elsevier: 2018; pp 183-239; (d) Grätzel, M., *J. Photochem. Photobiol. C* **2003**, *4*, 145-153; (e) Nazeeruddin, M. K.; Baranoff, E.; Grätzel, M., *Solar Energy* **2011**, *85*, 1172-1178.

(8) Upadhyaya, H. M.; Senthilarasu, S.; Hsu, M.-H.; Kumar, D. K., *Sol. Energy Mater. Sol. Cells* **2013**, *119*, 291-295.

(9) (a) Dye Sensitized Solar Cell Market Analysis By Application (Portable Charging, BIPV/BAPV, Embedded Electronics, Outdoor Advertising, Automotive (AIPV)) And Segment Forecasts To 2022. https://www.grandviewresearch.com/industry-analysis/dye-sensitized-solar-cell-market (accessed Jul, 15); (b) Zhang, S.; Yang, X.; Numata, Y.; Han, L., *Energy Environ. Sci.* **2013**, *6*, 1443-1464.

(10) Yella, A.; Lee, H. W.; Tsao, H. N.; Yi, C.; Chandiran, A. K.; Nazeeruddin, M. K.; Diau, E. W.; Yeh, C. Y.; Zakeeruddin, S. M.; Gratzel, M., *Science* **2011**, *334*, 629-634.

(11) Burschka, J.; Pellet, N.; Moon, S. J.; Humphry-Baker, R.; Gao, P.; Nazeeruddin, M. K.; Gratzel, M., *Nature* **2013**, *499*, 316-319.

(12) (a) Bozic-Weber, B.; Constable, E. C.; Furer, S. O.; Housecroft, C. E.; Troxler, L. J.; Zampese, J. A., *Chem. Commun.* **2013**, *49*, 7222-7224; (b) Ito, S.; Murakami, T. N.; Comte, P.; Liska, P.; Gratzel, C.; Nazeeruddin, M. K.; Gratzel, M., *Thin Solid Films* **2008**, *516*, 4613-4619.

(13) (a) Bauer, C.; Jacques, P.; Kalt, A., *Chem. Phys. Lett.* **1999**, *307*, 397-406; (b) Stylidi, M.; Kondarides, D. I.; Verykios, X. E., *Applied Catalysis B: Environmental* **2003**, *40*, 271-286.

(14) He, J.; Hagfeldt, A.; Lindquist, S.-E.; Grennberg, H.; Korodi, F.; Sun, L.; Åkermark, B., *Langmuir* **2001**, *17*, 2743-2747.

(15) Bozic-Weber, B.; Constable, E. C.; Housecroft, C. E., *Coord. Chem. Rev.* **2013**, *257*, 3089-3106.

(16) Chung, I.; Lee, B.; He, J.; Chang, R. P.; Kanatzidis, M. G., *Nature* **2012**, *485*, 486-489.

(17) Bozic-Weber, B.; Chaurin, V.; Constable, E. C.; Housecroft, C. E.; Meuwly, M.; Neuburger, M.; Rudd, J. A.; Schonhofer, E.; Siegfried, L., *Dalton Trans.* **2012**, *41*, 14157-14169.

(18) Nguyen, L. H.; Mulmudi, H. K.; Sabba, D.; Kulkarni, S. A.; Batabyal, S. K.; Nonomura, K.; Gratzel, M.; Mhaisalkar, S. G., *Phys. Chem. Chem. Phys.* **2012**, *14*, 16182-16186.

Chapter 4

Spectroscopic Characterization and Mechanistic Studies on Visible Light Photoredox Carbon-Carbon Bond Formation by Bis(Arylimino)Acenaphthene Copper Photosensitizers

4.1 Foreword

Previously mentioned in Chapter 2 and 3, we have developed two new Ar-BIAN Cu^{I} complexes in our attempt to look into more earth-abundant alternatives which have an ease of synthesis. In Chapter 3, the newly developed Cu^{I} complexes were incorporated into DSSCs, but their performances were lackluster therefore Chapter 4 discusses the modification of the previous ligand design and the employment of the new complexes in other artificial photosynthetic applications such as in catalyzing photoredox reactions.

Chapter 4 is based on the work published in ACS Catalysis and adapted with permission from *ACS Catal.* **2018**, *8*, 11277-11286. Copyright © 2018 American Chemical Society. I was the first author and responsible for the synthesis and characterization of the compounds. Lisa Jiaying Tan and Yoke Tin Chai assisted with the synthesis of a few of the compounds. Shue Mei Ng performed the time-correlated single photon counting (TCSPC) measurements. Dr. Ganguly was instrumental in the crystallographic analysis, Dr. Du performed the X-ray absorption spectroscopy (XAS) and Dr. Yeow provided insightful suggestions during manuscript preparations.

Spectroscopic Characterization and Mechanistic Studies on Visible Light Photoredox Carbon-Carbon Bond Formation by Bis(Arylimino)Acenaphthene Copper Photosensitizers

Yik Yie Ng, Lisa Jiaying Tan, Shue Mei Ng, Yoke Tin Chai, Rakesh Ganguly, Yonghua Du, Edwin Kok Lee Yeow, and Han Sen Soo*

4.2 Abstract

Currently, the most popular molecular photosensitizers used for synthetic organic chemistry and energy applications are still the noble metal-based ruthenium and iridium complexes that usually require expensive metal and ligand precursors. In contrast, bis(arylimino)acenaphthene (Ar-BIAN) are established redox non-innocent π-accepting ligands that are easily assembled in one condensation step from affordable and commercially available precursors. Herein, we have developed a series of Ar-BIAN Cu^{I} complexes as visible light harvesting photosensitizers. Notably, one of these panchromatic, homoleptic Ar-BIAN Cu^{I} complexes exhibits a *radiative* recombination lifetime that is longer than diffusion control, as observed by time-correlated single

photon counting spectroscopy. The Ar-BIAN Cu^{I} facilitates visible-light promoted atom transfer radical addition reactions *via* carbon-carbon bond formation with CBr_3 radicals in good yields of up to 75%. Steady-state and transient absorption spectroscopic measurements, together with spectroelectrochemical experiments and intermediate isolation studies, were performed to obtain insights into this photoredox catalysis and provide guidelines for the general deployment of Ar-BIAN Cu^{I} photosensitizers in synthetic organic chemistry and renewable energy applications.

4.3 Introduction

The storage of solar energy in the form of chemical bonds, also known as artificial photosynthesis or the production of solar fuels,[1] is an increasingly attractive and complementary approach to photovoltaics for sustainable energy production. This is exemplified in Chapter 3 where the newly developed Cu^{I} complexes were incorporated into DSSCs.[2] Furthermore, (visible) light is progressively being adopted as an alternative, eco-friendly energy source to drive photoredox catalysis in a renaissance for the application of organic radical chemistry in synthetic methodology under mild reaction conditions.[3] Previously discussed in section 1.3, one of the critical components in sophisticated artificial photosynthetic units, photoredox reactions, and even photovoltaics such as DSSCs[4] is the light harvester, which is necessary for the conversion of photon energy into chemical potential. Effective solar energy harvesters should ideally be panchromatic and absorb even some of the NIR wavelengths without compromising too much on the anodic and cathodic chemical potentials that can be derived. Moreover, to serve as a photosensitizer that can power the multi-electron catalytic processes in artificial photosynthesis, the excited state lifetimes must be sufficiently long to ensure that charge injection or transfer occurs before unproductive recombination processes. In this respect, molecules comprising precious metals like ruthenium (Ru), iridium (Ir), and platinum (Pt),[5] or synthetically laborious ligands such as porphyrins, phthalocyanines, and corroles[6] have remained the mainstay of photosensitizers most commonly employed. However, the prohibitive high costs and toxicity of heavy metal-based chromophores have added impetus to the development of more sustainable and affordable alternatives, including organic or copper (Cu) dyes.[7]

Cu^{I} chromophores with suitable π-acceptor ligands have been likened to Ru^{II} polypyridyl complexes, since both classes of compounds can absorb visible light by

MLCT transitions, while minimizing non-radiative losses through energetically accessible dark states in other spin manifolds.[8] However, unlike the Ru^{II} complexes, effective Cu^{I} photosensitizers that have amply long lifetimes for photochemistry typically possess bulky pyridine cores with branched hydrocarbon chains on the periphery,[8b, 9] which can avert the structural reorganizations that are expected of transient Cu^{I} to Cu^{II} excitations.[10] Consequently, the ligands require expensive precursors and consist of demanding synthetic routes with palladium-catalyzed coupling reactions, which negate the benefits from utilizing Cu instead of Ru or Ir.

On the contrary, Ar-BIAN ligands are recognized as versatile, redox non-innocent π-acceptors[11] that are easily assembled by condensation reactions between affordable, commercial anilines and acenaphthenequinone.[12] A number of metal complexes supported by Ar-BIAN ligands have been reported recently,[13] including two in the previous chapters.[2, 14] To understand the photophysical behavior of the Ar-BIAN Cu^{I} dyes, the ligands were re-designed and a series of new Ar-BIAN Cu^{I} complexes were prepared. Electrochemical and transient absorption spectroscopic measurements were conducted on them. The complexes contain only earth-abundant elements, and noble metals have been excluded even during the synthetic process. Gratifyingly, a new homoleptic Ar-BIAN Cu^{I} chromophore that exhibits *radiative* recombination lifetimes longer than diffusion control is observed for the first time, and has been employed in photocatalytic carbon-carbon bond formation reactions as a proof of concept. In the following sections, the experimental findings on the Cu^{I} photosensitizers will be explained, with an example of their application in photoredox atom transfer radical addition (ATRA),[15] and detailed spectroscopic and mechanistic studies to probe elementary steps of the catalysis will be presented.

Another point to note is the presence of either a hydroxamic acid or an ester group as a substituent on each of the phenyl rings. These functional groups were added as the initial purpose of these Ar-BIAN Cu^{I} complexes were to be anchored onto a semiconductor material as a component of a DSSC. However, in Chapter 3, the preliminary results obtained after incorporating complexes **2.3** and **2.4** into DSSCs were not excellent. Therefore, we examined the potential of these Cu^{I} complexes as catalysts for other useful applications.

4.4 Results and Discussion

4.4.1 Design and Synthesis of Ar-BIAN Ligands and their Corresponding Cu^{I} Complexes (4.1 – 4.6)

The synthetic steps for the substituted Ar-BIAN ligands and detailed characterization data are described in section 4.7. Briefly, the precursors for the ligands were prepared according to the procedures previously reported and they were rather straightforward with moderate yields obtained.[16] For the ligand synthesis, the protocol reported by Gasperini and co-workers[12] was adapted for the synthesis of Ar^{NHOH}-$BIAN^{Br}$ (**4.1**), while $Ar^{Br,OMe}$-BIAN (**4.2**) and Ar^{OMe}-$BIAN^{Br}$ (**4.3**) were synthesized via a $TiCl_4$-promoted condensation[2, 17] to give moderate yields. Of the three ligands synthesized, the ^1H NMR of **4.2** gave broader signals due to the presence of both the (*E*,*E*)- and (*E*,*Z*)-isomers similar to what was observed for ligand **2.2** in the previous chapter since they have an almost identical molecule design.

Subsequently, treatment of suspensions of $[(CH_3CN)_4Cu^{I}]PF_6$ in DMF or DCM, with solutions of the corresponding Ar-BIAN in the same solvent under N_2 gave rise to the respective Ar-BIAN Cu^{I} complexes: $[(Ar^{NHOH}\text{-}BIAN^{Br})_2Cu^{I}]PF_6$ (**4.4**), $[(Ar^{Br,OMe}\text{-}BIAN)_2Cu^{I}]PF_6$ (**4.5**), and $[(Ar^{OMe}\text{-}BIAN^{Br})_2Cu^{I}]PF_6$ (**4.6**) (Scheme 4.1).

Scheme 4.1 Synthesis of the Ar-BIAN ligands (**4.1** – **4.3**) and Cu^{I} complexes (**4.4** – **4.6**).

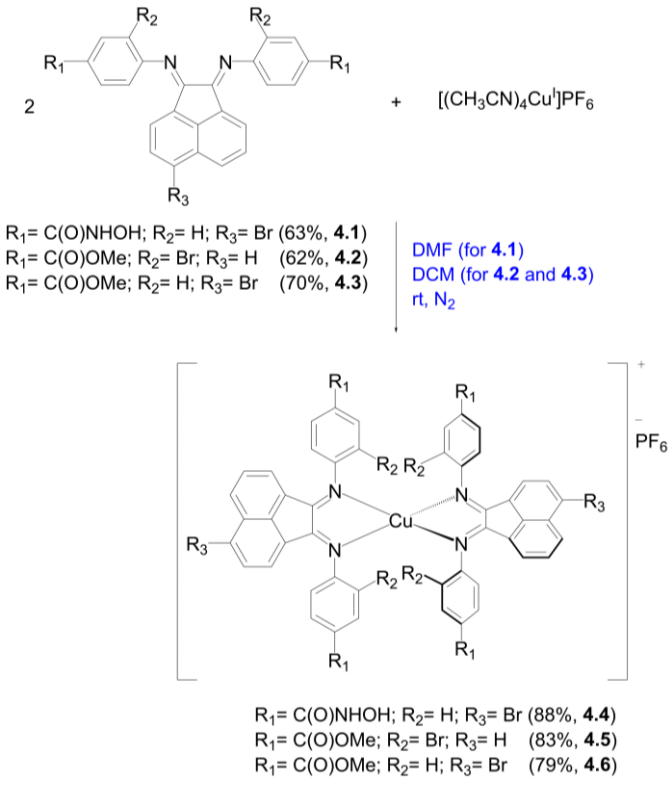

Crystals of **4.4** suitable for single crystal X-ray diffraction were obtained by recrystallization from DMF layered below a solution of Et_2O and 1,2-dimethoxyethane (DME) to obtain a dark red block with a monoclinic C 1 2/c 1 space group (Figure 4.1). The bite angles of the Ar-BIAN are almost identical, with an average of 82.8° while the average of the almost equivalent Cu-N bond lengths is 2.03 Å. The aromatic rings of the 4-aminobenzohydroxamic acid group are positioned in a nearly orthogonal manner to the acenaphthene plane with a dihedral angle of 89.2(5)°. However, the crystal contained disordered solvent molecules in the unit cell, resulting in C-C bond distances that may not be very accurate. Nevertheless, the ORTEP of **4.4** in Figure 4.1 exhibits the expected distorted tetrahedral geometry around Cu^I, which is consistent with other tetrahedral Ar-BIAN Cu^I complexes.[13b, 13c, 18]

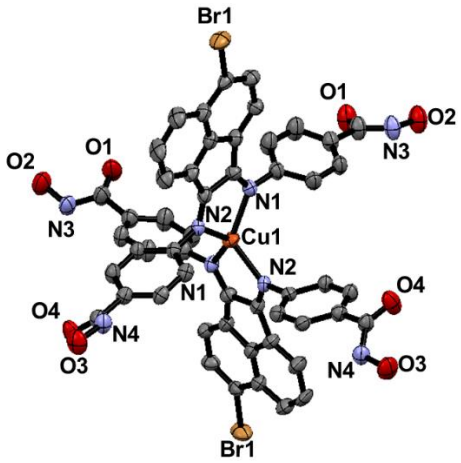

Figure 4.1 ORTEP from single crystal X-ray diffraction experiment of **4.4**. The PF_6^- counter-anion and the hydrogen atoms have been omitted for clarity. The thermal ellipsoids are at 50% probability.

4.4.2 Electrochemical Measurements

To determine the feasibility of complexes **4.4** – **4.6** in redox catalysis, cyclic voltammetry (CV) experiments were performed on them. Electrochemical measurements were performed for all the compounds **4.1** – **4.6** in DMF or DCM depending on their solubilities, containing 0.10 M tetrabutylammonium hexafluorophosphate (TBAH). All potentials (Table 4.1) reported and discussed subsequently are referenced against the ferrocenium ion/ferrocene redox couple (Fc^+/Fc).

A chemically quasi-reversible redox wave was observed for **4.6** at $E_{1/2}$ = +0.29 V (Figure 4.2a) and is assigned to the $Cu^{II/I}$ couple. The anodic and cathodic peak currents, i_p^{red}/i_p^{ox} approaches unity as the scan rate was increased while plots of the peak current *versus* the square root of the scan rates are linear (Figure 4.3), as expected for a diffusion-limited process at the electrode. Similarly, during a cathodic scan, a quasi-reversible reduction wave was detected at $E_{1/2}$ = –1.0 V, as depicted in Figure 4.2b. In addition, comparable redox behaviors were observed for **4.5** since both complexes have similar structures except for the position of the bromide atoms. Due to the poor solubilities of **4.1** and **4.4** in DCM, the CV experiments were conducted in DMF instead. Hence, cathodically shifted redox potentials were observed for **4.4**, and because of the difference in the solvents used, it is rather inaccurate to do a fair comparison between **4.4** and the other two Cu complexes. Therefore, **4.4** was not considered as a photocatalyst candidate for subsequent photoredox reactions. Nevertheless, the reversibility of the redox waves in **4.5** and **4.6** suggest that the regeneration of the complexes after photocatalytic activity should be plausible, which prompted us to explore if they could be applied as photoredox catalysts.

Table 4.1 Electrochemical data for compounds **4.1**-**4.6**[a]

	Anodic Scan					
	E_p^{ox}(I)[d]	E_p^{red}(I)[d]	$E_{1/2}^{ox}$(I)[e]	E_p^{ox}(II)[d]	E_p^{red}(II)[d]	$E_{1/2}^{ox}$(II)[e]
4.1[b]	-	-	-	-	-	-
4.2[c]	-	-	-	-	-	-
4.3[c]	0.32	-	-	0.77	-	-
4.4[b]	-	-	-	-	-	-
4.5[c]	0.65	0.38	0.52	-	-	-
4.6[c]	0.50	0.09	0.29	-	-	-

	Cathodic Scan								
	E_p^{red}(III)[d]	E_p^{ox}(III)[d]	$E_{1/2}^{red}$(III)[e]	E_p^{red}(IV)[d]	E_p^{ox}(IV)[d]	$E_{1/2}^{red}$(IV)[e]	E_p^{red}(V)[d]	E_p^{ox}(V)[d]	$E_{1/2}^{red}$(V)[e]
4.1[b]	-2.26	-2.20	-2.23	-2.03	-	-	-1.55	-	-
4.2[c]	-1.71	-1.53	-1.62	-	-1.13	-	-	-	-
4.3[c]	-1.71	-1.55	-1.63	-1.30	-1.16	-1.23	-	-0.46	-
4.4[b]	-2.31	-2.24	-2.28	-2.08	-	-	-1.51	-	-
4.5[c]	-1.69	-1.50	-1.60	-1.44	-	-	-1.07	-0.91	-0.99
4.6[c]	-	-	-	-1.43	-1.31	-1.37	-1.06	-0.92	-0.99

[a] Conditions: 1.0 mM of compound in 0.10 M TBAH in anhydrous solvent, scan rate: 100 mV s^{-1}; all potentials are given in V *versus* Fc^+/Fc redox couple. [b] Solvent: DMF. [c] Solvent: DCM. [d] E_p^{ox} and E_p^{red} stand for the oxidation and reduction peak potentials respectively. [e] $E_{1/2}^{red}$ stands for the half-wave reduction potential.

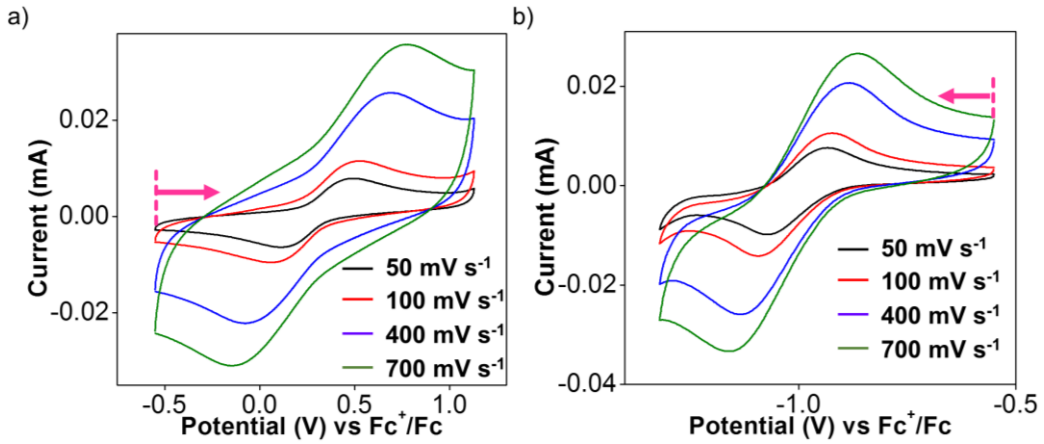

Figure 4.2 Cyclic voltammograms for **4.6** in DCM solutions at different scan rates: under (a) an anodic and (b) a cathodic scan. The pink arrows indicate the scan directions, with vertical dashed lines indicating the initial potentials for each scan.

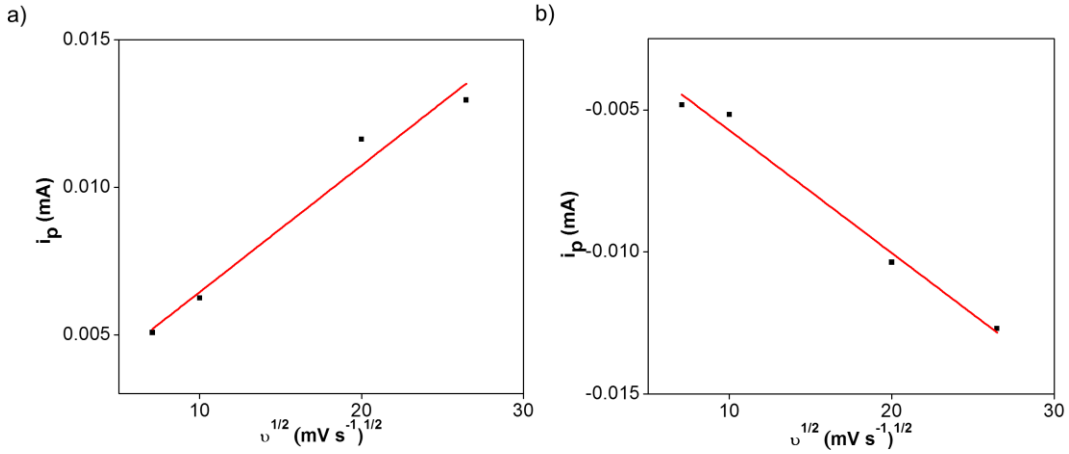

Figure 4.3 Plots of (a) anodic and (b) cathodic peak current (i_p) against the square root of the scan rate ($v^{1/2}$) of **4.6** for its anodic scan.

4.4.3 Optical Absorption and Emission Spectroscopy

Next, UV-visible-NIR spectroscopy was employed to study the absorption characteristics of the Ar-BIAN ligands **4.1 – 4.3** (Figure 4.4a) and the complexes **4.4 – 4.6** (Figure 4.4b), with the intention to explore their utilization as photocatalysts. While their corresponding ligands absorb mostly in the UV region, the complexes **4.4** – **4.6** displayed panchromatic properties. The absorption spectra of **4.1** – **4.3** gave similar characteristics to previously reported Ar-BIAN compounds with strong absorption in the UV region including the weak and broad bands to about 550 nm.[2, 13c, 14b]

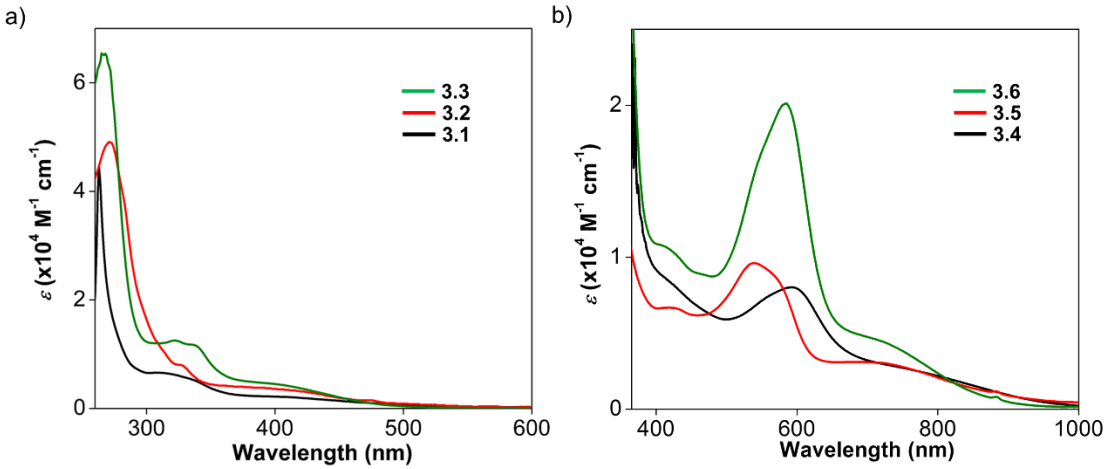

Figure 4.4 Electronic absorption spectra of (a) **4.1** in DMF, and **4.2** and **4.3** in DCM; (b) **4.4** in DMF, and **4.5** and **4.6** in DCM.

Whereas for **4.4** – **4.6**, in addition to the strong absorption in the UV region, they displayed MLCT bands in the visible region and also into the NIR region. Like most previously documented homoleptic Cu^{I} Ar-BIAN complexes,[13b, 13c, 19] no steady-state emission signal was detected for **4.4** and **4.5**. On the contrary, the steady-state luminescence spectra of **4.6** contained emission signals as illustrated in Figure 4.5a. Upon excitation between 430 to 460 nm, **4.6** displayed an emission band at 510 nm. The emission at 510 nm is likely attributed to a ligand-centered emission since **4.3** shows a similar signal (Figure 4.5b).

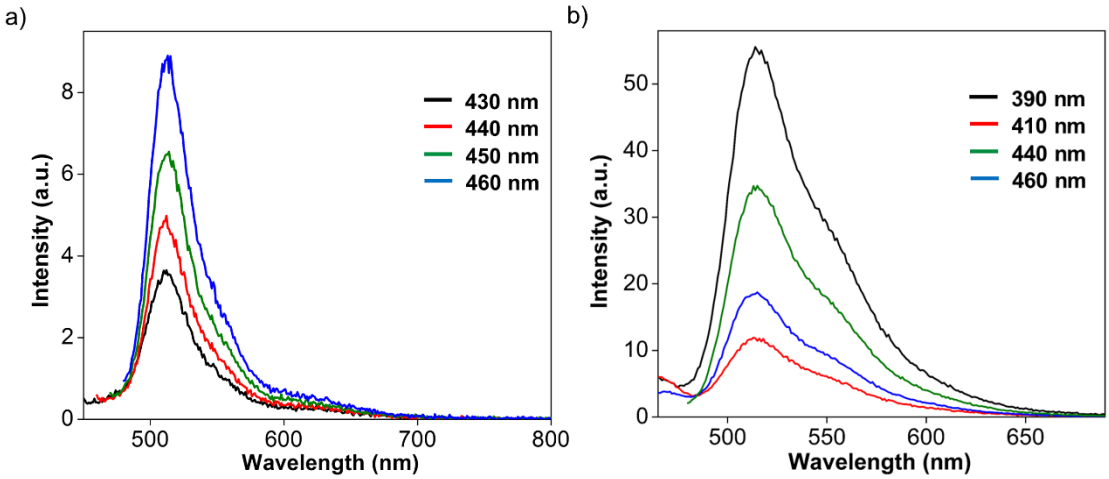

Figure 4.5 Steady state emission spectra of (a) **4.6** and (b) **4.3** in DCM, with the excitation wavelengths labelled in different colors.

The longer-lived emission signal for **4.6** likely arises from the presence of the electron-withdrawing and heavy atom, Br, on the acenaphthene ring. The presence of the bromide functionality localizes the photoexcited negative charges on the acenaphthene motif, thus improving spatial separation of the LUMO from the HOMO on Cu, while the heavy atom facilitates intersystem crossing, both of which lead to longer-lived radiative excited states. Despite these favorable modifications, ligand **4.3** and complex **4.6** have emission quantum yields, Φ_r, of only 5.0 x 10^{-4} and 1.5 x 10^{-4} respectively, with $[Ru(bpy)_3](PF_6)_2$ in DCM ($\Phi_r = 0.029$) used as a reference.[20] The excitation wavelength used for all samples is 390 nm while the integrated area is from 480 – 700 nm. Therefore, the emission quantum yield measured for **4.6** is the total emission feature consisting of both the emission at 510 nm and the weak shoulder at 615 nm.

The radiative quantum yields, φ_r, were measured in DCM solutions. Each sample was prepared in a glovebox under a N_2 atmosphere. The φ_r values were obtained by comparing the photoluminescence intensities to $[Ru(bpy)_3](PF_6)_2$ and calculated using the following expression:

$$\varphi_r = \varphi_{ref} \frac{I}{A} \frac{A_{ref}}{I_{ref}}$$

where φ_{ref} is the known quantum yield of the reference compound. The photosensitizer $[Ru(bpy)_3](PF_6)_2$ dissolved in DCM ($\varphi_r = 0.029$) was used as the reference; *I* is the integrated fluorescence intensity and *A* is the absorbance at the excitation wavelength of the sample (no subscripts) and the reference compound (subscript *ref*).

4.4.4 Transient Absorption and Emission Spectroscopy

Transient absorption and emission spectroscopy (TAS and TES respectively) were performed to investigate the photoexcited behavior and lifetimes of the complexes. For these experiments, the samples were irradiated with UV or visible light pulses of 5 – 8 ns durations. They were then probed by an electronically synchronized broadband xenon lamp beam before and after the pulses, and the intensity of the transmitted light was detected. In all the TAS data in this chapter, the logarithm of the ratio (ΔA) of the transmitted light intensity from the probe beam *after* laser excitation to the transmitted intensity *before* laser excitation are presented. The change in optical density (ΔOD) of

the transient photoexcited state relative to the ground state thus indicates increased absorption (positive ΔA) or reduced absorption/emission (negative ΔA).

Although **4.4** has a Br atom at the same position on the ligand as **4.6**, quenching due to exciplex formation with DMF might have rendered it non-photoluminescent.[21] A strongly binding, polar solvent such as DMF was required for **4.4** due to its poor solubility in non-coordinating solvents such as DCM. This exciplex formation was further confirmed when a TAS was performed and a permanent ground-state bleach was observed at 620 nm as illustrated in Figure 4.6. This phenomenon is similar to a previously published report by Papanikolaou and Tkachenko where they noticed a bleaching of the ground state MLCT absorption of their $[Cu(Ar\text{-}BIAN)_2]BF_4$ complexes at around 600 nm.[19] Upon laser excitation, **4.4** undergoes a MLCT transition between the Cu^I center and the low-lying π* acceptor orbital. The metal center then adopts a d^9 configuration allowing for Jahn-Teller distortion to occur. The structure of the complex will therefore assume a more flattened coordination geometry.[8b, 22] Since DMF is a strong donating solvent, it is likely that the solvent molecule will coordinate to the more 'open' structure of complex forming an exciplex.[21] Hence rendering it non-emissive.

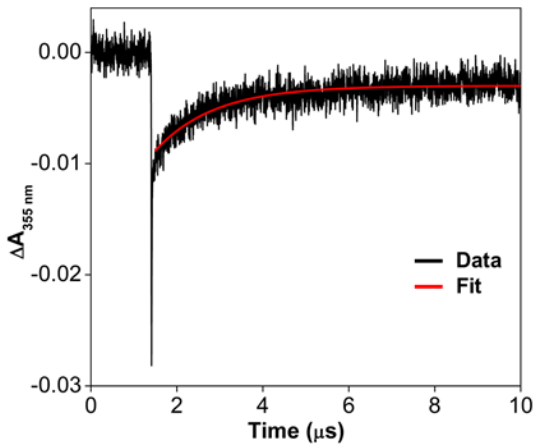

Figure 4.6 Nanosecond transient absorption kinetics recorded at 610 nm after excitation of **4.4** in DMF with 355 nm laser pulses.

The transient absorption and emission spectra of **4.5** are shown in Figure 4.7. As mentioned previously, complex **4.5** does not photoluminesce hence the presence of ground-state bleaching in Figure 4.9a but an almost negligible transient emission signal in Figure 4.7b. Due to its almost nonexistent emission property, complex **4.5** was not considered to be used as a photocatalyst for the photoredox reaction subsequently.

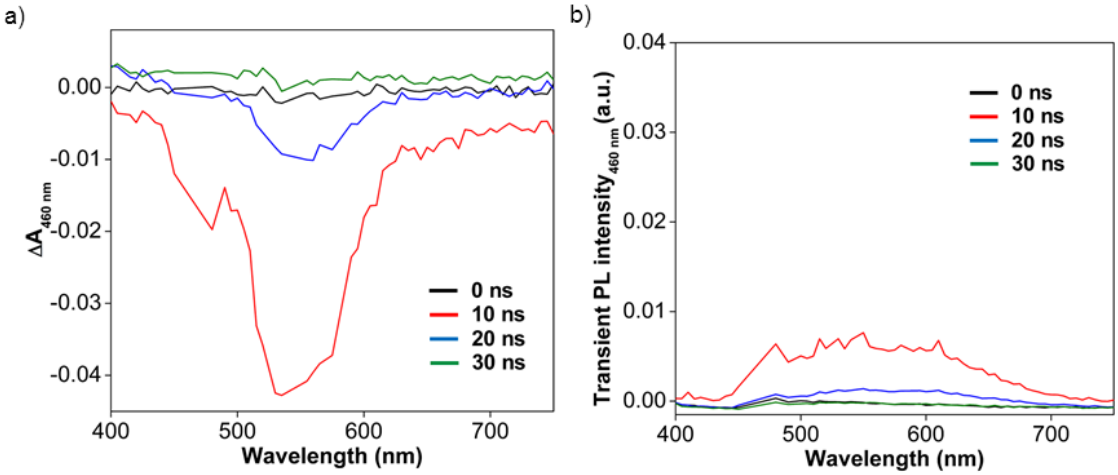

Figure 4.7 (a) Nanosecond transient absorption spectra of **4.5** in DCM; (b) nanosecond transient emission spectra of **4.5** in DCM after laser excitation at 460 nm.

The nanosecond time-resolved optical spectroscopy of the photoluminescent **4.6** was also done to evaluate its suitability for photoredox catalysis. The time evolution of the transient absorption signals of **4.6** are presented in Figure 4.8. The TAS and TES data were obtained after exciting the sample solution with 460 nm laser pulses. The excited state absorption and emission difference spectra were acquired after increasing time intervals as labelled by the different colors in Figure 4.8.

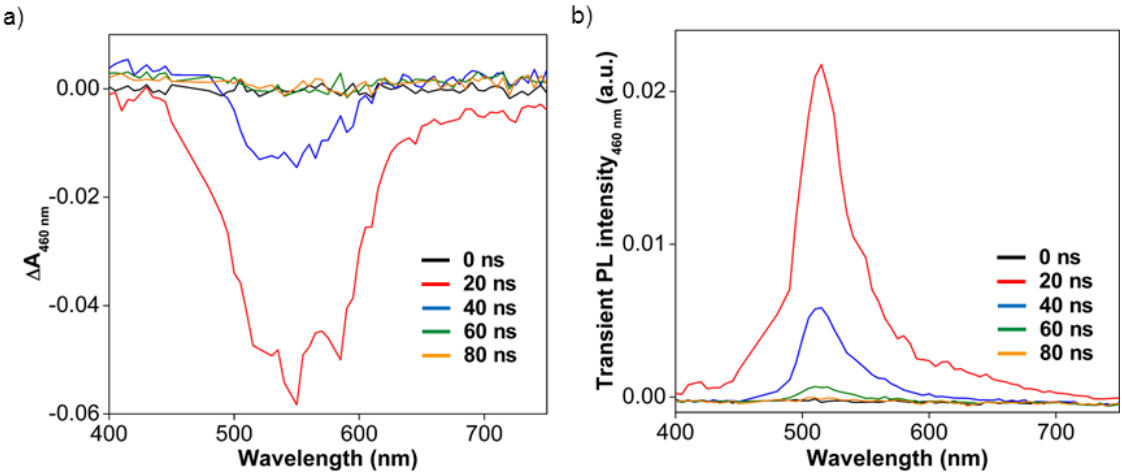

Figure 4.8 Nanosecond transient (a) absorption and (b) emission spectra of **4.6** in DCM, at increasing delay times of 20 (red), 40 (blue), 60 (green), and 80 (orange) ns after the 460 nm pulse.

An absorbance bleach centered at ~550 nm was observed (Figure 4.8a), indicating a ground state bleach of **4.6** superimposed on the excited state emission, as confirmed by the TES obtained between 20 to 80 ns (Figure 4.8b). The latter concurs with the steady-state emission spectra and the time-correlated single photon counting (TCSPC) measurements of **4.6** in DCM at 510 nm upon 466 nm irradiation (Figure 4.9a).

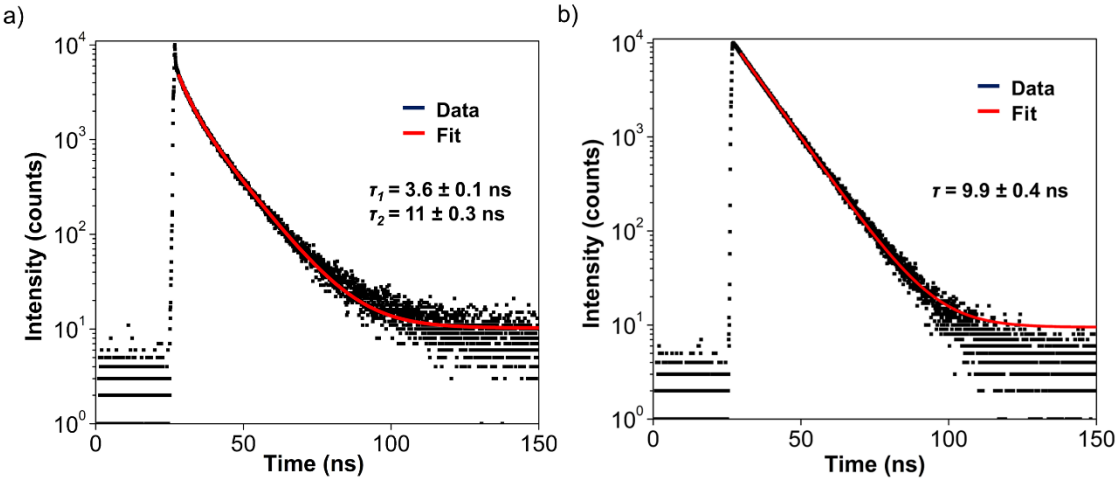

Figure 4.9 Photoluminescence decay of (a) **4.6** and (b) **4.3** in DCM. The samples were excited at 466 nm and the photoluminescence were recorded at 510 nm.

The photoluminescence decay of **4.6** can be fitted with a bi-exponential decay function with a faster component (3.6 ± 0.1 ns) that can be attributed to the relaxation of the MLCT excited state of Cu^{I}. A slower component (11 ± 0.3 ns) is similar to the luminescence lifetime of the ligand, **4.3** (9.9 ± 0.4 ns, Figure 4.9b). The errors corresponding to the fits of the transient signal lifetimes were determined *via* the principle of error propagation by calculating the root-mean-square deviation from the sum of squares of the uncertainties in each measured value. For each time-resolved measurement, the associated uncertainties included the spectrofluorimeter time-resolution, mass of samples, and volumes of samples. Hence, the error of the transient signal lifetime, $\delta\tau$, was calculated according to the following equation:

$$\delta\tau = \tau\sqrt{\left(\frac{\delta\tau_a}{\tau_a}\right)^2 + \left(\frac{\delta m_k}{m_k}\right)^2 + \left(\frac{\delta V_n}{V_n}\right)^2}$$

where τ = transient signal lifetime; $\delta\tau_a$ = uncertainty of the spectrofluorimeter time-resolution; δm_k = uncertainty of the mass of the dissolved samples; δV_n = uncertainty of

the n^{th} volume measurement, where *n* represents the *n* different volume measurements including stock solution and sample preparations.

Compared to the ultrafast optical spectroscopic studies previously reported, when some *heteroleptic* Ar-BIAN complexes were excited at higher energies, the transient optical spectrum was mainly dominated by a triplet ligand-centered relaxation.[19, 23] On the other hand, the photoluminescence decay of **4.6** consists of two contributions. The observation of more than one emission constituent is not uncommon. As described by Casadonte *et al.*, in a rigid matrix, two emission signals were observed from a triplet intraligand (^{3}IL) and a triplet charge transfer (^{3}CT) excited state.[24]

Although the excited state lifetime of **4.6** (~ 4 ns) is shorter than those of the prototypical ruthenium-based photosensitizers such as $Ru(bpy)_3^{2+}$ (488 ns in DCM),[20] it is still one of the longest-lived *panchromatic chromophores* among first-row transition metal complexes. For example, the excited state lifetime of the longest-lived iron-based photosensitizer is 100 ps,[25] while the rest are on the order of tens of picoseconds or shorter.[26] The excited state lifetime of **4.6** is short compared to the state-of-the-art Cu^I-based photosensitizers,[27] an example being $[Cu(dsbtmp)_2]^+$ (dsbtmp = 2,9-di(sec-butyl)-3,4,7,8-tetramethyl-1,10-phenanthroline), which has an excited state lifetime ranging from 1.2 to 2.8 μs.[27a] However, $[Cu(dsbtmp)_2]^+$ is not panchromatic and absorbs only up to 520 nm, and also has a more costly, multi-step ligand synthetic route.[27a]

4.5 Visible-Light Assisted Atom Transfer Radical Addition (ATRA) Reaction

4.5.1 Results and Discussion

With a photoexcited lifetime in the nanosecond regime, the unimolecular recombination rate of **4.6** is now longer-lived than diffusion-controlled reactions, allowing the opportunity to apply it in electron transfer processes such as photoredox catalysis. As a proof-of-concept, the ability of **4.6** to photocatalyze carbon-carbon bond formation *via* ATRA[28] between styrenes and tetrabromomethane (**4.9**) was investigated. Multiple attempts have also been made to find other reaction protocols but many were unsuccessful due to the small potential window of the redox couple for **4.6**. Some photocatalytic reactions that were attempted include the trifluoromethylation reaction using pyridine *N*-oxide and trifluoroacetic anhydrides previously reported by Beatty *et al*.[29] However, when this reaction was carried out using **4.6**, the reaction did not proceed.

Other reactions including the reduction of bromomalonate or bromotrichloromethane did not proceed as well.[30]

The detailed experimental and characterization of the products obtained from the visible-light assisted ATRA reaction are given in section 4.7. Table 4.2 summarizes the ATRA reaction carried out using visible light. Upon irradiation with two white light LEDs and a low catalyst loading (0.60 mol%), the reaction proceeded with moderate NMR yields (32-75%) calculated by comparison with an internal standard in the NMR. Notably, the photocatalytic reaction could be conducted when light of shorter wavelengths (⩽490 nm) was cut off (entry 6), highlighting an advantage over longer-lived Cu photosensitizers such as $[Cu(dsbtmp)_2]^+$. The control experiments (entries 2 – 6) showed minimal product formation. Although irradiation with the Ar-BIAN ligand alone led to some products, the yields and selectivities were poorer (entries 5, 8, 11), especially for the slower substrates. Electron-donating methyl (entry 12) and electron-withdrawing chloro and cyano (entries 7 and 10) were all tolerated. The low product yield observed in entry 12 is due to the formation of by-product as observed from the crude NMR spectrum and the GC-MS. Some of the by-products observed were 1-methyl-4-(2,2,2-tribromoethyl)benzene and chloroform. The cyano group did not react with the radical intermediates because C=C bond lengths are generally longer than that of C≡N bond lengths. Therefore, it is likely that the CBr_3 radical will prefer to add to the alkene which has a weaker bond strength instead of reacting with the C≡N bond. The nitrile group does not oxidize or reduce easily giving them stability when undergoing redox reactions.[31] Also, the carbon in the nitrile is electrophilic. Since CBr_3 radicals are also electrophilic, there is a mismatch in polarity so reaction between the CBr_3 and C≡N is unlikely. This is further supported by previous reports where the C≡N bond did not react.[32] In addition, fused rings such as naphthalene (entry 13) were also compatible for this reaction. The low yield observed is probably due to the formation of by-products. At the end of the reaction, white precipitate was observed possibly due to polymerization of the vinylnaphthalene. The ^{1}H NMR yields were calculated using the following formula:

$$\text{yield (\%)} = 100\% * \frac{\nu(\text{product})}{\nu(\text{standard})} * n$$

where $\frac{\nu(\text{product})}{\nu(\text{standard})}$ is the integral ratio of the corresponding ^{1}H NMR peaks and n is the standard to starting material (in mol) ratio.

Table 4.2 ATRA Reaction Photocatalyzed by **4.6**[a]

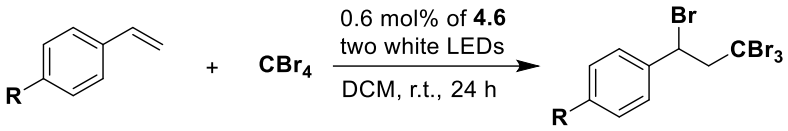

	Alkene	Product	% conv.[b]	Yield (%)[c]	TON[d]	TOF (h^{-1})[e]
1	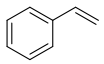	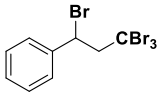	100	74	167	5.15
2[f]			30	<3		
3[g]			18	<1		
4[h]			100	7		
5[i]			100	55		
6[j]			68	28		
7	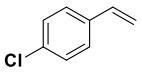	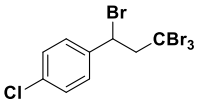	100	75	167	5.15
8[i]			100	55		
9	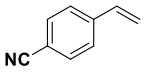	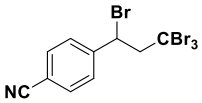	53	44	89	3.69
10[k]			100	75	167	2.58
11[i]			100	30		
12	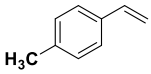	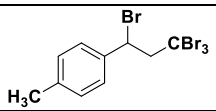	100	44[l]	167	5.15
13	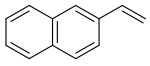	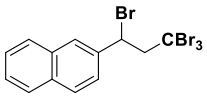	100	32[m, n]	167	5.15

[a] Conditions: Alkene (1 eq.), CBr_4 (1 eq.), **4.6** (0.60 mol%) in DCM (1.0 mL), irradiation with two white LEDs (48 W each) for 24 h. [b] The % conversion of styrene was monitored by ^{1}H NMR spectroscopy. [c] The ^{1}H NMR yields were calculated by comparing against 1,1,2,2-tetrachloroethane as the internal standard. [d] The minimum turnover number (TON): the number of moles of substrate consumed by a mole of **2.6**. [e] The minimum turnover frequency (TOF): TON per unit time. [f] Dark reaction. [g] No catalyst. [h] $[(CH_3CN)_4Cu]PF_6$, no Ar-BIAN ligand. [i] Ar-BIAN ligand (0.60 mol%) only as the catalyst. [j] Irradiation by one LED upon installation of a longpass filter to cut off wavelengths below 490 nm. [k] Reaction time: 48 h. [l] The desired ATRA product was not isolated due to hydrolysis upon purification to form 4-methyl-α-(2,2,2-tribromoethyl)benzenemethanol. [m] The desired ATRA product was not isolated due to hydrolysis upon purification to form 3,3,3-tribromo-1-(naphthalen-2-yl)propan-1-ol. [n] The NMR spectra of both the crude reaction mixture and the hydrolyzed product have been presented as Figures A.26-28.

4.5.2 Evaluating the Reaction Pathway of the Photocatalyzed ATRA Reaction

The products obtained agree with those from previously reported Cu^{I}-photocatalyzed ATRA reactions.[15c, 15d] As shown in Scheme 4.2, we propose that the photoexcited Cu^{I} complex transfers an electron to **4.9** to generate a CBr_3 radical (**4.10**), which adds to the styrene. The resulting intermediate (**4.11**) is then oxidized by the Cu^{II} species (**4.8**) to regenerate **4.6**, while **4.12** combines with Br^- to form the desired product (**4.13**).

To obtain insights into the proposed mechanism, UV-visible spectra of the different components (**4.6**, styrene, and CBr_4) were collected at 1 h intervals (Figure 4.10). The UV-visible spectra of the reaction mixture containing only **4.6**, and both **4.6** and styrene showed minimal decreases in the absorbance at 580 nm, as illustrated in Figure 4.11. However, in the absence of styrene, the λ_{max} at 580 nm decreased rapidly (Figure 4.10a), suggesting that **4.6** quickly depleted, due to the lack of **4.11** to reduce **4.8** back to **4.6**. Therefore, after irradiating for 3 h, the MLCT band of **4.6** at 580 nm diminished, which was then followed by the formation of a new species at λ_{max} of 470 nm, preventing the completion of the catalytic cycle.

Scheme 4.2 Proposed Mechanism of the Cu^{I}-Photocatalyzed ATRA of CBr_4 and Styrenes

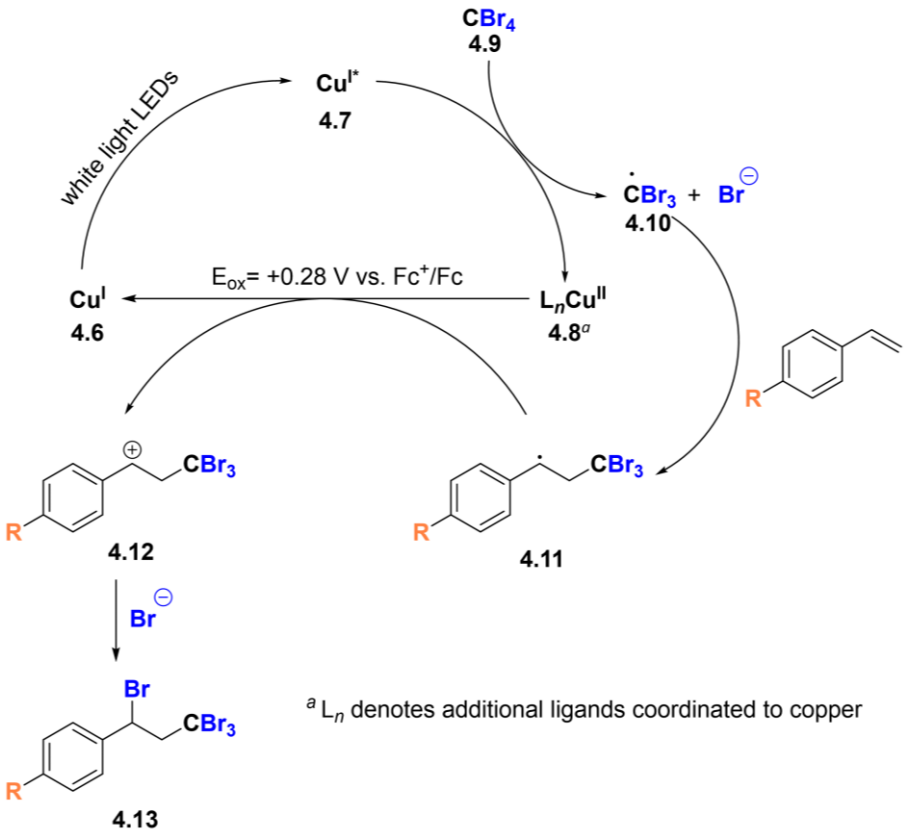

In contrast, when styrene was present, the absorption band at 580 nm persisted (with modest reduction due to photobleaching) even after 5 h of irradiation (Figure 4.10b), which indicated the regeneration of **4.6** during the catalytic cycle *via* the reduction of the Cu^{II} in **4.8**. We attempted to identify **4.8** formed during the photoredox reaction by carrying out spectroelectrochemical measurements on **4.6**. The UV-visible spectra obtained in Figure 4.10c shows the changes in the absorption bands of **4.6** upon its oxidation when a potential of more than +0.50 V (*vs* Fc^{+}/Fc) was applied. This potential was chosen since the CV experiments indicated that **4.6** had a one-electron oxidation wave at 0.29 V (Table 4.1).

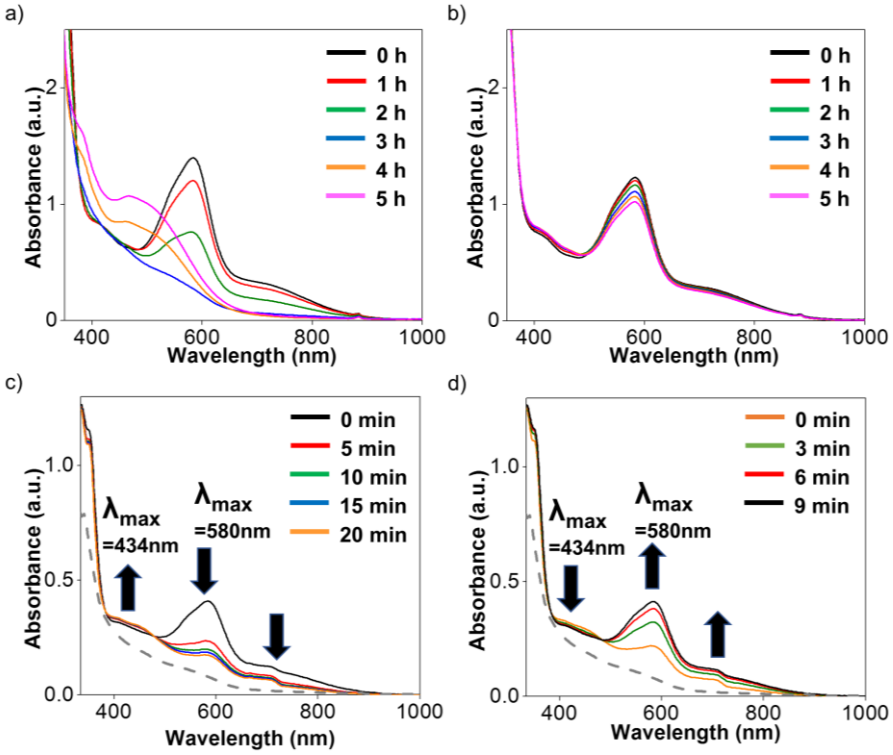

Figure 4.10 UV-visible spectra of the reaction mixture containing (a) only **4.6** and CBr_4, and (b) **4.6**, styrene, and CBr_4 at 1 h intervals. UV-visible spectra of **4.6** obtained by spectroelectrochemical measurements (c) when an oxidative potential is applied at 0.30 V with the time points at 0 (black), 5 (red), 10 (green), 15 (blue), and 20 (orange) min; and (d) when a reductive potential of -0.13 V is applied on the orange sample in (c) with the time points at 0 (orange), 3 (green), 6 (red), and 9 (black) min. In both (c) and (d), the intermediate from the reaction between **4.6** and CBr_4 after 3 h (grey dashed line) has been reproduced and normalized from (a).

The absorption band at 580 nm was diminished whereas the band at 434 nm grew slightly after **4.6** was oxidized electrochemically (black to orange, Figure 4.10c). Remarkably, the final spectrum after one-electron oxidation (orange line, Figure 4.10c) appears to be very similar to the intermediate from the reaction between **4.6** and CBr_4 after 3 h (grey dashed line, Figure 4.10c, reproduced from Figure 4.10a). When a reductive potential at -0.20 V was applied, the characteristic absorption at 580 nm was recovered, while the band at 434 nm decreased slightly to regenerate the original UV-visible spectrum of **4.6** (Figure 4.10d). Therefore, we postulate that **4.8** in the photoredox catalytic cycle could be the one-electron oxidized intermediate obtained during the spectroelectrochemical experiments.

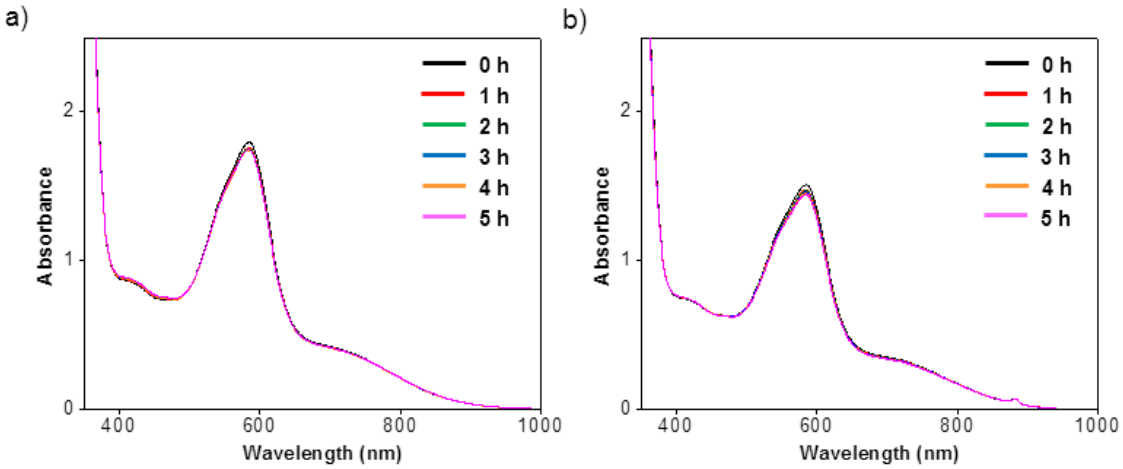

Figure 4.11 UV-visible spectra of the reaction mixture containing (a) only **4.6**, and (b) both **4.6** and styrene at 1 h intervals. The slight decrease in the absorbance signals indicates that there was slight photobleaching of **4.6** upon white light irradiation, but no reaction with styrene.

Attempts were made to isolate and identify **4.8** by irradiating a mixture of **4.6** and a stoichiometric equivalent of CBr_4. Brown precipitate was collected, but single crystals could not be obtained after multiple recrystallization attempts. Therefore, the UV-visible spectrum of the brown precipitate was obtained and compared to the chemically oxidized **4.6**, which was formed by mixing tris(2,4-dibromophenyl)aminium hexafluoroantimonate ('Magic Green') with **4.6** to obtain a Cu^{II} product (**4.14**). However, as illustrated in Figure 4.12, the UV-visible spectra of **4.8** and **4.14** are patently distinct. Complex **4.14** consists of an octahedral Cu^{II} center with ACN molecules bound in the axial positions. A fully refined structure of **4.14** was not obtained due to the presence of disorder in the location of the Br atoms and also disordered molecules. ACN

was necessary for the recrystallization of **4.14** due to its poor solubility in less polar solvents. In order to elucidate a more precise crystal structure, the non-bromide version of **4.14** was grown using the same solvent combination and the crystal structure is given in Figure 4.12c.

As anticipated for octahedral and distorted octahedral Cu^{II} complexes with ACN bound,[33] the higher symmetry and orbitally forbidden nature of the d-d transitions of **4.14** result in weak visible absorption bands. On the other hand, the optical absorption bands of **4.8** are dramatically red-shifted with intensity even in the NIR region up to around 1000 nm. Therefore, we anticipate that **4.8** is unlikely to have a distorted octahedral geometry similar to **4.14** but may have a lower symmetry or could have at least one Br^- bound. This has been supported by Olshin and co-workers, who reported that Cu^{II} complexes in ACN, with increasing equivalents of added Br^-, demonstrated a marked red shift in their d-d absorption bands and a decrease in coordination number from six.[33]

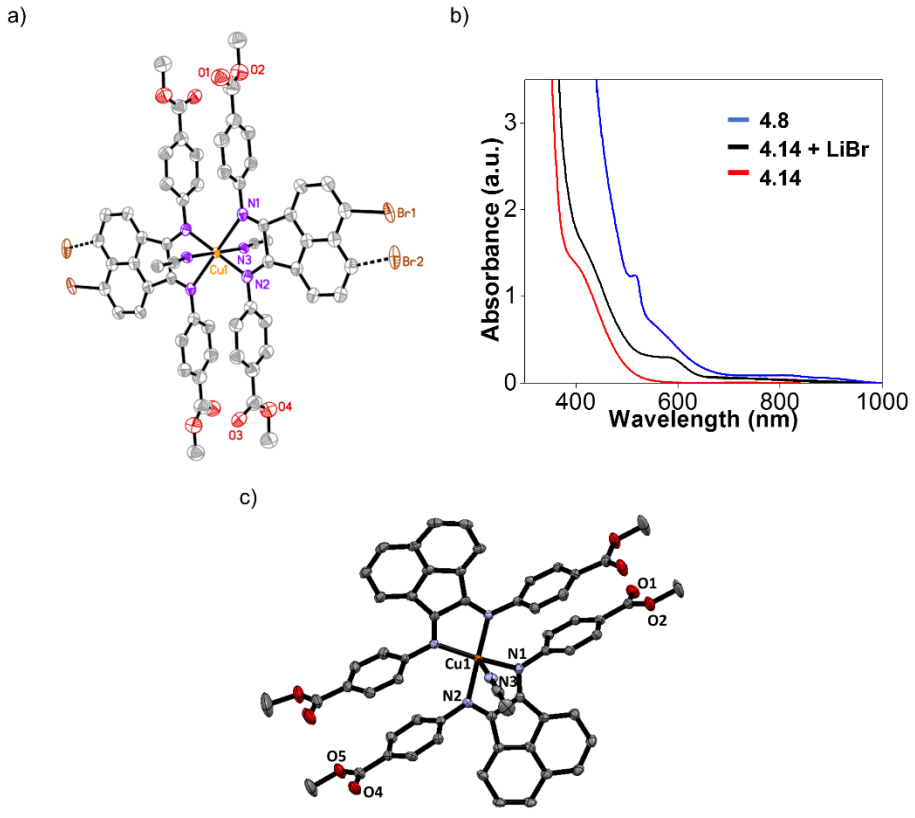

Figure 4.12 (a) ORTEP from the single crystal X-ray diffraction experiment of **4.14**. The thermal ellipsoids are at 50% probability. The structure of **4.14** has not been fully refined due to severe disorder in the position of the Br atoms. A model with equal occupancy of the Br as Br1

and Br2 provided adequate refinement, but the disordered solvent molecules could not be refined any further. The two counter-anions and the hydrogen atoms have been omitted for clarity. (b) UV-visible spectra comparison between **4.8**, **4.14** after stirring with two equivalents of LiBr, and **4.14**. (c) ORTEP from the single crystal X-ray diffraction experiment of the non-bromide version of **4.14**. The thermal ellipsoids are at 50% probability.

To further corroborate this proposed identity of **4.8**, 2.0 equivalents of LiBr was added to **4.14**. The steady-state absorption spectrum is displayed in black in Figure 4.11b. Gratifyingly, this product now shows red-shifted absorption bands in the NIR region, intermediate between **4.8** and **4.14**, although it is still not coincident with **4.8**. Thus, we propose that **4.8** may be a Cu^{II} complex with CBr_3 or Br^- coordinated, with a lower square pyramidal or trigonal bipyramidal symmetry. Additional in situ X-ray absorption spectroscopic experiments with photolysis will be necessary, which is beyond the scope of this thesis.

4.6 Conclusion

In this chapter, the development and characterization of several panchromatic Ar-BIAN Cu^I complexes, one of which displays *radiative* recombination rates that are longer-lived than diffusion control, are described. Notably, it has been demonstrated that this luminescent Ar-BIAN Cu^I complex is capable of photocatalytically facilitating ATRA carbon-carbon bond formation reactions under ambient conditions. Insights into the reaction pathway of the photocatalytic cycle indicate that exciplex formation by coordination of photogenerated radicals may be occurring. Consequently, in addition to the introduction of electron-withdrawing heavy atoms on the acenaphthene motif to increase the photoexcited lifetimes, more steric protection of the Cu^I center will be necessary in future generations of Ar-BIAN Cu^I complexes for them to become generally exploitable in solar energy harvesting and synthetic organic chemistry applications.

4.7 Experimental Section

4.7.1 General Considerations

The Cu complexes used in this study were synthesized in a glovebox under a N_2 atmosphere. Deuterated solvents were purchased from Cambridge Isotope Laboratories

and were distilled prior to use. The other chemicals were obtained from Sigma-Aldrich and were used as received. Compounds 4-aminobenzohydroxamic acid[16a] and 5-bromoacenaphthylene-1,2-dione[16b] were synthesized according to previously published procedures. The ^{1}H and ^{13}C spectra were recorded at room temperature on a Bruker AVANCE 400 MHz spectrometer. The ^{1}H and ^{13}C chemical shifts (δ reported in ppm) are referenced to the residual solvent signal(s). Elemental analyses were performed with an Elementar vario MICRO cube analyser. High-resolution mass spectra (HRMS) were obtained with a Q-TOF Premier LC HR mass spectrometer.

UV-visible spectroscopic measurements were performed using a Shimadzu UV-3600 UV-Vis-NIR Spectrophotometer. Photoluminescence decay profiles were recorded on a time-correlated single-photon counting (TCSPC) spectrofluorimeter (Fluorocube, Horiba Jobin Yvon). The samples were excited at 466 nm using a pulsed diode laser (NanoLED-466 L, Horiba Jobin Yvon) and the photoluminescence decay signals were recorded at 510 nm. The transient absorption and emission measurements were performed using an Edinburgh Instruments model LP920 transient absorption spectrometer equipped with a pulsed Xe probe lamp in conjunction with a Nd:YAG laser (Continuum model Surelite II-10) as the excitation source. The laser pulse width is 5-8 ns and the repetition rate is 10 Hz. During transient absorption measurements, the pulses are synchronized with the LP920 system at a frequency of 1 Hz. The pulse energy used was between 6-23 mJ/pulse.

4.7.2 Synthesis of Ligand Precursors

4-aminobenzohydroxamic acid

Compound 4-aminobenzohydroxamic acid was prepared according to the procedures previously reported.[16a] The ^{1}H and ^{13}C NMR spectra confirmed the identity of the product, which was collected in 72% yield as a beige solid. ^{1}H NMR (500 MHz, DMSO-d_6): δ 5.58 (s, 2 H, NH_2), 6.52 (d, J = 8.5 Hz, 2 H, aromatic H), 7.46 (d, J = 8.5 Hz, 2 H, aromatic H), 8.63 (s, 1 H, NH), 10.72 (s, 1 H, OH) ppm. ^{13}C NMR (101 MHz, DMSO-d_6): δ 112.7, 119.3, 128.3, 151.6, 165.1 ppm. ESI-MS calcd. for $C_7H_9N_2O_2$, $[M+H]^+$ m/z = 153.06, found 153.01.

5-bromoacenaphthylene-1,2-dione

Compound 5-bromoacenaphthylene-1,2-dione was prepared according to the procedures previously reported.[16b] The ^{1}H and ^{13}C NMR spectra confirmed the identity of the product, which was collected in 54% yield as an orange solid. ^{1}H NMR (500 MHz, DMSO-d_6): δ 7.98 (d, J = 7.5 Hz, 1 H), 8.06 (dd, J = 7.0, 8.5 Hz, 1 H), 8.17 (d, J = 7 Hz, 1 H), 8.24 (d, J = 7.5 Hz, 1 H), 8.43 (d, J = 8.5 Hz, 1 H) ppm. ^{13}C NMR (101 MHz, DMSO-d_6): δ 122.09, 122.13, 126.47, 128.90, 129.52, 129.71, 130.11, 130.59, 131.98, 144.33, 186.64, 186.82 ppm. GC-MS calcd for $C_{12}H_5BrO_2$, [M] m/z = 259.95, found 259.88.

Methyl 4-amino-3-bromobenzoate

Methyl 4-aminobenzoate (0.40 g, 2.6 mmol) and N-bromosuccinimide (NBS) (0.47 g, 2.6 mmol) were added to DMF (5 mL). The reaction mixture was stirred at 0 ºC in a round bottom flask sealed with a rubber septum for 1 h, and then at RT for 24 h. Subsequently, excess H_2O was added. A beige precipitate was obtained by Buchner filtration and the precipitate was washed with excess cold H_2O. The precipitate was further dried in vacuo, yielding methyl 4-amino-3-bromobenzoate (0.57 g, 92%). ^{1}H NMR (400 MHz, DMSO-d6): δ 3.76 (s, 3 H), 6.18 (s, 2 H), 6.80 (d, J = 8.8 Hz, 1 H) 7.64 (dd, J = 8.4, 2.0 Hz, 1 H) 7.89 (d, J = 1.6 Hz, 1 H). ^{13}C NMR (101 MHz, DMSO-d6): δ 51.55, 105.88, 114.11, 117.53, 129.84, 133.73, 150.29, 165.19 ppm.

4.7.3 Synthesis of Ligands (4.1 – 4.3)

(Ar^{NHOH}-$BIAN^{Br}$)$ZnCl_2$ complex

In a flask equipped with a side arm and a reflux condenser, 5-bromoacenaphthylene-1,2-dione (0.11 g, 0.42 mmol) and $ZnCl_2$ (0.10 g, 0.73 mmol) were suspended in a solution of chlorobenzene (2 mL) and methanol (2 mL). The flask was heated to 55 ºC and the mixture was heated for 1 h before 4-aminobenzohydroxamic acid (0.13 g, 0.84 mmol) was added. The suspension was then heated at 65 ºC for 72 h and filtered while hot. The orange solid residue was dried *in vacuo* and was used in the next step without further purification.

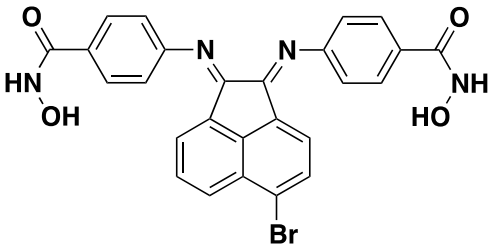

Preparation of Ar^{NHOH}-$BIAN^{Br}$ (4.1) by decoordination of Zn

The orange (Ar^{NHOH}-$BIAN^{Br}$)$ZnCl_2$ was suspended in a solution of excess trisodium ethylenediaminetetraacetate, which was prepared by dissolving ethylenediaminetetraacetic acid (EDTA, 0.913 g, 3.12 mmol) in an aqueous solution (10 mL) of NaOH (0.37 g, 9.4 mmol). The suspension was sonicated until the mixture turned yellow (~ 15 min). The yellow-orange solid was collected by filtration. In a glovebox, the solid (0.16 g) was purified by recrystallization in *N*,*N*-dimethylformamide (DMF)/diethyl ether (Et_2O). The recrystallized solid was dried under reduced pressure to give a yellow-orange solid (0.14 g, 63%). ^{1}H NMR (400 MHz, DMSO-d_6): δ 6.67 (d, J = 8.0 Hz, 1 H), 6.86 (d, J = 7.2 Hz, 1 H), 7.18 (d, J = 8.4 Hz, 4 H), 7.71 (t, J = 7.6 Hz, 1 H), 7.92-7.95 (m, 5 H), 8.13 (d, J = 8.4 Hz, 1 H), 9.05 (s, 2 H), 11.30 (s, 2 H) ppm. ^{13}C NMR (101 MHz, DMSO-d_6): δ 112.63 (2 C), 117.36 (2 C), 123.89, 124.05, 124.24, 127.67, 128.08, 128.28, 128.74 (2 C), 129.64, 130.10, 131.58, 141.49, 153.58 (2 C), 158.93, 159.20, 163.85, 163.92 ppm. HRMS (ESI+, *m/z*) calcd. for $C_{26}H_{18}BrN_4O_4$, $[M+H]^+$ *m/z* = 529.0511, found 529.0510. Anal. Calcd for $C_{26}H_{18}BrN_4O_4 \cdot 2H_2O$ (%): C, 55.23; H, 3.74; N, 9.91. Found: C, 54.94; H, 3.88; N, 9.55.

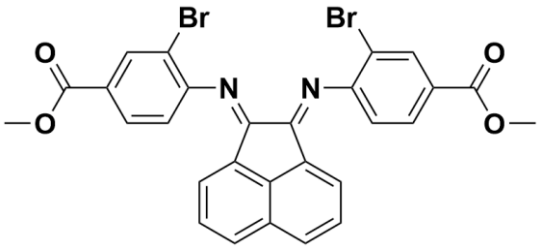

$Ar^{Br,OMe}$-BIAN (4.2)

The ligand **4.2** was synthesized according to a modified procedure reported previously.[17] A 1.0 M toluene solution of $TiCl_4$ (3.0 mL, 3.0 mmol) was added to methyl 4-amino-3-bromobenzoate (0.30 g, 1.3 mmol) and 1,4-diazabicyclo[2.2.2]octane (DABCO, 0.91 g, 8.1 mmol) under N_2. Subsequently, chlorobenzene (10 mL) was added and the reaction mixture was heated for 2 h at 100 ºC. Acenapthylene-1,2-dione (0.10 g, 0.54 mmol) was then added and the reaction mixture was heated for another 24 h. The

precipitate (TiO_2) was removed by hot filtration while the filtrate was collected and dried by rotary evaporation. The residue was recrystallized using tetrahydrofuran (THF)/pentane in a glovebox to afford orange **4.2** (0.20 g, 0.33 mmol, 62% yield). ^{1}H NMR (400 MHz, $CDCl_3$): δ 3.98 (s, 6 H), 6.89 (d, J = 7.1 Hz, 2 H), 7.20 (d, J = 8.2 Hz, 2 H), 7.45 (t, J = 7.7 Hz, 2 H), 7.99 (d, J = 8.3 Hz, 2 H), 8.11 (d, J = 8.1 Hz, 2 H), 8.43 (s, 2 H) ppm. ^{13}C NMR (101 MHz, $CDCl_3$): δ 52.52, 112.27, 119.17, 124.04, 127.77, 128.40, 128.57, 130.11 (2 C), 131.43, 135.14, 141.89, 154.12, 161.88, 165.91 ppm. HRMS (ESI+, *m/z*) calcd. for $C_{28}H_{19}Br_2N_2O_4$, $[M+H]^+$ *m/z* = 604.9712, found 604.9700. Anal. Calcd for $C_{28}H_{18}Br_2N_2O_4 \cdot 2H_2O$ (%): C, 52.36; H, 3.45; N, 4.36. Found: C, 52.02; H, 3.47; N, 4.31.

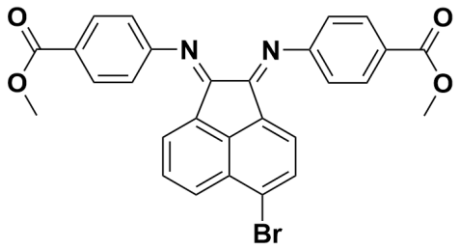

Ar^{OMe}-$BIAN^{Br}$ (4.3)

The ligand **4.3** was synthesized according to the procedure used for **4.2**. The crude product was recrystallized using DCM/hexane to afford brown **4.3** (0.75 g, 1.42 mmol, 70% yield). ^{1}H NMR (400 MHz, $CDCl_3$): δ 3.97 (s, 6 H), 6.69 (d, J = 8.0 Hz, 1 H), 6.91 (d, J = 7.2 Hz, 1 H), 7.16 (dd, J = 3.0, 8.6 Hz, 4 H), 7.50 (t, J = 8.0 Hz, 1 H), 7.64 (d, J = 8.0 Hz, 1 H), 8.15 (d, J = 8.4 Hz, 1 H), 8.18 (dd, J = 3.2, 8.4 Hz, 4 H) ppm. ^{13}C NMR (101 MHz, $CDCl_3$): δ 52.28 (2 C), 118.02 (4 C), 124.77, 125.16, 125.48, 126.73, 126.76, 127.75, 128.46, 129.16, 129.19, 131.14, 131.52, 131.58 (4 C), 142.66, 155.62, 155.66, 160.19, 160.42, 166.94, 166.97 ppm. HRMS (ESI+, m/z) calcd. for $C_{28}H_{20}BrN_2O_4$, $[M+H]^+$ *m/z* = 527.0606, found 527.0610. Anal. Calcd for $C_{28}H_{19}BrN_2O_4 \cdot CH_2Cl_2$ (%): C, 50.78; H, 2.99; N, 4.16. Found: C, 51.09; H, 3.10; N, 3.94.

4.7.4 Synthesis of Cu Complexes (4.4 – 4.6)

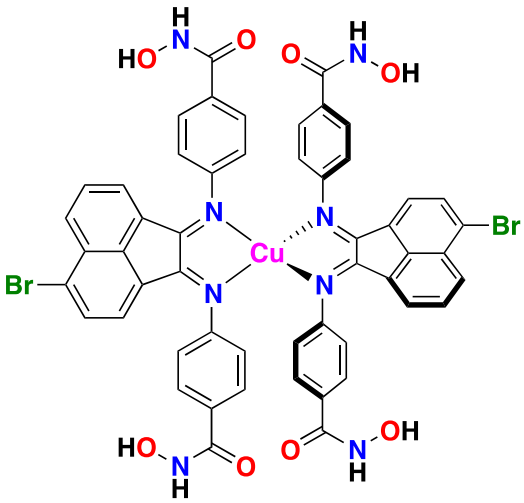

[(Ar^{NHOH}-BIAN^{Br})$_2$Cu^{I}]PF$_6$ (4.4)

In a glovebox, **4.1** (0.090 g, 0.17 mmol) was dissolved in DMF and added to [(CH$_3$CN)$_4$Cu^{I}]PF$_6$ (0.032 g, 0.086 mmol) dissolved in ACN. The reaction was stirred at room temperature (RT) overnight, during which a black solution formed. Upon addition of Et$_2$O, a black solid precipitated, which was collected by filtration. The solid was purified by recrystallization in DMF/Et$_2$O. Black crystalline solid formed and was collected by filtration and dried *in vacuo* to give the product **4.4** (0.075 g, 0.067 mmol, 88% yield). Due to the poor solubility of **4.4**, sufficiently high concentrations of the complex could not be dissolved for the chemical shifts in the ^{13}C NMR spectrum to be located even after a 55 h experiment. ^{1}H NMR (400 MHz, DMSO-d_6): δ 7.03 (d, J = 5.2 Hz, 2 H), 7.22 (d, J = 5.6 Hz, 2 H), 7.31 (s, 8 H), 7.77 (t, J = 7.6 Hz, 2 H), 7.92 – 7.99 (m, 10 H), 8.26 (d, J = 8.0 Hz, 2 H), 9.13 (s, 4 H), 11.34 (s, 4 H) ppm. HRMS (ESI+, m/z) calcd. for C$_{52}$H$_{34}$Br$_2$CuN$_8$O$_8$, [M]$^+$ *m/z* = 1120.0241, found 1120.0259. C$_{52}$H$_{34}$Br$_2$CuN$_8$O$_8$PF$_6$·5H$_2$O (%): C, 46.02; H, 3.27; N, 8.26. Found: C, 46.13; H, 3.61; N, 7.82.

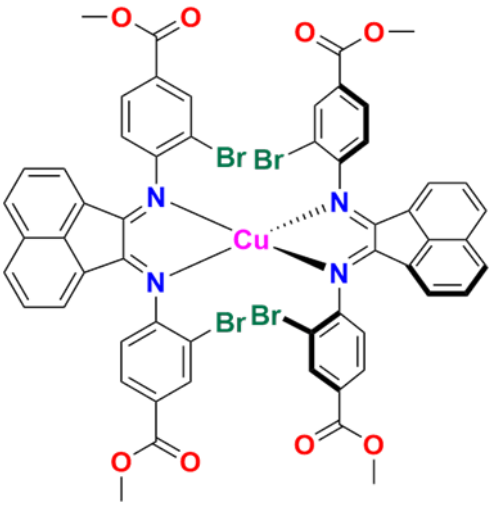

[(Ar^{Br,OMe}-BIAN)$_2$Cu^{I}]PF$_6$ (4.5)

In a glovebox, **4.2** (0.040 g, 0.066 mmol) was dissolved in THF and added to [(CH$_3$CN)$_4$Cu^{I}]PF$_6$ (0.012 g, 0.032 mmol) dissolved in ACN. The reaction was stirred at RT overnight, during which a black solution formed. The solution was dried *in vacuo* and the product was recrystallized in DCM/Et$_2$O to afford **4.5** as a black powder (0.035 g, 0.027 mmol, 83% yield). ^{1}H NMR (400 MHz, CDCl$_3$): δ 4.02 (s, 12 H), 6.86 (s, 4 H), 7.36 (s, 4 H), 7.50 (t, J = 4.0 Hz, 4 H), 8.11 (d, J = 7.6 Hz, 8 H), 8.38 (s, 4 H) ppm. ^{13}C NMR (101 MHz, CDCl$_3$): δ 52.90 (4 C), 114.88 (4 C), 122.35 (4 C), 125.30 (4 C), 126.41 (4 C), 129.15 (4 C), 130.38 (2 C), 130.72 (4 C), 131.34 (4 C), 132.23 (4 C), 135.28 (4 C), 149.87 (2 C), 165.27 (8 C), 165.89 (4 C) ppm. HRMS (ESI+, m/z) calcd. for C$_{56}$H$_{36}$Br$_4$CuN$_4$O$_8$, [M]$^+$ *m/z* = 1271.8641, found 1271.8624. Anal. Calcd for C$_{56}$H$_{36}$Br$_4$CuN$_4$O$_8$PF$_6$·H$_2$O (%): C, 46.74; H, 2.66; N, 3.89; found: C, 46.33; H, 2.97; N, 3.87.

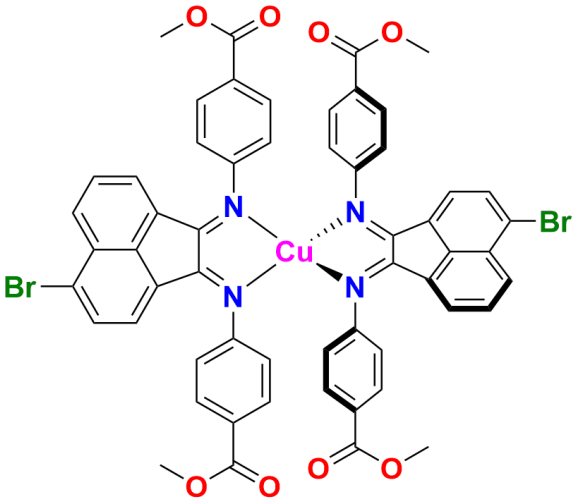

[(Ar^{OMe}-$BIAN^{Br}$)$_2$$Cu^{I}$]$PF_6$ (4.6)

In a glovebox, **4.3** (0.062 g, 0.12 mmol) was dissolved in DCM and added to [(CH_3CN)$_4$$Cu^{I}$]$PF_6$ (0.022 g, 0.059 mmol) suspended in DCM. The reaction mixture was stirred at RT overnight, during which a black solution formed. The solution was dried *in vacuo* and the product was recrystallized in DCM/Et_2O to afford **4.6** as a black powder (0.052 g, 0.046 mmol, 79% yield). ^{1}H NMR (400 MHz, $CDCl_3$): δ 3.97 (s, 12 H), 7.01 (d, J = 7.6 Hz, 2 H), 7.23 (d, J = 8.4 Hz, 10 H), 7.62 (t, J = 8.0 Hz, 2 H), 7.77 (d, J = 7.6 Hz, 2 H), 8.23 (dd, J = 2.4, 8.4 Hz, 8 H), 8.33 (d, J = 8.4 Hz, 2 H) ppm. ^{13}C NMR (101 MHz, $CDCl_3$): δ 52.83 (4 C), 120.82 (8 C), 125.69 (2 C), 125.93 (2 C), 126.46 (2 C), 126.55 (4 C), 128.59 (2 C), 130.27 (2 C), 130.42 (2 C), 131.60 (2 C), 131.73 (2 C), 132.32 (8 C), 132.82 (2 C), 144.01 (2 C), 155.20 (4 C), 164.36 (2 C), 164.77 (2 C), 166.27 (4 C) ppm. HRMS (ESI+, m/z) calcd. for $C_{56}H_{38}Br_2CuN_4O_8$, $[M]^+$ *m/z* = 1116.0431, found 1116.0455. Anal. Calcd for $C_{56}H_{38}Br_2CuN_4O_8PF_6 \cdot H_2O$ (%): C, 52.50; H, 3.15; N, 4.37; found: C, 52.15; H, 3.31; N, 4.60.

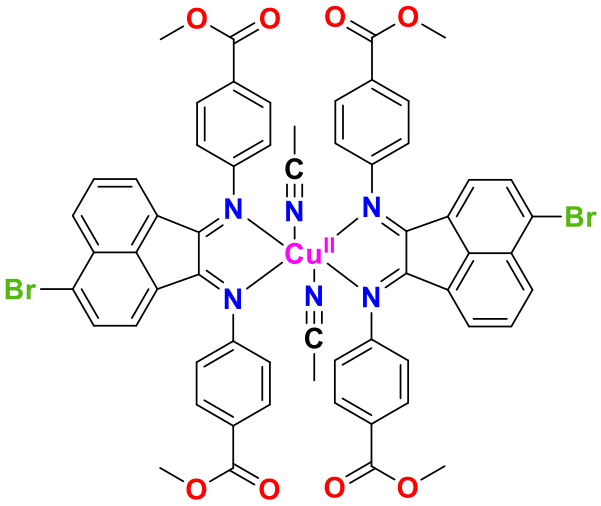

[(Ar^{OMe}-$BIAN^{Br}$)$_2$(CH_3CN)$_2$$Cu^{II}$]($PF_6$)($SbF_6$) (4.14)

In a glovebox, **4.6** (15 mg, 0.012 mmol) was dissolved in DCM. Upon addition of tris(2,4-dibromophenyl)aminium hexafluoroantimonate (11 mg, 0.012 mmol) at RT, the dark purple solution turned brown. The solution was dried *in vacuo* and the product was recrystallized in ACN/Et_2O to afford **4.14** as orange crystals (15 mg, 0.010 mmol, 81% yield). However, the fully refined crystal structure of **4.14** could not be obtained because of the disorder in the location of the Br atoms and the solvent molecules present. Anal. Calcd for $C_{60}H_{44}Br_2CuN_6O_8PSbF_{12}$ (%): C, 45.58; H, 2.81; N, 5.32; found: C, 45.05; H, 2.41; N, 4.70.

4.8 General Procedure for ATRA Reaction Catalyzed by 4.6

A solution of alkene (0.13 mmol), CBr_4 (0.13 mmol), and **4.6** (0.60 mol%) in DCM (1.0 mL) was degassed using two freeze-pump-thaw cycles, refilled with N_2, and irradiated with two white LEDs for 24 h. The reaction mixture was concentrated in vacuo. Some of these organic compounds have been previously reported and we have verified the identity of our products by comparing our spectroscopic data with those from the references.

(1,3,3,3-tetrabromopropyl)benzene[15d]

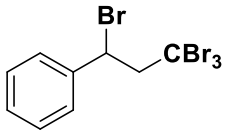

Colourless oil, 74% yield.

The product was isolated after purification on silica with hexanes as the eluent and the thin-layer chromatography (TLC) spot was monitored with UV irradiation. ^{1}H NMR (400 MHz, $CDCl_3$): δ 4.06 (dd, J = 7.7, 15.6 Hz, 1 H), 4.13 (dd, J = 4.2, 15.6 Hz, 1 H), 5.33 (dd, J = 4.1, 7.7 Hz, 1 H), 7.41 – 7.28 (m, 3 H), 7.53 – 7.46 (m, 2 H). ^{13}C NMR (101 MHz, $CDCl_3$): δ 35.15, 50.19, 66.60, 128.30, 129.03 (2 C), 129.09 (2 C), 140.93. HRMS calcd. for $C_9H_9Br_4$, $[M+H]^+$ *m/z* =435.7319, found 435.7319.

1-chloro-4-(1,3,3,3-tetrabromopropyl)benzene

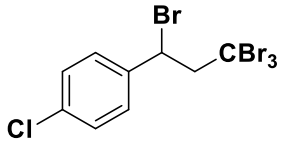

White solid, 75% yield.

The product was isolated after purification on silica with hexanes as the eluent and the TLC spot was monitored with UV irradiation, ^{1}H NMR (400 MHz, $CDCl_3$): δ 4.01 (dd, J = 15.6, 8.4 Hz, 1 H), 4.10 (dd, J = 15.6, 3.8 Hz, 1 H), 5.31 (dd, J = 8.2, 3.8 Hz, 1 H), 7.34 (d, J = 8.4 Hz, 2 H), 7.43 (d, J = 8.4 Hz, 2 H). ^{13}C NMR (101 MHz, $CDCl_3$): δ 34.78, 49.04, 66.39, 129.23 (2 C), 129.69 (2 C), 134.91, 139.33. HRMS calcd. for $C_9H_8Br_4Cl$, $[M+H]^+$ *m/z* =470.6929, found 470.7015.

1-cyano-4-(1,3,3,3-tetrabromopropyl)benzene[32a]

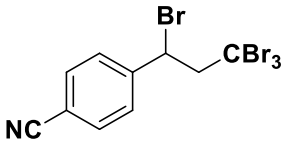

Yellow oil, 44% yield.

The product was isolated after purification on silica with the eluent system ethyl acetate:hexanes in a ratio of 9:1 and the TLC spot was monitored with UV irradiation, ^{1}H NMR (400 MHz, $CDCl_3$): δ 4.02 (dd, J = 15.6, 8.4 Hz, 1 H), 4.12 (dd, J = 15.6, 4.0 Hz, 1 H), 5.32 (dd, J = 8.4, 3.6 Hz, 1 H), 7.61 (d, J = 8.4 Hz, 2 H), 7.67 (d, J = 8.4 Hz, 2 H). ^{13}C NMR (101 MHz, $CDCl_3$): δ 34.23, 48.03, 66.09, 112.92, 118.31, 129.17 (2 C), 132.82 (2 C), 145.78. HRMS calcd. for $C_{10}H_8Br_4N$, $[M+H]^+$ *m/z* =461.7271, found 461.7346.

1-methyl-4-(1,3,3,3-tetrabromopropyl)benzene[15a]

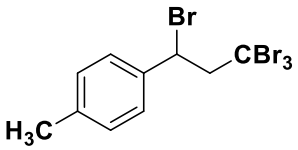

Yellow oil, 44% yield.

The NMR of the crude reaction mixture was recorded after the reaction since the compound hydrolyzed after purification on silica with hexanes as the eluent. ^{1}H NMR (400 MHz, $CDCl_3$): δ 2.35 (s, 3 H), 4.05 (dd, J = 15.6, 7.6 Hz, 1 H), 4.11 (dd, J = 15.4, 4.2 Hz, 1 H), 5.32 (dd, J = 7.8, 4.2 Hz, 1 H), 7.17 (d, J = 8.0 Hz, 2 H), 7.38 (d, J = 8.0 Hz, 2 H). ^{13}C NMR (101 MHz, $CDCl_3$): δ 21.41, 35.32, 50.41, 66.61, 128.18 (2 C), 129.70 (2 C), 138.02, 139.13. HRMS calcd for $C_{10}H_{11}Br_4$, $[M+H]^+$ *m/z* =450.7475, found 450.7550.

2-(1-bromo-3,3,3-tribromopropyl)-naphthalene

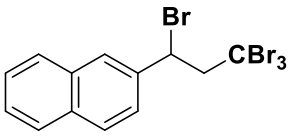

32% yield.

The ^{1}H NMR of the crude reaction mixture was recorded after the reaction since the compound hydrolyzed after purification on silica with hexanes as the eluent.

3,3,3-tribromo-1-(naphthalen-2-yl)propan-1-ol

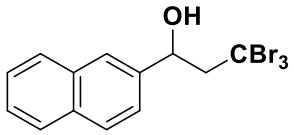

Colourless oil.

The NMR of the hydrolyzed product was isolated after purification on silica with hexanes as the eluent. ^{1}H NMR (400 MHz, $CDCl_3$): δ 2.71 (br s, 1 H), 3.60 (dd, J = 15.5, 2.6 Hz, 1 H), 3.68 (dd, J = 15.6, 7.1 Hz, 1 H), 5.38 (dd, J = 7.1, 2.4 Hz, 1 H), 7.59 – 7.47 (m, 3 H), 7.93 – 7.86 (m, 4 H). ^{13}C NMR (101 MHz, $CDCl_3$): δ 37.14, 67.61, 74.57, 123.84, 124.95, 126.40, 126.61, 127.90, 128.21, 128.94, 133.28, 133.46, 140.05.

4.9 References

(1) Gust, D.; Moore, T. A.; Moore, A. L., *Acc. Chem. Res.* **2009**, *42*, 1890-1898.

(2) Kee, J. W.; Ng, Y. Y.; Kulkarni, S. A.; Muduli, S. K.; Xu, K.; Ganguly, R.; Lu, Y.; Hirao, H.; Soo, H. S., *Inorg. Chem. Front.* **2016**, *3*, 651-662.

(3) (a) Schultz, D. M.; Yoon, T. P., *Science* **2014**, *343*, 985; (b) Prier, C. K.; Rankic, D. A.; MacMillan, D. W., *Chem. Rev.* **2013**, *113*, 5322-5363; (c) Stevenson, S. M.; Higgins, R. F.; Shores, M. P.; Ferreira, E. M., *Chem. Sci.* **2017**, *8*, 654-660; (d) Hsu, Y. C.; Wang, V. C.; Au-Yeung, K. C.; Tsai, C. Y.; Chang, C. C.; Lin, B. C.; Chan, Y. T.; Hsu, C. P.; Yap, G. P. A.; Jurca, T.; Ong, T. G., *Angew. Chem. Int. Ed.* **2018**, *57*, 4622-4626.

(4) Pashaei, B.; Shahroosvand, H.; Graetzel, M.; Nazeeruddin, M. K., *Chem. Rev.* **2016**, *116*, 9485-9564.

(5) (a) Yin, J.-F.; Velayudham, M.; Bhattacharya, D.; Lin, H.-C.; Lu, K.-L., *Coord. Chem. Rev.* **2012**, *256*, 3008-3035; (b) Henwood, A. F.; Zysman-Colman, E., *Chem. Commun.* **2017**, *53*, 807-826; (c) Yam, V. W.; Au, V. K.; Leung, S. Y., *Chem. Rev.* **2015**, *115*, 7589-7728; (d) Yu, S.; Zeng, Y.; Chen, J.; Yu, T.; Zhang, X.; Yang, G.; Li, Y., *RSC Adv.* **2015**, *5*, 70640-70648.

(6) (a) Mathew, S.; Yella, A.; Gao, P.; Humphry-Baker, R.; Curchod, B. F.; Ashari-Astani, N.; Tavernelli, I.; Rothlisberger, U.; Nazeeruddin, M. K.; Gratzel, M., *Nat. Chem.* **2014**, *6*, 242-247; (b) Salvatori, P.; Amat, A.; Pastore, M.; Vitillaro, G.; Sudhakar, K.; Giribabu, L.; Soujanya, Y.; De Angelis, F., *Comput. Theor. Chem.* **2014**, *1030*, 59-66; (c) Chen, Z.; Lohr, A.; Saha-Moller, C. R.; Wurthner, F., *Chem. Soc. Rev.* **2009**, *38*, 564-584.

(7) (a) Romero, N. A.; Nicewicz, D. A., *Chem. Rev.* **2016**, *116*, 10075-10166; (b) Miller, A. J.; Dempsey, J. L.; Peters, J. C., *Inorg. Chem.* **2007**, *46*, 7244-7246; (c) Zhang, Y.; Petersen, J. L.; Milsmann, C., *J. Am. Chem. Soc.* **2016**, *138*, 13115-13118.

(8) (a) Dokic, M.; Soo, H. S., *Chem. Commun.* **2018**, *54*, 6554-6572; (b) Armaroli, N., *Chem. Soc. Rev.* **2001**, *30*, 113-124; (c) Lazorski, M. S.; Castellano, F. N., *Polyhedron* **2014**, *82*, 57-70.

(9) Khnayzer, R. S.; McCusker, C. E.; Olaiya, B. S.; Castellano, F. N., *J. Am. Chem. Soc.* **2013**, *135*, 14068-14070.

(10) Housecroft, C. E.; Constable, E. C., *Chem. Soc. Rev.* **2015**, *44*, 8386-8398.

(11) (a) Fedushkin, I. L.; Skatova, A. A.; Cherkasov, V. K.; Chudakova, V. A.; Dechert, S.; Hummert, M.; Schumann, H., *Chem. Eur. J.* **2003**, *9*, 5778-5783; (b) Hill, N. J.; Vargas-Baca, I.; Cowley, A. H., *Dalton Trans.* **2009**, 240-253.

(12) Gasperini, M.; Ragaini, F.; Cenini, S., *Organometallics* **2002**, *21*, 2950-2957.

(13) (a) Kern, T.; Monkowius, U.; Zabel, M.; Knor, G., *Eur. J. Inorg. Chem.* **2010**, 4148-4156; (b) Rosa, V.; Santos, C. I. M.; Welter, R.; Aullon, G.; Lodeiro, C.; Aviles, T., *Inorg. Chem.* **2010**, *49*, 8699-8708; (c) Papanikolaou, P.; Akrivos, P. D.; Czapik, A.; Wicher, B.; Gdaniec, M.; Tkachenko, N., *Eur. J. Inorg. Chem.* **2013**, 2418-2431.

(14) (a) Wang, J.; Ganguly, R.; Yongxin, L.; Diaz, J.; Soo, H. S.; Garcia, F., *Dalton Trans.* **2016**, *45*, 7941-7946; (b) Wang, J.; Ganguly, R.; Yongxin, L.; Diaz, J.; Soo, H. S.; Garcia, F., *Inorg. Chem.* **2017**, *56*, 7811-7820; (c) Hasan, K.; Wang, J.; Pal, A. K.; Hierlinger, C.; Guerchais, V.; Sen Soo, H.; Garcia, F.; Zysman-Colman, E., *Sci. Rep.* **2017**, *7*, 15520.

(15) (a) Chen, B.; Fang, C.; Liu, P.; Ready, J. M., *Angew. Chem. Int. Ed.* **2017**, *56*, 8780-8784; (b) Rawner, T.; Lutsker, E.; Kaiser, C. A.; Reiser, O., *ACS Catal.* **2018**, *8*, 3950-3956; (c) Knorn, M.; Rawner, T.; Czerwieniec, R.; Reiser, O., *ACS Catal.* **2015**, *5*, 5186-5193; (d) Pirtsch, M.; Paria, S.; Matsuno, T.; Isobe, H.; Reiser, O., *Chem. Eur. J.* **2012**, *18*, 7336-7340.

(16) (a) Gaynor, D.; Starikova, Z. A.; Haase, W.; Nolan, K. B., *Dalton Trans.* **2001**, 1578-1581; (b) Grant, C. D.; Kang, S. O.; Hay, B. P., *J. Org. Chem.* **2013**, *78*, 7735-7740.

(17) Li, L.; Jeon, M.; Kim, S. Y., *J. Mol. Catal. A: Chem.* **2009**, *303*, 110-116.

(18) Li, L.; Lopes, P. S.; Rosa, V.; Figueira, C. A.; Lemos, M. A. N. D. A.; Duarte, M. T.; Aviles, T.; Gomes, P. T., *Dalton Trans.* **2012**, *41*, 5144-5154.

(19) Papanikolaou, P. A.; Tkachenko, N. V., *Phys. Chem. Chem. Phys.* **2013**, *15*, 13128-13136.
(20) Caspar, J. V.; Meyer, T. J., *J. Am. Chem. Soc.* **1983**, *105*, 5583-5590.
(21) (a) Everly, R. M.; McMillin, D. R., *Photochem. Photobiol.* **1989**, *50*, 711-716; (b) Laviecambot, A.; Cantuel, M.; Leydet, Y.; Jonusauskas, G.; Bassani, D.; McClenaghan, N., *Coord. Chem. Rev.* **2008**, *252*, 2572-2584; (c) Penfold, T. J.; Karlsson, S.; Capano, G.; Lima, F. A.; Rittmann, J.; Reinhard, M.; Rittmann-Frank, M. H.; Braem, O.; Baranoff, E.; Abela, R.; Tavernelli, I.; Rothlisberger, U.; Milne, C. J.; Chergui, M., *J. Phys. Chem. A* **2013**, *117*, 4591-4601.
(22) Garakyaraghi, S.; Danilov, E. O.; McCusker, C. E.; Castellano, F. N., *J. Phys. Chem. A* **2015**, *119*, 3181-3193.
(23) (a) Kern, T.; Monkowius, U.; Zabel, M.; Knör, G., *Inorg. Chim. Acta* **2011**, *374*, 632-636; (b) Evans, D. A.; Lee, L. M.; Vargas-Baca, I.; Cowley, A. H., *Organometallics* **2015**, *34*, 2422-2428.
(24) (a) Casadonte, D. J.; McMillin, D. R., *J. Am. Chem. Soc.* **1987**, *109*, 331-337; (b) Coppens, P.; Sokolow, J.; Trzop, E.; Makal, A.; Chen, Y., *J. Phys. Chem. Lett.* **2013**, *4*, 579-582.
(25) Chabera, P.; Liu, Y.; Prakash, O.; Thyrhaug, E.; Nahhas, A. E.; Honarfar, A.; Essen, S.; Fredin, L. A.; Harlang, T. C.; Kjaer, K. S.; Handrup, K.; Ericson, F.; Tatsuno, H.; Morgan, K.; Schnadt, J.; Haggstrom, L.; Ericsson, T.; Sobkowiak, A.; Lidin, S.; Huang, P.; Styring, S.; Uhlig, J.; Bendix, J.; Lomoth, R.; Sundstrom, V.; Persson, P.; Warnmark, K., *Nature* **2017**, *543*, 695-699.
(26) (a) Duchanois, T.; Etienne, T.; Cebrián, C.; Liu, L.; Monari, A.; Beley, M.; Assfeld, X.; Haacke, S.; Gros, P. C., *Eur. J. Inorg. Chem.* **2015**, *2015*, 2469-2477; (b) Harlang, T. C.; Liu, Y.; Gordivska, O.; Fredin, L. A.; Ponseca, C. S., Jr.; Huang, P.; Chabera, P.; Kjaer, K. S.; Mateos, H.; Uhlig, J.; Lomoth, R.; Wallenberg, R.; Styring, S.; Persson, P.; Sundstrom, V.; Warnmark, K., *Nat. Chem.* **2015**, *7*, 883-889; (c) Fatur, S. M.; Shepard, S. G.; Higgins, R. F.; Shores, M. P.; Damrauer, N. H., *J. Am. Chem. Soc.* **2017**, *139*, 4493-4505.
(27) (a) McCusker, C. E.; Castellano, F. N., *Inorg. Chem.* **2013**, *52*, 8114-8120; (b) Garakyaraghi, S.; Crapps, P. D.; McCusker, C. E.; Castellano, F. N., *Inorg. Chem.* **2016**, *55*, 10628-10636.
(28) Kharasch, M. S.; Jensen, E. V.; Urry, W. H., *Science* **1945**, *102*, 128.

(29) Beatty, J. W.; Douglas, J. J.; Cole, K. P.; Stephenson, C. R., *Nat. Commun.* **2015**, *6*, 7919.
(30) (a) Furst, L.; Matsuura, B. S.; Narayanam, J. M.; Tucker, J. W.; Stephenson, C. R., *Org. Lett.* **2010**, *12*, 3104-3107; (b) Huo, H.; Wang, C.; Harms, K.; Meggers, E., *J. Am. Chem. Soc.* **2015**, *137*, 9551-9554.
(31) Zoski, C. G., *Handbook of Electrochemistry*. Elsevier: 2007.
(32) (a) Song, C.-x.; Chen, P.; Tang, Y., *RSC Adv.* **2017**, *7*, 11233-11243; (b) Matsuo, K.; Yamaguchi, E.; Itoh, A., *Asian J. Org. Chem* **2018**, *7*.
(33) Olshin, P. K.; Myasnikova, O. S.; Kashina, M. V.; Gorbunov, A. O.; Bogachev, N. A.; Kompanets, V. O.; Chekalin, S. V.; Pulkin, S. A.; Kochemirovsky, V. A.; Skripkin, M. Y.; Mereshchenko, A. S., *Chem. Phys.* **2018**, *503*, 14-19.

Chapter 5

Future Outlook and Conclusion

5.1 Foreword

Chapters 2 – 4 demonstrate the use of Ar-BIAN Cu^{I} complexes in different applications of artificial photosynthetic system such as in DSSCs or as catalysts for photoredox reactions. However, due to the short photoexcited lifetimes and absence of emission signals (except for complex **4.6**) of all the synthesized Ar-BIAN Cu^{I} complexes, we are keen to investigate other ligand systems to develop more effective Cu^{I} photosensitizers. Therefore, this chapter will briefly describe the future outlook as well as conclude the thesis.

5.2 Future Outlook

As we attempt to shift away from the use of Ar-BIAN as a ligand due to its lack of emission, we are interested in other ligand systems that have similar ease of synthesis and are able to produce luminescent complexes. Cu complexes based on NHC ligands have been reported[1] to be luminescent because of their strong bonds with the metal center. Therefore, a carbene ligand system is of interest to us. Mentioned briefly in Chapter 1, MIC is a relatively new, stable *abnormal* carbene that has high tunability in its substituents and functionalities to adjust the electronic properties of the MIC complexes formed. For example, the installation of electron-withdrawing groups stabilizes MICs, while electron-donating substituents destabilize the free ligands, preventing their isolation.[2] With its strongly σ-donating properties and versatility in its synthesis, numerous transition metal complexes bearing MIC ligands have been developed.[3]

Most of the MIC complexes synthesized are used in homogeneous catalysis while less attention has been paid to the study of their photophysical properties and the use of such complexes as triplet emitters.[4] Hence, more research is required in this field since MIC complexes have shown promising results in its emission properties such as the phosphorescent Pt complexes that have emission quantum yields of 61 – 72% and impressive lifetimes of up to 17.9 ms.[4] At the same time, Ir complexes with 1,2,3-triazoles as ligands are candidates of phosphorescent dopants in organic light-emitting diodes (OLEDs), light-emitting electrochemical cells (LECs), and electronic display devices.[3b] Other transition metals consisting of the MIC ligand system have also been reported[3b, 5] to give exciting photophysical properties. Therefore, our future prospective includes the development of new MIC Cu^{I} complexes to investigate their photophysical activities and explore their possible applications.

5.3 Conclusion

In summary, this thesis has provided a study of the development of new Cu^{I}-based photosensitizers supported by Ar-BIAN ligands comprising earth-abundant elements. The synthesis and full characterization of the new Ar-BIAN ligands and their corresponding Cu^{I} complexes were presented. A systematic investigation of their photochemical and photophysical properties was performed. Following on, their applications in DSSCs and as a photocatalyst for ATRA reaction were also discussed. The first series of Ar-BIAN Cu^{I} complexes we synthesized have been presented in Chapter 2. One of the Cu^{I} complexes (**2.4**) showed a unique crystal structure, which has a rhombically distorted square planar geometry around the metal center due to its ortho-iodoarylimino moieties. The DFT calculations that we obtained provided a comprehensive study of the unexpected coordination sphere observed. A comparison of the UV-visible absorption spectra and diffuse reflectance spectra revealed that the complex adopts different geometries when in solution and in the solid-state. The feasibility of these new Cu complexes as photosensitizers in DSSCs was investigated. The *J-V* curves gave low, but unoptimized efficiencies due to the less-than-optimal alignments of the molecular orbitals of the complexes with the other components of the DSSC.

Subsequently, another series of Ar-BIAN Cu^{I} complexes were synthesized after modifying some of the substituents on the ligands. Detailed electrochemical and spectroscopic studies were completed. In addition to the quasi-reversible redox waves observed in its CV, complex **4.6** exhibited an emission signal at 510 nm that has a photoexcited lifetime on the order of nanoseconds. The luminescent **4.6** was shown to be an effective photocatalyst in the ATRA reaction between styrenes and CBr_4 under ambient conditions. We attempt to rationalize the mechanism of the photoredox reaction by identifying the intermediate *via* spectroelectrochemistry and independently oxidizing **4.6** to obtain its UV-visible absorption spectrum. These experiments validated our hypothesis that the intermediate may be a Cu^{II} complex with CBr_3 or Br attached.

In the future, we are interested in the similarly versatile MIC ligand system. Its strongly σ-donating and moderate π-accepting nature makes it a potential candidate for homogeneous catalysis and as luminophores. Future work includes the synthesis and complete characterization of the new carbene complexes to establish their chemical and redox properties. In-depth photophysical analyses of the complexes in solution, thin film

and solid-state will be necessary to determine their feasibility as efficient luminophores before incorporating the complexes in photoredox catalysis reactions or in light-emitting devices.

In conclusion, we have successfully synthesized a series of Ar-BIAN ligands that can be easily assembled to form the corresponding Cu^{I} complexes with varying photophysical properties. In the future, we hope to further optimize the ligand system to improve the photochemical and photophysical features of the Cu^{I} complexes.

5.4 References

(1) Matsumoto, K.; Matsumoto, N.; Ishii, A.; Tsukuda, T.; Hasegawa, M.; Tsubomura, T., *Dalton Trans.* **2009**, 6795-6801.

(2) Ung, G.; Bertrand, G., *Chem. Eur. J.* **2011**, *17*, 8269-8272.

(3) (a) Arnold, P. L.; Pearson, S., *Coord. Chem. Rev.* **2007**, *251*, 596-609; (b) Scattergood, P. A.; Sinopoli, A.; Elliott, P. I. P., *Coord. Chem. Rev.* **2017**, *350*, 136-154.

(4) Soellner, J.; Tenne, M.; Wagenblast, G.; Strassner, T., *Chem. Eur. J.* **2016**, *22*, 9914-9918.

(5) Hohloch, S.; Scheiffele, D.; Sarkar, B., *Eur. J. Inorg. Chem.* **2013**, *2013*, 3956-3965.

Publications

1. Jun Wei Kee, Yik Yie Ng, Sneha Kulkarni, Subas Muduli, Kai Xu, Rakesh Ganguly, Yunpeng Lu, Hajime Hirao, and Han Sen Soo, Development of Bis(arylimino)acenaphthene (BIAN) Copper Complexes as Visible Light Harvesters for Potential Photovoltaic Applications. *Inorg. Chem. Front.*, **2016**, *3*, 651-662.

2. Yik Yie Ng, Lisa Jiaying Tan, Shue Mei Ng, Yoke Tin Chai, Rakesh Ganguly, Yonghua Du, Edwin Kok Lee Yeow, and Han Sen Soo, Spectroscopic Characterization and Mechanistic Studies on Visible Light Photoredox Carbon-Carbon Bond Formation by Bis(Arylimino)Acenaphthene Copper Photosensitizers. *ACS Catal.* **2018**, *8*, 11277-11286.

3. Xian Liang Ho, Haiyan Shao, Yik Yie Ng, Rakesh Ganguly, Yunpeng Lu, Han Sen Soo, Visible Light Driven Hydrogen Evolution by Molecular Nickel Catalysts with Time-Resolved Spectroscopic and DFT Insights. *Inorg. Chem.* **2018**, DOI: 10.1021/acs.inorgchem.8b03003.

Appendix

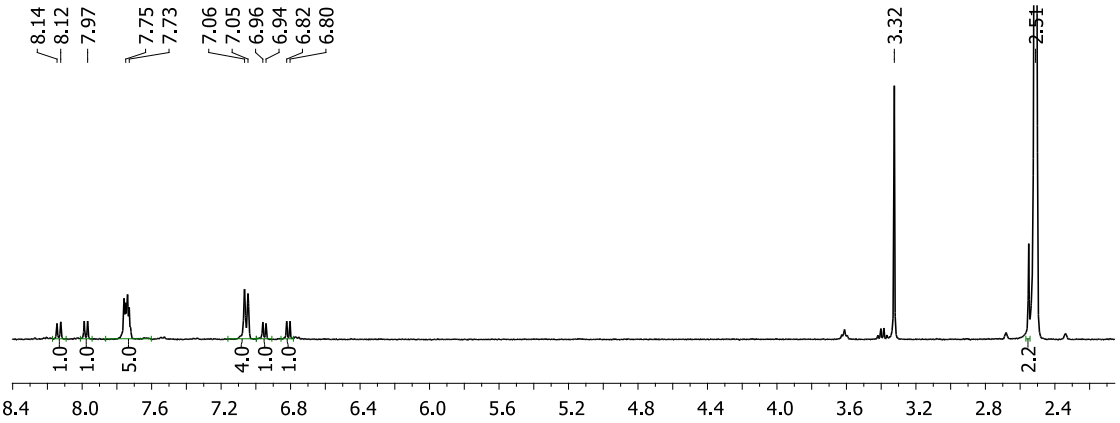

Figure A.1 The ^{1}H NMR spectrum of **2.1** recorded in DMSO-d_6. The solvent residual peak is at 2.50 ppm (quintet), while the peak at 3.31 ppm is due to water in the NMR solvent.

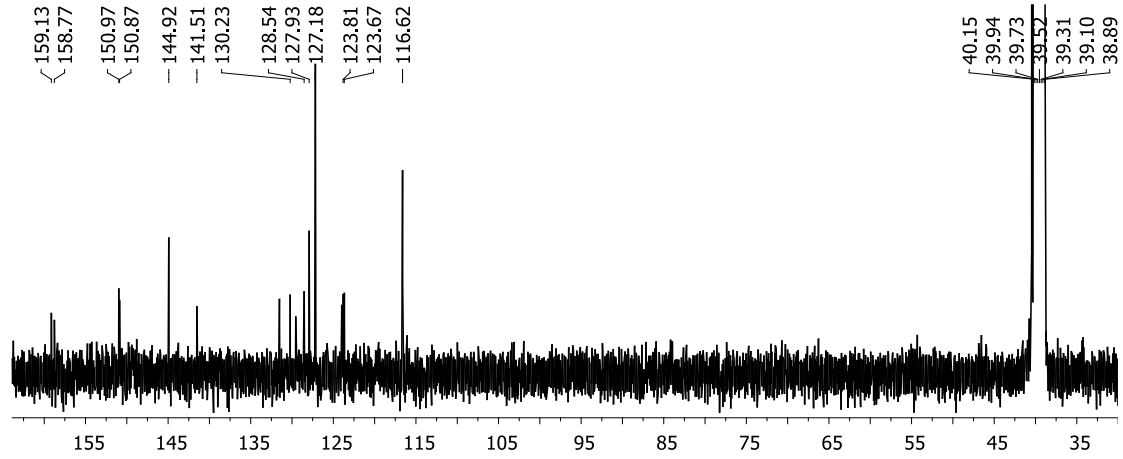

Figure A.2 The ^{13}C NMR spectrum of **2.1** recorded in DMSO-d_6. The solvent residual peak is at 39.5 ppm (septet).

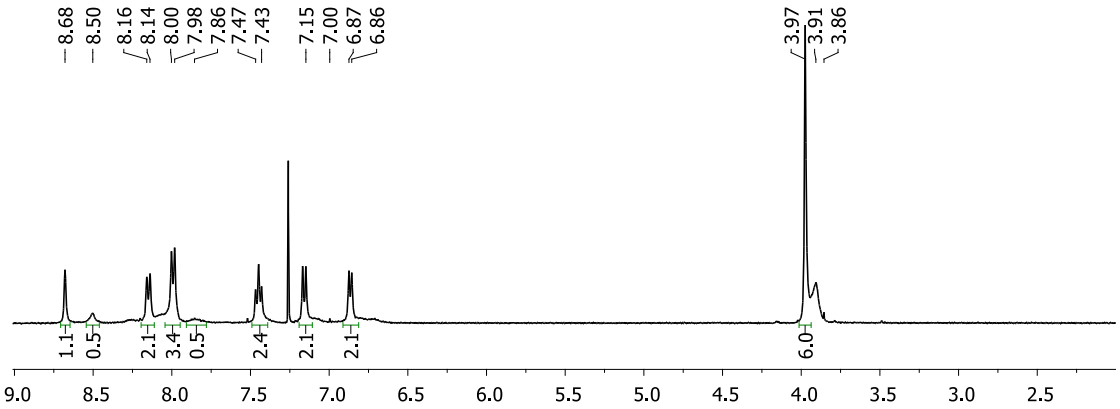

Figure A.3 The ^{1}H NMR spectrum of **2.2** recorded in $CDCl_3$. The solvent residual peak is at 7.26 ppm (singlet).

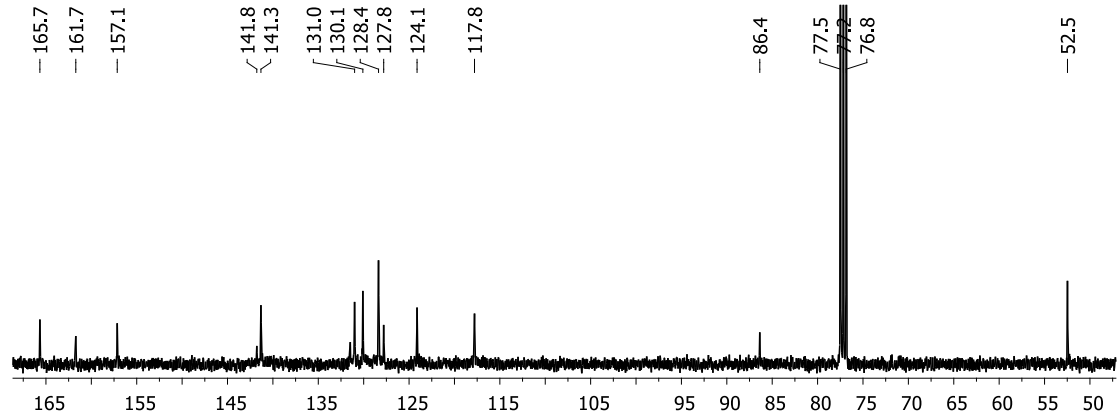

Figure A.4 The ^{13}C NMR spectrum of **2.2** recorded in $CDCl_3$. The solvent residual peak is at 77.2 ppm (triplet).

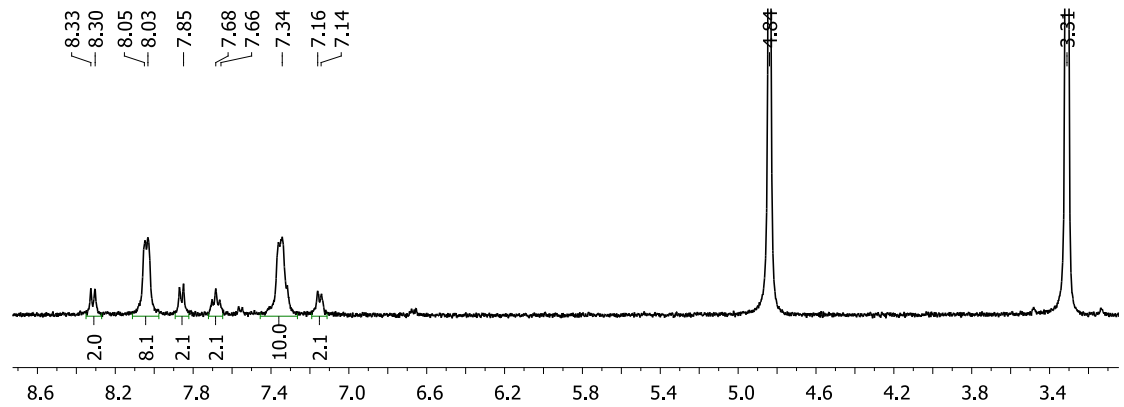

Figure A.5 The ^{1}H NMR spectrum of **2.3** recorded in MeOD-d_4. The solvent residual peak is at 3.31 ppm (quintet), while the peak at 4.84 ppm is due to water in the NMR solvent.

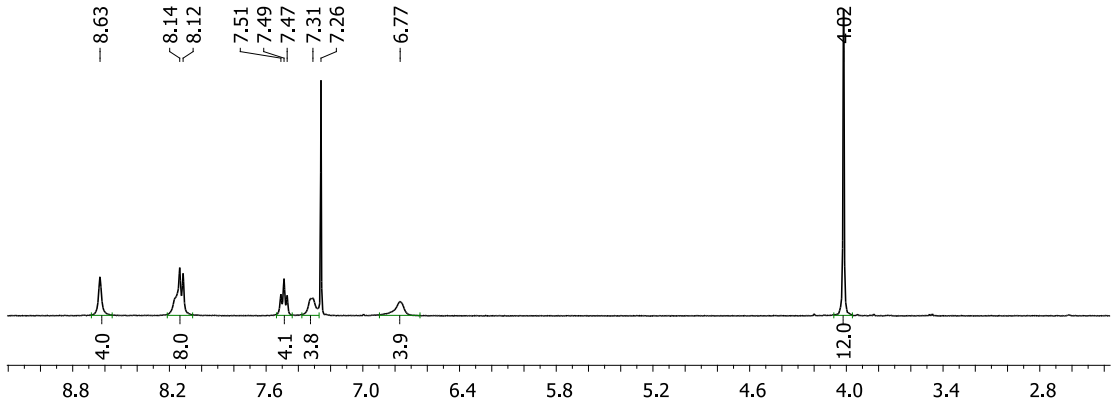

Figure A.6 The ^{1}H NMR spectrum of **2.4** recorded in $CDCl_3$. The solvent residual peak is at 7.26 ppm (singlet).

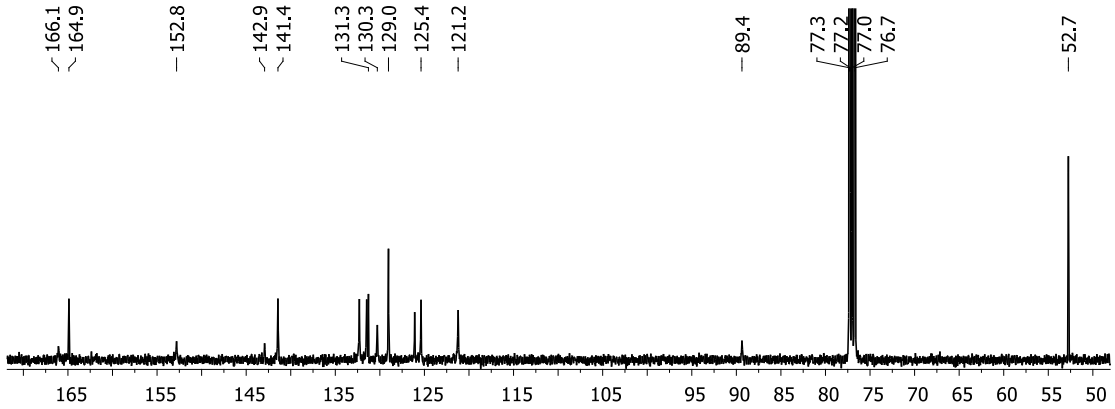

Figure A.7 The ^{13}C NMR spectrum of **2.4** recorded in $CDCl_3$. The solvent residual peak is at 77.2 ppm (triplet).

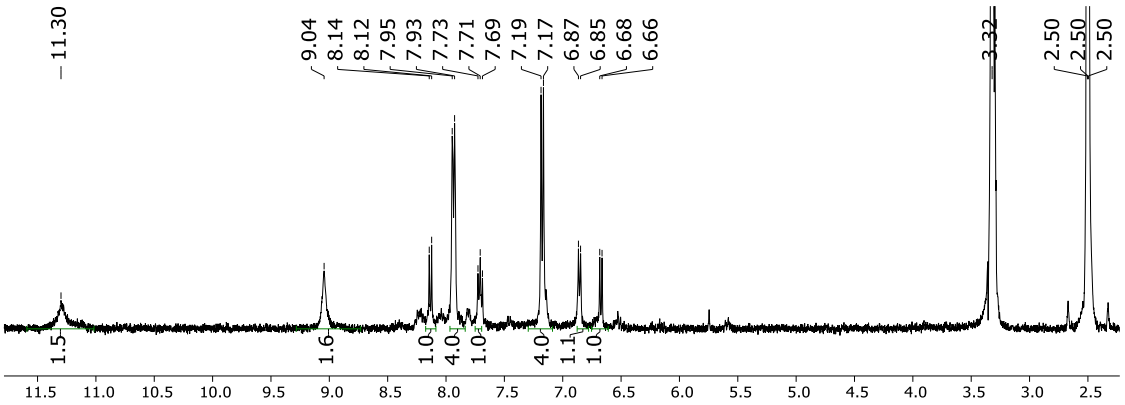

Figure A.8 The ^{1}H NMR spectrum of **4.1** recorded in DMSO-d_6. The solvent residual peak is at 2.50 ppm (quintet), while the peak at 3.32 ppm is due to water in the NMR solvent.

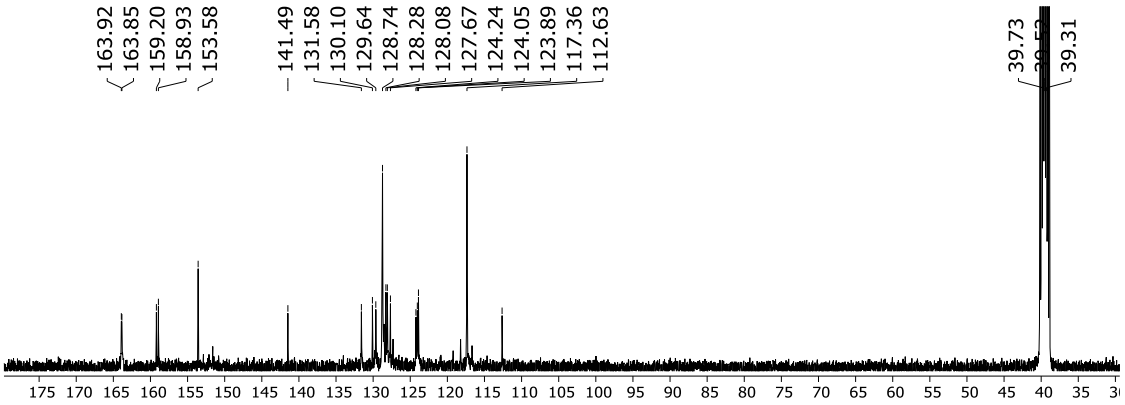

Figure A.8 The ^{13}C NMR spectrum of **4.1** recorded in DMSO-d_6. The solvent residual peak is at 39.5 ppm (septet).

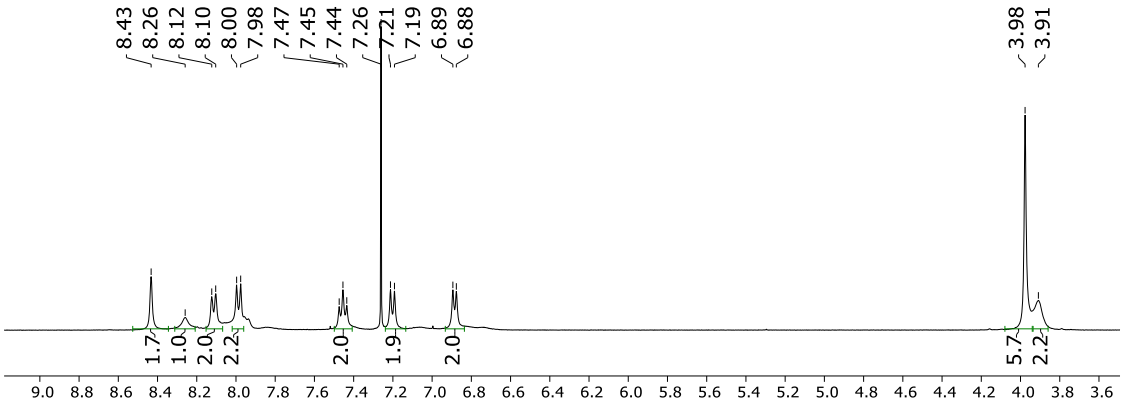

Figure A.9 The ^{1}H NMR spectrum of **4.2** recorded in $CDCl_3$. The solvent residual peak is at 7.26 ppm (singlet).

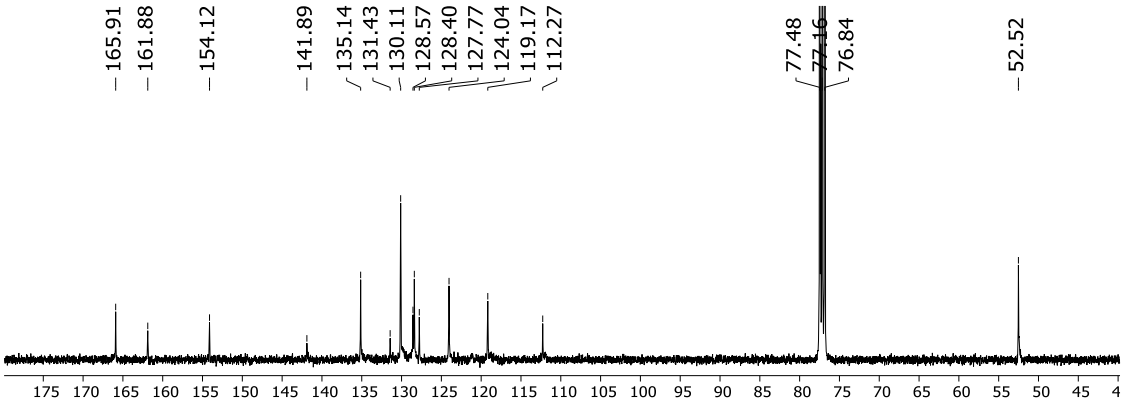

Figure A.10 The ^{13}C NMR spectrum of **4.2** recorded in $CDCl_3$. The solvent residual peak is at 77.2 ppm (triplet).

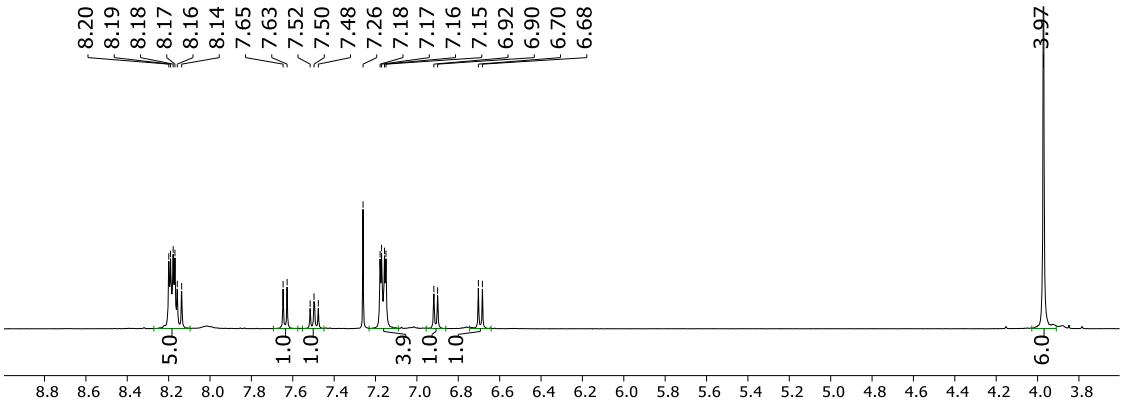

Figure A.11 The ^{1}H NMR spectrum of **4.3** recorded in $CDCl_3$. The solvent residual peak is at 7.26 ppm (singlet).

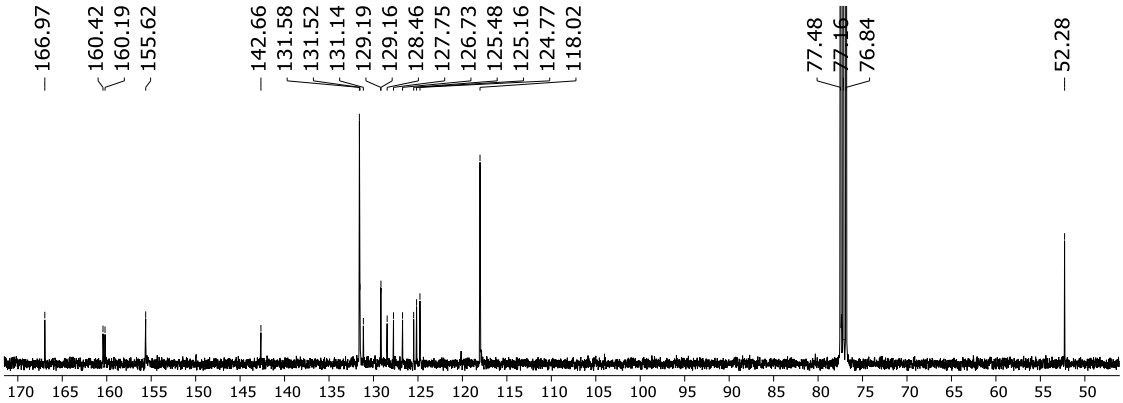

Figure A.12 The ^{13}C NMR spectrum of **4.3** recorded in $CDCl_3$. The solvent residual peak is at 77.2 ppm (triplet).

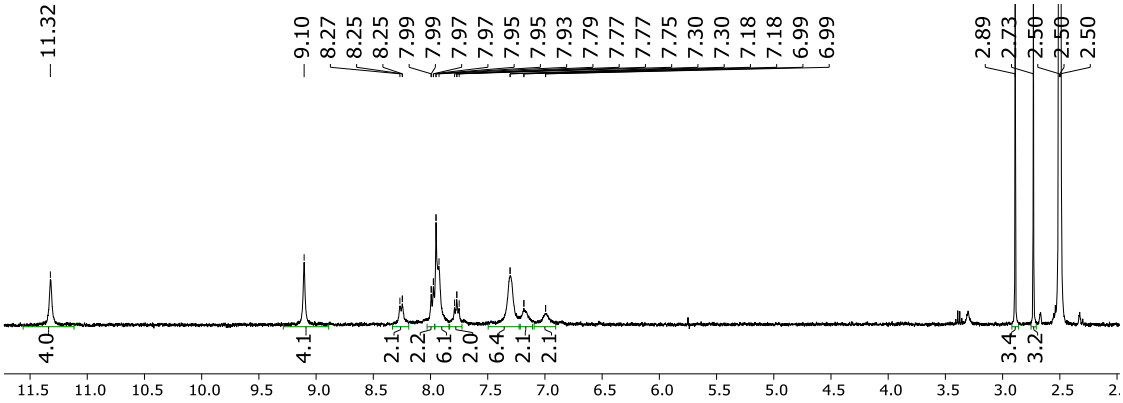

Figure A.13 The ^{1}H NMR spectrum of **4.4** recorded in DMSO-d_6. The solvent residual peak is at 2.50 ppm (quintet), while the peaks at 2.73, 2.89, and 7.95 ppm are due to DMF.

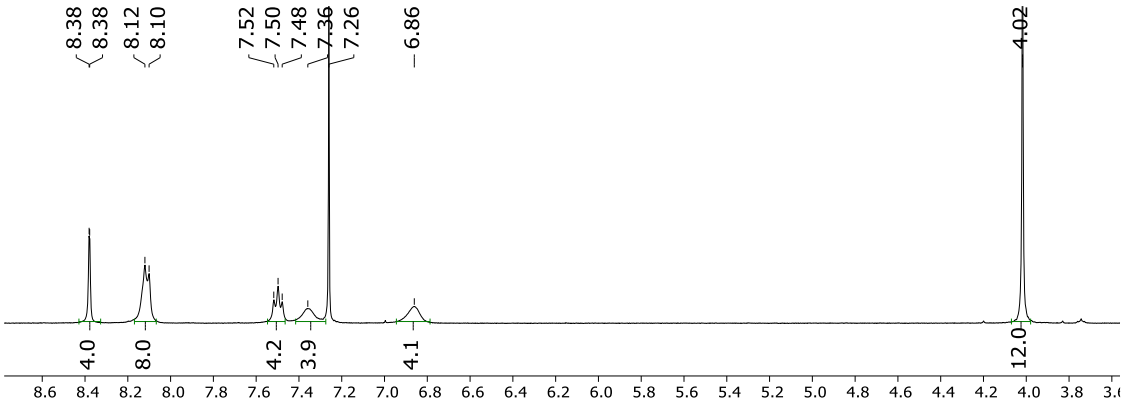

Figure A.14 The ^{1}H NMR spectrum of **4.5** recorded in $CDCl_3$. The solvent residual peak is at 7.26 ppm (singlet).

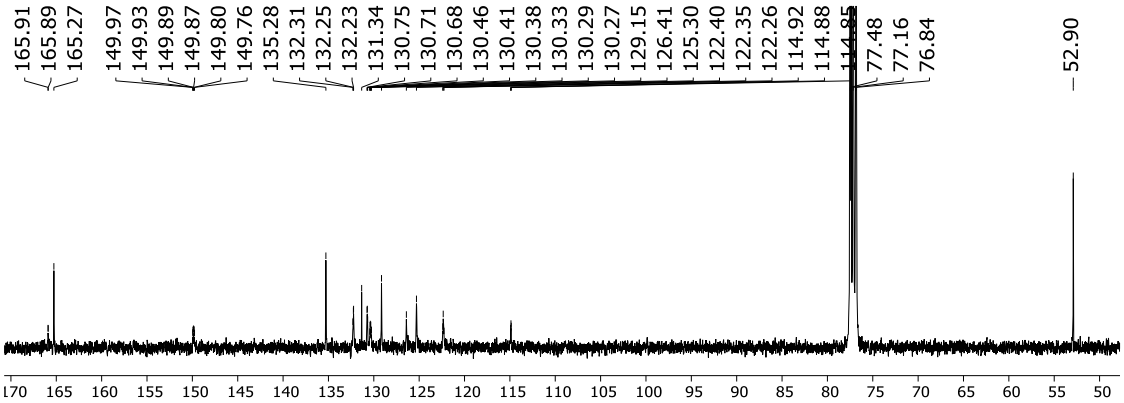

Figure A.15 The ^{13}C NMR spectrum of **4.5** recorded in $CDCl_3$. The solvent residual peak is at 77.2 ppm (triplet).

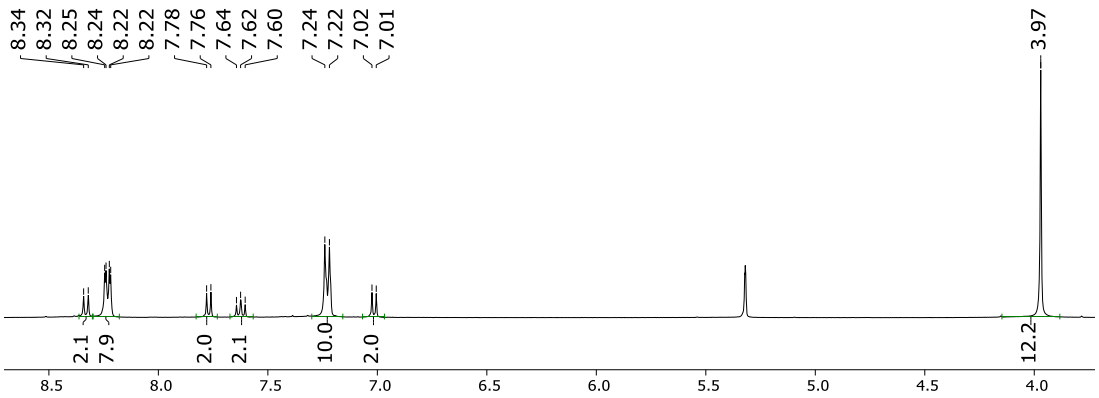

Figure A.16 The ^{1}H NMR spectrum of **4.6** recorded in $CDCl_3$. The solvent residual peak is at 7.26 ppm (singlet).

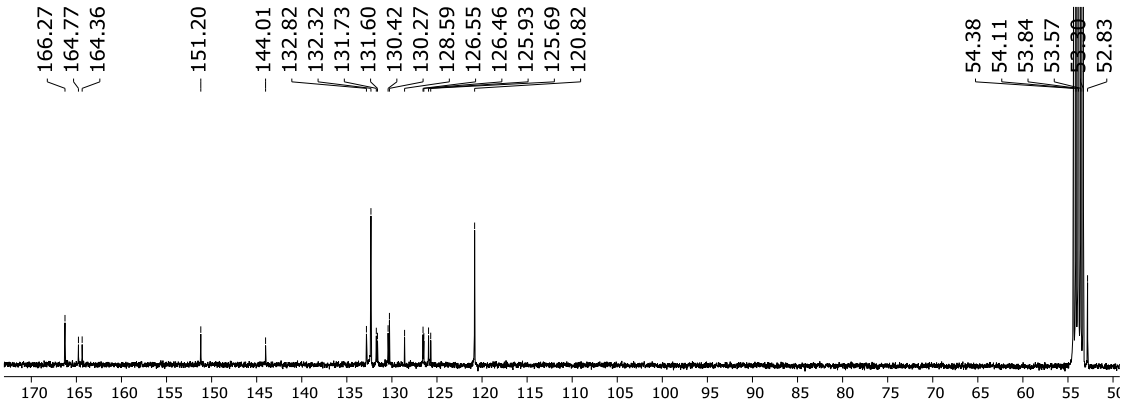

Figure A.17 The ^{13}C NMR spectrum of **4.6** recorded in $CDCl_3$. The solvent residual peak is at 77.2 ppm (triplet).

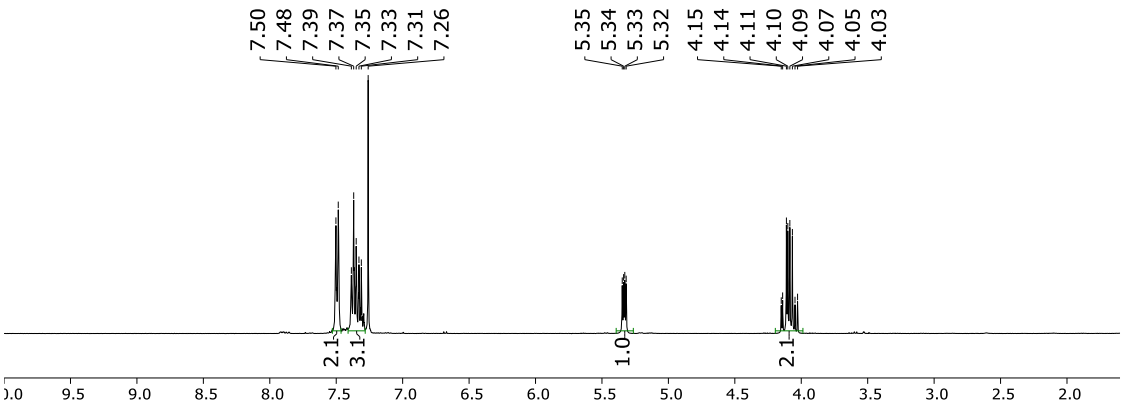

Figure A.18 The ^{1}H NMR spectrum of (1,3,3,3-tetrabromopropyl)benzene recorded in $CDCl_3$. The solvent residual peak is at 7.26 ppm (singlet).

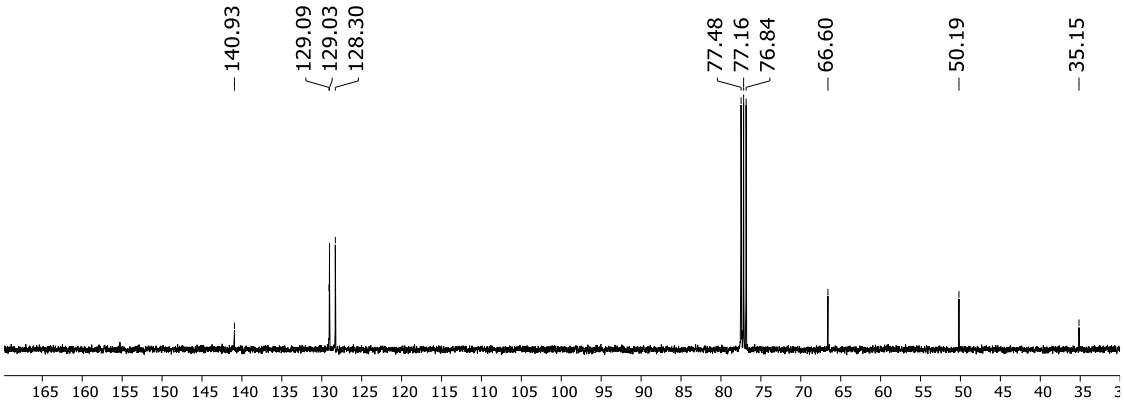

Figure A.19 The ^{13}C NMR spectrum of (1,3,3,3-tetrabromopropyl)benzene recorded in $CDCl_3$. The solvent residual peak is at 77.16 ppm (triplet).

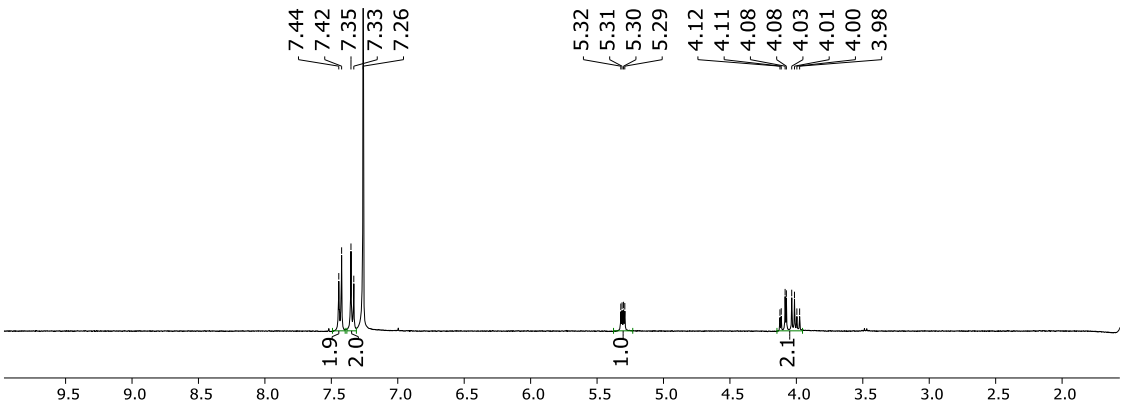

Figure A.20 The ^{1}H NMR spectrum of 1-chloro-4-(1,3,3,3-tetrabromopropyl)benzene recorded in $CDCl_3$. The solvent residual peak is at 7.26 ppm (singlet).

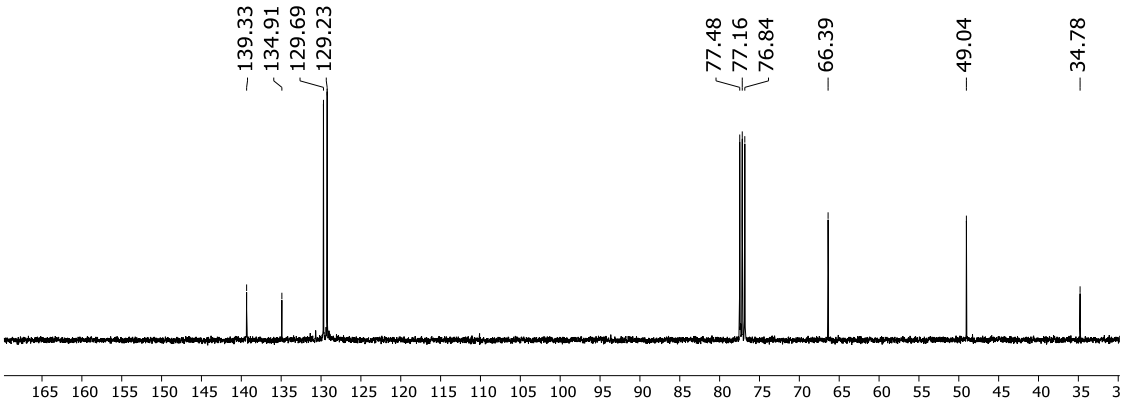

Figure A.21 The ^{13}C NMR spectrum of 1-chloro-4-(1,3,3,3-tetrabromopropyl)benzene recorded in $CDCl_3$. The solvent residual peak is at 77.16 ppm (triplet).

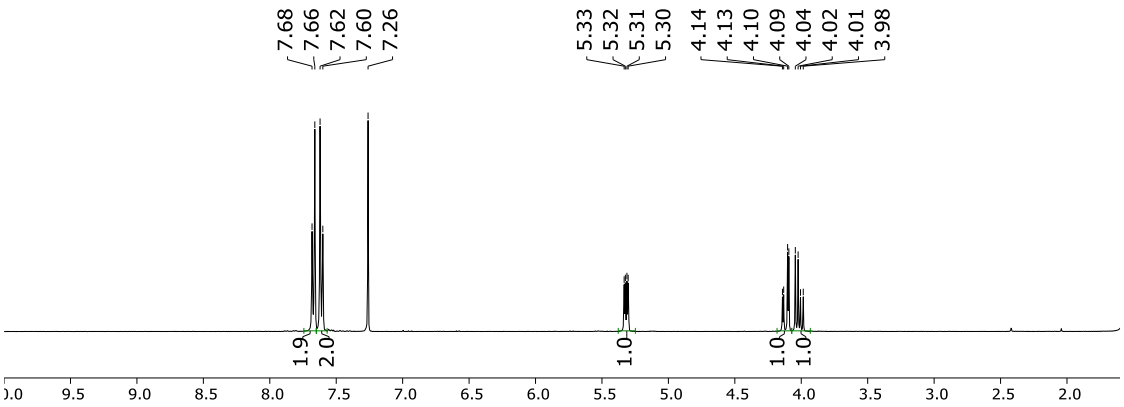

Figure A.22 The ^{1}H NMR spectrum of 1-cyano-4-(1,3,3,3-tetrabromopropyl)benzene recorded in $CDCl_3$. The solvent residual peak is at 7.26 ppm (singlet).

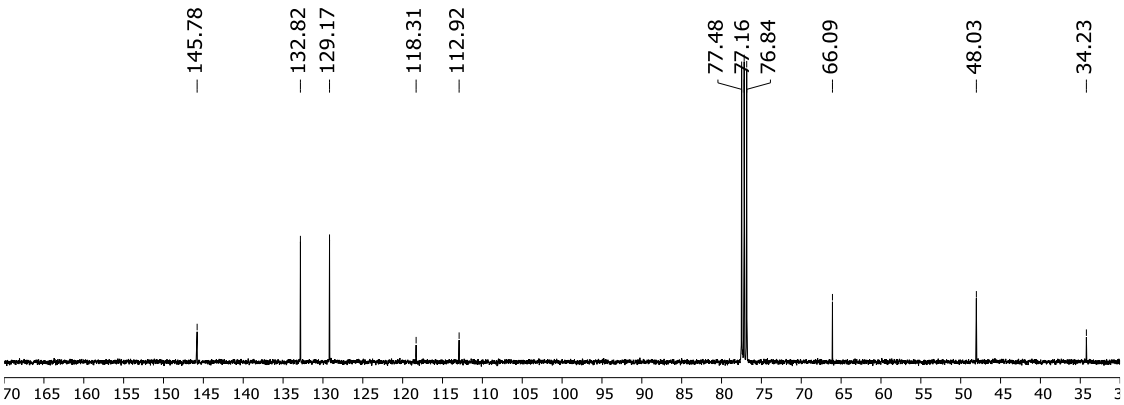

Figure A.23 The ^{13}C NMR spectrum of 1-cyano-4-(1,3,3,3-tetrabromopropyl)benzene recorded in $CDCl_3$. The solvent residual peak is at 77.16 ppm (triplet).

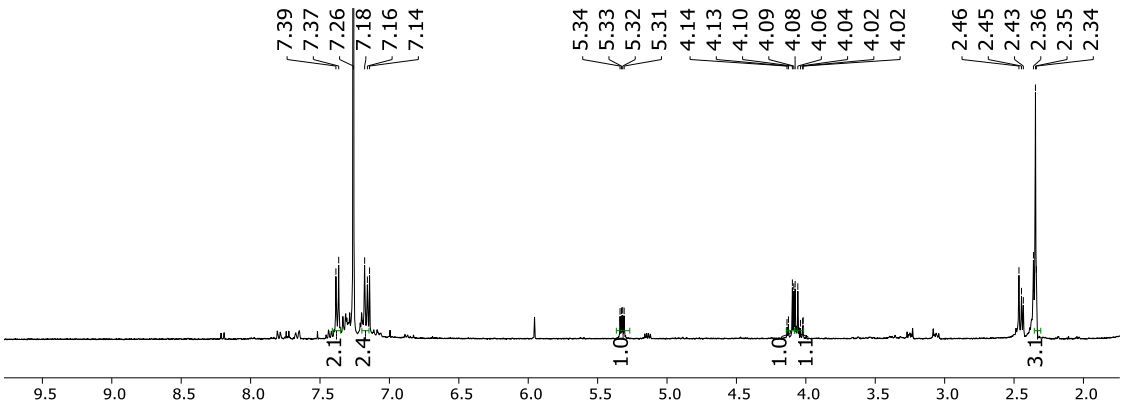

Figure A.24 The ^{1}H NMR spectrum of 1-methyl-4-(1,3,3,3-tetrabromopropyl)benzene recorded in $CDCl_3$. The solvent residual peak is at 7.26 ppm (singlet).

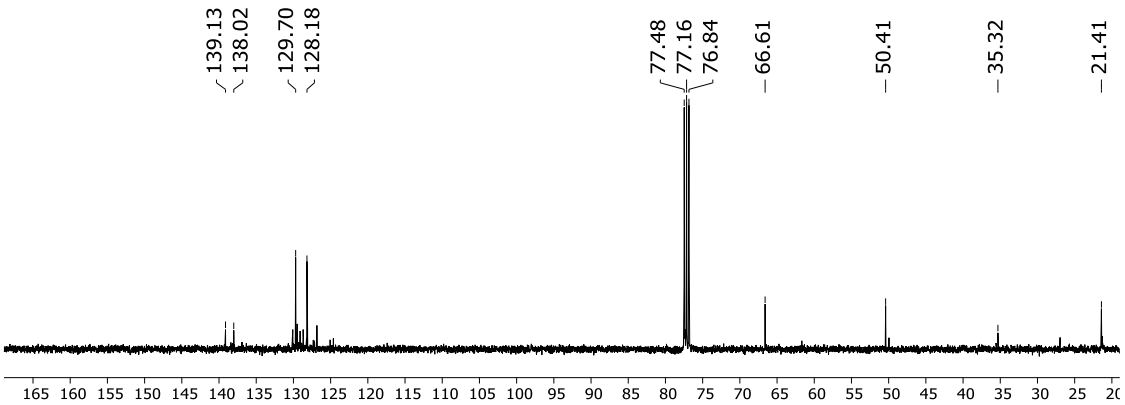

Figure A.25 The ^{13}C NMR spectrum of 1-methyl-4-(1,3,3,3-tetrabromopropyl)benzene recorded in $CDCl_3$. The solvent residual peak is at 77.16 ppm (triplet).

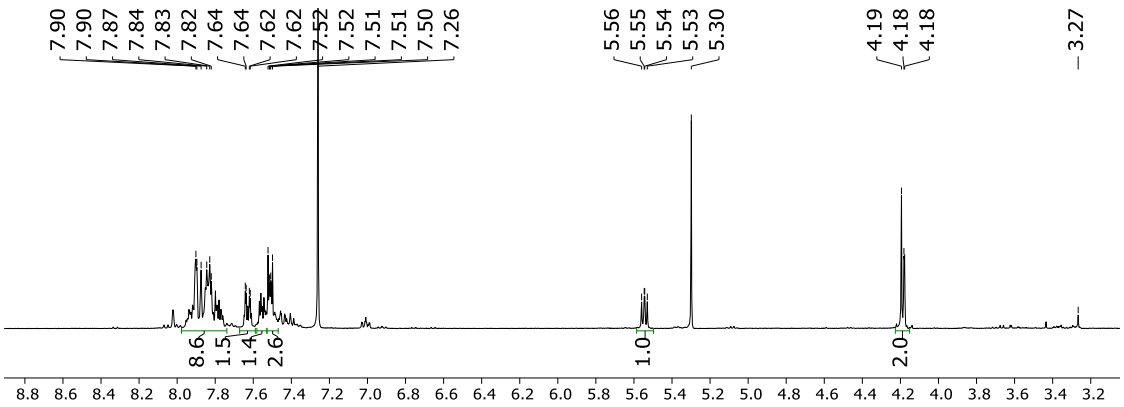

Figure A.26 The ^{1}H NMR spectrum of the crude reaction mixture with 2-(1-bromo-3,3,3-tribromopropyl)-naphthalene recorded in $CDCl_3$. The solvent residual peak is at 7.26 ppm (singlet).

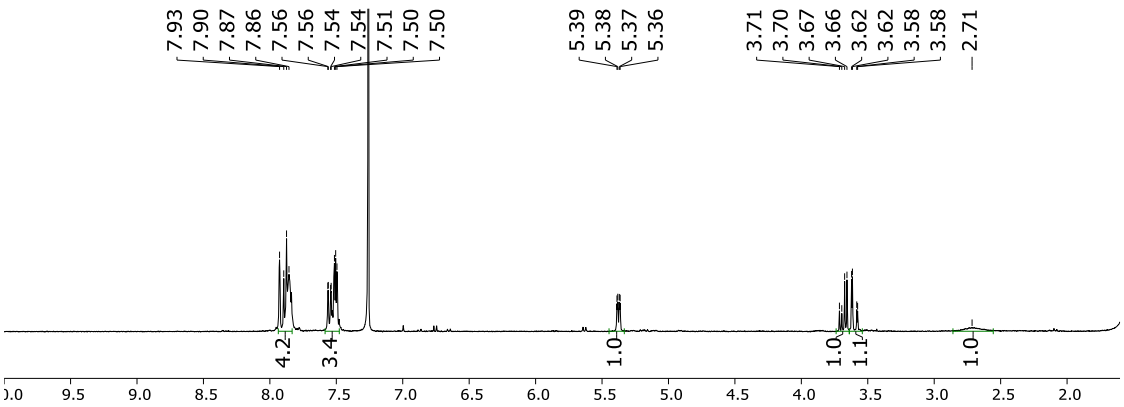

Figure A.27 The ^{1}H NMR spectrum of 3,3,3-tribromo-1-(naphthalen-2-yl)propan-1-ol recorded in $CDCl_3$. The solvent residual peak is at 7.26 ppm (singlet).

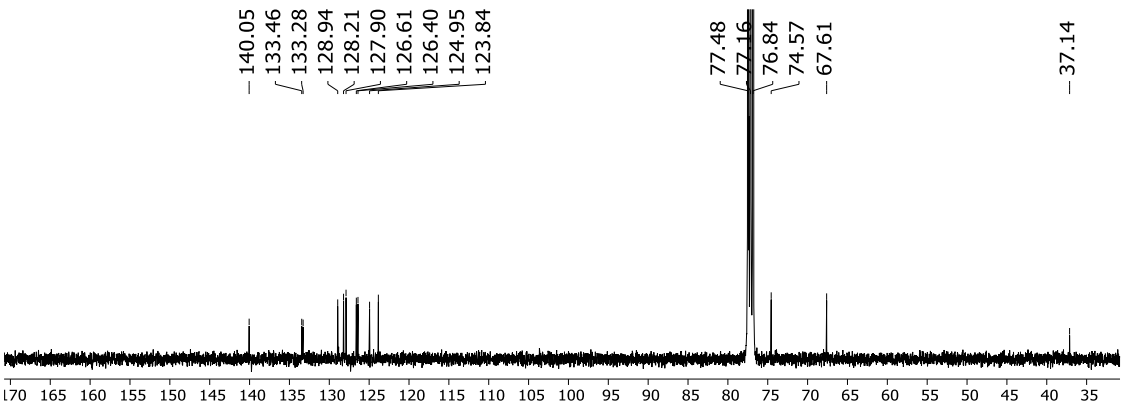

Figure A.28 The ^{13}C NMR spectrum of 3,3,3-tribromo-1-(naphthalen-2-yl)propan-1-ol recorded in $CDCl_3$. The solvent residual peak is at 77.16 ppm (triplet).

X-Ray Data of Compounds

Table A.1 Crystal data and structure refinement for **2.2**

	2.2
Chemical formula	$C_{28}H_{18}I_2N_2O_4$
Formula weight	700.24 g/mol
Temperature	103(2) K
Wavelength	0.71073 Å
Crystal size	0.100 x 0.180 x 0.280 mm
Crystal habit	orange block
Crystal system	triclinic
Space group	P -1
Unit cell dimensions	a = 9.8551(5) Å; α = 87.110(2)° b = 10.0192(6) Å; β = 78.367(2)° c = 14.2431(7) Å; γ = 65.0268(19)°
Volume	1247.74(12) $Å^3$
Z	2
Density (calculated)	1.864 g/cm^3
Absorption coefficient	2.559 mm^{-1}
F(000)	676
θ range	2.46 to 31.15°
Index ranges	-14<=h<=14, -14<=k<=14, -20<=l<=20
Refl. collected	24090
Indep. Reflns. (R_{int})	8056 [R(int) = 0.0460]
Coverage of independent reflections	99.7%
Max. and min. transmission	0.7840 and 0.5340
Data / restraints / parameters	8056 / 0 / 327
Goodness-of-fit on F^2	1.011
Δ/σ_{max}	0.001
Final R indices [I>2σ(I)]	R1 = 0.0333, wR2 = 0.0664
R indices (all data)	R1 = 0.0502, wR2 = 0.0744
Largest diff. peak and hole	1.020 and -0.742 $eÅ^{-3}$
R.M.S. deviation from mean	0.136 $eÅ^{-3}$
Refinement method	Full-matrix least-squares on F^2

X-ray crystallographic data for **2.2** has been deposited at the Cambridge Crystallographic Data Centre (CCDC) under deposition number CCDC1431314.

Table A.2 Crystal data and structure refinement for **2.4** grown from DCM/Et_2O and toluene/THF

	2.4 (DCM/Et_2O)	**2.4** (toluene/THF)
Chemical formula	$C_{58}H_{40}Cl_4CuF_6I_4N_4O_8P$	$C_{82}H_{75}CuF_6I_4N_4O_{11}P$
Formula weight	1778.85 g/mol	2008.57 g/mol
Temperature	103(2) K	153(2) K
Wavelength	0.71073 Å	0.71073 Å
Crystal size	0.080 x 0.120 x 0.180 mm	0.020 x 0.060 x 0.120 mm
Crystal habit	red block	blue plate
Crystal system	triclinic	triclinic
Space group	P -1	P -1
Unit cell dimensions	a = 11.844(4) Å; α = 94.692(7)° b = 13.707(5) Å; β = 97.346(7)° c = 20.634(8) Å; γ = 113.076(5)°	a = 15.3314(9) Å; α = 98.846(4)° b = 15.4957(9) Å; β = 110.128(3)° c = 18.5347(10) Å; γ = 98.427(4)°
Volume	3024.4(19) $Å^3$	3989.7(4) $Å^3$
Z	2	2
Density (calculated)	1.953 g/cm^3	1.672 g/cm^3
Absorption coefficient	2.682 mm^{-1}	1.917 mm^{-1}
F(000)	1716	1986
θ range	1.01 to 29.34°	1.20 to 26.27°
Index ranges		-18<=h<=18, -19<=k<=19, -22<=l<=22
Refl. collected	16485	84854
Indep. Reflns. (R_{int})	16485 [R(int) = 0.0898]	15930 [R(int) = 0.1456]
Coverage of indep. reflns.	99.3%	98.6%
Max. and min. transmission	0.8140 and 0.6440	0.9630 and 0.8030
Data / restraints / parameters	16485 / 82 / 808	15930 / 478 / 1035
Goodness-of-fit on F^2	1.076	1.115
Δ/σ_{max}	0.001	0.001
Final R indices [I>2σ(I)]	R1 = 0.0865, wR2 = 0.1658	R1 = 0.0840, wR2 = 0.2135
R indices (all data)	R1 = 0.1677, wR2 = 0.2071	R1 = 0.1914, wR2 = 0.2916
Largest diff. peak and hole	2.540 and -1.644 $eÅ^{-3}$	2.906 and -2.189 $eÅ^{-3}$
R.M.S. deviation from mean	0.250 $eÅ^{-3}$	0.278 $eÅ^{-3}$
Refinement method: Full-matrix least-squares on F^2		

X-ray crystallographic data for **2.4** has been deposited at CCDC under deposition numbers CCDC1431315 and 1431316.

Table A.3 Crystal data and structure refinement for **4.4**

	4.4	
Chemical formula	$C_{76}H_{92}Br_2CuF_6N_{12}O_{15}P$	
Formula weight	1781.94 g/mol	
Temperature	103(2) K	
Wavelength	0.71073 Å	
Crystal size	0.160 x 0.280 x 0.400 mm	
Crystal system	monoclinic	
Space group	C 1 2/c 1	
Unit cell dimensions	a = 26.796(2) Å	α = 90°
	b = 14.7426(14) Å	β = 114.7964(15)°
	c = 22.903(3) Å	γ = 90°
Volume	8213.5(16) $Å^3$	
Z	4	
Density (calculated)	1.441 g/cm^3	
Absorption coefficient	1.342 mm^{-1}	
F(000)	3680	
θ range	1.70 to 26.42°	
Index ranges	-31<=h<=33, -18<=k<=18, -28<=l<=28	
Refl. collected	39682	
Indep. Reflns. (R_{int})	8416 [R(int) = 0.1565]	
Max. and min. transmission	0.8140 and 0.6160	
Data / restraints / parameters	8416 / 2354 / 902	
Goodness-of-fit on F^2	0.935	
Final R indices [I>2σ(I)]	R1 = 0.0866, wR2 = 0.2333	
R indices (all data)	R1 = 0.1944, wR2 = 0.2711	
Largest diff. peak and hole	0.745 and -0.744 $eÅ^{-3}$	
R.M.S. deviation from mean	0.108 $eÅ^{-3}$	
Refinement method	Full-matrix least-squares on F^2	

X-ray crystallographic data for **4.4** has been deposited at CCDC under deposition numbers CCDC1848314.

Table A.4 Crystal data and structure refinement for **4.14**

	4.14	
Chemical formula	$C_{60}H_{42}Br_2CuF_{12}N_6O_8Sb_2$	
Formula weight	1669.85 g/mol	
Temperature	100 K	
Wavelength	0.71073 Å	
Crystal size	0.140 x 0.220 x 0.280 mm	
Crystal system	monoclinic	
Space group	C 1 2/c 1	
Unit cell dimensions	a = 11.7665(11) Å	α = 90°
	b = 26.084(3) Å	β = 92.097(3)°
	c = 21.8320(18) Å	γ = 90°
Volume	6696.1(11) $Å^3$	
Z	4	
Density (calculated)	1.656 g/cm^3	
Absorption coefficient	2.397 mm^{-1}	
F(000)	3268	
θ range	2.4 to 25.0°	
Index ranges	-14<=h<=14, -30<=k<=30, -20<=l<=25	
Refl. collected	31030	
Indep. Reflns. (R_{int})	5831 [R(int) = 0.094]	
Max. and min. transmission	0.730 and 0.570	
Data / restraints / parameters	5831 / 989 / 382	
Goodness-of-fit on F^2	1.976	
Final R indices [I>2σ(I)]	R1 = 0.1755, wR2 = 0.5348	
Largest diff. peak and hole	2.64 and -1.89 $eÅ^{-3}$	
R.M.S. deviation from mean	0.262 $eÅ^{-3}$	
Refinement method	Full-matrix least-squares on F^2	

X-ray crystallographic data for **4.14** has been deposited at CCDC, under deposition numbers CCDC1866188.

Table A.5 Crystal data and structure refinement for the non-bromide version of **4.14**

Chemical formula	$C_{64}H_{56}Cl_{12}CuN_6O_9Sb_2$	
Formula weight	1785.58 g/mol	
Temperature	100(2) K	
Wavelength	0.71073 Å	
Crystal size	0.020 x 0.120 x 0.140 mm	
Crystal system	triclinic	
Space group	P -1	
Unit cell dimensions	a = 14.5160(7) Å	α = 70.8459(13)°
	b = 15.1547(7) Å	β = 79.6608(14)°
	c = 18.4079(9) Å	γ = 69.3416(13)°
Volume	3570.0(3) $Å^3$	
Z	2	
Density (calculated)	1.661 g/cm^3	
Absorption coefficient	1.554 mm^{-1}	
F(000)	1778	
θ range	2.15 to 32.72°	
Index ranges	-22<=h<=21, -23<=k<=22, -27<=l<=26	
Refl. collected	71794	
Indep. Reflns. (R_{int})	26023 [R(int) = 0.0776]	
Max. and min. transmission	0.9700 and 0.8120	
Data / restraints / parameters	26023 / 568 / 984	
Goodness-of-fit on F^2	1.026	
Final R indices [I>2σ(I)]	R1 = 0.0660, wR2 = 0.1356	
R indices (all data)	R1 = 0.1407, wR2 = 0.1689	
Largest diff. peak and hole	2.157 and -1.447 $eÅ^{-3}$	
R.M.S. deviation from mean	0.137 $eÅ^{-3}$	
Refinement method	Full-matrix least-squares on F^2	